2

NATIONAL AERONAUTICS AND SPACE ADMINISTRATION

Technical Memorandum 33-644

Effects of Turbulence in the Atmosphere of Venus on Pioneer Venus Radio—Phase I

R. Woo
W. Kendall
A. Ishimaru
R. Berwin

JET PROPULSION LABORATORY
CALIFORNIA INSTITUTE OF TECHNOLOGY
PASADENA, CALIFORNIA

June 30, 1973

NATIONAL AERONAUTICS AND SPACE ADMINISTRATION

Technical Memorandum 33-644

Effects of Turbulence in the Atmosphere of Venus on Pioneer Venus Radio—Phase I

R. Woo
W. Kendall
A. Ishimaru
R. Berwin

JET PROPULSION LABORATORY
CALIFORNIA INSTITUTE OF TECHNOLOGY
PASADENA, CALIFORNIA

June 30, 1973

Prepared Under Contract No. NAS 7-100
National Aeronautics and Space Administration

PREFACE

This report presents the results of one phase of research carried out at the Jet Propulsion Laboratory, California Institute of Technology, for the NASA Ames Research Center by agreement with the National Aeronautics and Space Administration (Contract NAS 7-100). W. Kendall and A. Ishimaru are consultants to the Jet Propulsion Laboratory.

ACKNOWLEDGMENT

We wish to thank D. Nixon for his cooperation and assistance in retrieving and processing the Mariner 5 tapes, W. Hullinger for providing invaluable assistance in interfacing the computer programs with the various operating systems of the IBM/360 computers, G. Anenberg for computation of the results presented in Figs. 3 and 4, G. Fjeldbo for discussion on ray penetration distance versus time for Mariner 5, and A. Ludwig and G. Levy for support throughout the course of this work.

CONTENTS

FIGURES (contd)

FIGURES (contd)

FIGURES (contd)

FIGURES (contd)

Abstract

The purpose of this study is to predict the effects of turbulence in the atmosphere of Venus on Pioneer Venus radio. Estimates of turbulence effects depend a great deal on our knowledge of the turbulence. Although very little is known about the turbulence in the Venusian atmosphere, valuable information can be inferred from radio measurements of the planet's atmosphere made by the previous space probes Venera and Mariner 5.

A careful investigation based on a theoretical and experimental study of the power spectrum of the Mariner 5 amplitude fluctuations is carried out and the results contribute considerably to our scientific knowledge of turbulence in the atmosphere of Venus. Fully developed turbulence is seen to exist predominantly in the altitude range of 41 - 49 km. This result is consistent with the high wind shear and wind velocities observed by Venera 4 for altitudes higher than 40 km. The outer scale size of turbulence is on the order of 100 m, the structure constant for the dayside atmosphere 3.9×10^{-7} $m^{-1/3}$, and that for the nightside atmosphere 2.9×10^{-7} $m^{-1/3}$.

Estimates for Pioneer Venus indicate that the variance of log-amplitude fluctuations is less than 0.056, the variance of phase fluctuations less than 0.88 rad^2 and the bandwidth of both amplitude and phase fluctuations no more than a few Hz.

I. Introduction

Since the atmosphere of Venus is very dense, even slight perturbations in the atmosphere caused by winds, thermal currents, etc., could give rise to substantial fluctuations in the refractive index. As a result, a radio wave propagating through the Venusian atmosphere would be expected to suffer fluctuations and undergo spectral broadening. These turbulence effects play a key role in the design of the communications link with the Pioneer Venus entry probes and the purpose of this study is to estimate them.

The quantities that we are interested in predicting for the Pioneer Venus link consist of the probability density functions, the means, the variances, and the power spectra of the amplitude and phase fluctuations. The communications engineer can in turn use these results to estimate the tracking ability and degradation of the phase coherent system. To make predictions for the turbulence effects we must know the nature and the characteristics of the atmospheric turbulence. No direct measurements for the Venusian atmosphere have been made. However, some pertinent information can be inferred from the radio link of spacecraft that probed the atmosphere of Venus. These of course include Mariner 5 and the Venera spacecraft. Our predictions for Pioneer Venus, therefore, rely heavily on radio measurements made by previous space probes.

This report is organized in the following manner. In Section II we present a very brief summary of the theory of wave propagation through turbulent medium. To include a complete presentation is impossible within the scope of this report. Nevertheless, our objective is to point out the salient features and to provide the reader with a source of tutorial references. In Section III the basic equations are presented and predictions of the effects of Venusian atmospheric

turbulence on the Pioneer Venus radio link are given. These estimates are based on the Venera radio data. In Section IV we present the results of processing the Mariner 5 occultation data. The turbulence effects that appear to be present are then compared with the developed theory as well as the Venera results. An additional crude estimate of radio spectral broadening can be obtained by analyzing the received spectra from the Venus radar experiment. This is discussed in Section V. Finally, conclusions and future work are summarized in Section VI.

II. Wave Propagation Through Turbulent Medium

In recent years there has been an increased interest in the problem of fluctuations in an electromagnetic wave as a result of scattering from random variations in the refractive index. In the earth's atmosphere these effects are often negligible at S-band, but become dominant in the millimeter and optical bands. Consequently, much of the recent work has dealt with the higher frequencies. In the case of Venus, because the lower atmosphere is so much denser than that of earth, turbulence is expected to affect frequencies as low as S-band. The available theory for wave propagation through turbulent medium is applicable to both the microwave and optical bands.

Extensive investigations of turbulence effects on wave propagation have been carried out by Tatarski (Refs. 1-2). Although very mathematical, the study of wave propagation in a turbulent medium consists of two basic steps. The first is the solution of Maxwell's equations to obtain the fluctuations in the electromagnetic wave in terms of the refractive index fluctuations. The method most widely used is Rytov's method which takes into account diffraction and multiple scattering effects. Rytov's method is valid when the fluctuations of the electromagnetic wave are small as in the case of microwave propagation through the atmosphere of Venus. The second step in the study of wave propagation in turbulent medium involves the characterization of the refractive index fluctuations. The power spectrum of the refractive index fluctuations is most convenient because its form in the atmosphere is the same as that of the wind velocity fluctuation spectrum. The wind velocity spectrum has received much attention from the atmospheric physicist and there is both theoretical and experimental evidence to indicate that its form follows that of the well-known Kolmogorov spectrum for fully-developed turbulence (Refs. 1-5, 8, 9).

Several excellent review articles of atmospheric turbulence and its effect on wave propagation have been published. Two general articles by Wheelon in 1959 (Refs. 6, 7) give a review of the state-of-art at that time. More recently, Strohbehn (Ref. 8) reviewed Rytov's method and its range of validity, Kolmogorov's spectrum and the probability density functions of the amplitude and phase fluctuations, while Lawrence and Strohbehn (Ref. 9) summarized the variances and temporal power spectra for the amplitude and phase fluctuations. Although the emphasis of the last two references is on optical frequencies, the results are equally applicable to microwave frequencies and the validity of this application is discussed in Ref. 10. The state-of-art of wave propagation in turbulent medium has also been reviewed in a recent Russian paper (Ref. 11) which is particularly useful because it contains a very extensive list of references. Several survey papers cover the effects of atmospheric turbulence on communications. Brookner (Refs. 12, 13) reviews the turbulence effects in terms of a communication channel model, while Kerr, et. al. (Ref. 14) discuss the consideration of atmospheric turbulence in the design of a communication system.

III. Estimates for Pioneer Venus Based on Venera Radio Data

Let us consider a turbulent medium characterized by the refractive index

$$n(\vec{r}) = 1 + n_1(\vec{r}) \tag{1}$$

where $n_1(\vec{r})$ is the fluctuation and assumed small and $\vec{r}$ is position. We write the propagating electric field in the absence of turbulence

$$u_o(\vec{r}) = A_o(\vec{r})\ e^{i\phi_o(\vec{r})} \tag{2}$$

where A_o is the amplitude and ϕ_o the phase. When the turbulence effects are included the electric field becomes

$$u(\vec{r}) = A(\vec{r})\ e^{i\phi(\vec{r})} \tag{3}$$

The turbulence effects are generally described in terms of the quantities log-amplitude fluctuation $\chi = \ell n \frac{A}{A_o}$ and phase fluctuation $S = \phi - \phi_o$. We note that (3) can be alternately written as

$$u(\vec{r}) = u_o(\vec{r})\ e^{\psi(\vec{r})} \tag{4}$$

where $\psi = \chi + iS$. For weak fluctuations, Maxwell's equations can be solved using Rytov's method to yield the first iterated solution (Refs. 1, 2, 8)

$$\psi(\vec{r}) = \int_{V'} 2k^2 G(\vec{r} - \vec{r}') \frac{u_o(\vec{r}')}{u_o(\vec{r})}\ n_1(\vec{r}')\ dV' \tag{5}$$

where G is the free space Green's function, k is the free space wave number and dV' is the differential scattering volume element. In the case of Pioneer Venus, we will assume that the radio frequency is 2297 MHz so that k = 48.11 rad/m. It is clear that (5) describes the fluctuations in the electromagnetic wave in terms of the refractive index fluctuations. According to (5) and assuming that the correlation distance of $n_1(\vec{r})$ is small compared to the dimensions of V', χ and S are both composed

of the sum of a large number of independent components, and therefore have a Gaussian distribution by virtue of the Central Limit Theorem. This means that A has a log-normal distribution. There have been alternative arguments in favor of the Rayleigh or Rice-Nakagami distribution for the amplitude A. For weak fluctuations there is little difference between the Rayleigh and log-normal distributions. Moreover, experimental evidence seems to support the log-normal distribution. A good summary of the distribution of A can be found in Refs. 8, 9 and 11.

The variance of the log-amplitude fluctuations σ_χ^2 is a measure of the strength of signal amplitude fluctuations. For weak fluctuations ($\sigma_\chi^2 << 1$):

$$\sigma_\chi^2 = \langle(\chi - \langle\chi\rangle)^2\rangle \simeq \left\langle\left(\frac{A - A_o}{A_o}\right)^2\right\rangle \tag{6}$$

where the brackets $\langle\ \rangle$ denote an average or expectation and $\langle\chi\rangle \simeq 0$. If the conservation of power is invoked, we can use the identity (Ref. 15)

$$\langle e^{ag}\rangle = e^{a\langle g\rangle + \frac{1}{2}a^2\langle(g - \langle g\rangle)^2\rangle} \quad \text{(g is Gaussian)} \tag{7}$$

to show that (4) yields

$$\begin{aligned} \langle A\rangle &= A_o\, e^{-\left(\frac{\sigma_\chi^2}{2}\right)} \\ \text{or}\quad \langle\chi\rangle &= -\frac{\sigma_\chi^2}{2} \end{aligned} \tag{8}$$

As mentioned in Section II, the refractive index fluctuations are characterized by the power spectrum which we denote $\Phi_n(K)$, where K is the spatial wave number. For well-developed turbulence, $\Phi_n(K)$ follows the well-known Kolmogorov spectrum, which can be written (Refs. 1, 2, 8, 9)

$$\Phi_n(K) = 0.033\, c_n^2(\vec{r})\, K^{-11/3} \tag{9}$$

where the structure constant c_n characterizes the intensity of turbulence and may vary as a function of position. The turbulence present in the atmosphere of Venus appears to be well-developed (Refs. 16, 17) and we will use Kolmogorov's spectrum of the form proposed by von Kármán (Refs. 1, 2, 8) to describe it, i.e.,

$$\Phi_n(K) = 0.033\, c_n^2(\vec{r}) \left(K^2 + \frac{1}{L_o^2}\right)^{-11/6} \tag{10}$$

where L_o is the outer scale of turbulence. The reason for using (10) instead of (9) is that (10) includes the effects of blob sizes larger than L_o. Additional comments on this point will be made later.

The spatial correlation functions for χ and S can be formed in terms of the spectrum (10) using (5), and the respective variances obtained. In a previous study (Ref. 18) it was shown that when the path length in the turbulent atmosphere was shorter than kL_o^2, as in the case of Pioneer Venus, then the effect of outer scale size on σ_χ^2 is negligible. For the Pioneer Venus configuration shown in Fig. 1, we therefore have (Refs. 1, 2, 17)

$$\sigma_\chi^2\ (z = z_o) = 0.565 \int_{z_o}^{\infty} c_n(z)\, z^{5/6}\, dz \tag{11}$$

where $\sigma_\chi^2\ (z = z_o)$ is the variance of the log-amplitude fluctuations of the radio signal received from the entry probe when it is located at altitude z_o. As can be seen, the spatial variation of c_n plays an important role in the determination of the effects of turbulence. Meaningful prediction of signal fading for Pioneer Venus due to atmospheric turbulence cannot be made without

some reliable estimates of the structure constant and its variation with altitude. Although no direct measurements of the structure constant have ever been performed, estimates can be inferred from the radio data transmitted through the Venusian atmosphere by space probes. In this section we will discuss the Venera data only. The Mariner 5 results will be covered in Section IV.

Veneras 4 through 8 were slow-descent probes with Veneras 4, 5 and 6 reaching approximate altitudes of 26, 24 and 19 kms respectively, and Veneras 7 and 8 successfully landing on the surface of Venus. The signals received from the Venera spacecraft were processed and their standard deviations computed over various time segments as the spacecraft descended through the atmosphere (Refs. 19-21). The standard deviations due to instrument error and interplanetary plasma scintillation were estimated and subtracted from the processed results, and the remaining part σ_χ was attributed to atmospheric turbulence. Fig. 2 is reproduced from Ref. 21 and summarizes the results obtained for Veneras 5 - 7. To estimate the structure constant, Yakovlev, et. al. (Ref. 21) assumed that c_n was constant in the altitude range 0 - 55 km. In other words, they assumed that the turbulence was homogeneous for altitudes lower than 55 km and non-existent for higher altitudes. Thus, (11) can be easily integrated to yield

$$\sigma_\chi^2 = 0.308\, c_n^2\, k^{7/6}\, L^{11/6} \tag{12}$$

where L is the penetration distance of the probe into the Venusian atmosphere. The dashed line in Fig. 2 represents (12) where a value of 1.4×10^{-7} $cm^{-1/3}$ for c_n was used. Although it is obvious that there is a large scatter of data, it should be pointed out that much of this could be due to the variation of c_n

with the various missions. A more meaningful check would be established if just the Venera 7 results were used. Unfortunately, Yakovlev, et. al., did not label their data. Although there does appear to be less scatter when (12) is compared with the separate sets of data obtained from Veneras 4 through 6 (Refs. 19, 20), the estimates derived from the Venera radio data are at best order-of-magnitude estimates only.

Prior to Venera 7, de Wolf (Refs. 22, 23) extrapolated the Venera 4 results to the surface of Venus and pointed out that serious fading could be expected there. This extrapolation assumed that the structure constant increased exponentially with decrease in altitude and was reasonable since this type of variation has been observed in the earth's lower atmosphere (Ref. 24). On the other hand, the homogeneous model used by Yakovlev, et. al., is also plausible in view of the fact that although the lower atmosphere is dense, it is relatively calm as evidenced by the atmospheric wind velocity profiles (Ref. 16). At any rate, the difference between extrapolating the structure constant inferred from Venera 4 exponentially or as a constant, is significant. In the case of exponential extrapolation, severe fading could occur. In the absence of radio data from the surface of Venus, other than that of Venera 7, we will assume that the turbulence is homogeneous. It must be emphasized that our predictions are only as valid as the estimates of turbulence inferred by Yakovlev, et. al., from the Venera 7 radio data.

According to Yakovlev, et. al. (Ref. 21), when Venera 7 was on the surface of Venus σ_χ was 0.073. For Venera 7, $\lambda = 0.3$ m and letting L = 55 km, (12) yields

$$c_n = 1.012 \times 10^{-6}\ m^{-1/3} \tag{13}$$

It might be interesting to note that (13) is about an order of magnitude higher than the value for c_n deep in the earth's atmosphere (Refs. 24, 25, 28). Using the value of c_n in (13), we obtain from (12) the following estimates for Pioneer Venus on the surface of Venus:

$$\begin{aligned} \sigma_\chi &= 0.1189 \\ \sigma_\chi^2 &= 0.014 \end{aligned} \tag{14}$$

and the corresponding <A> can be computed using (8).

In the case of phase, $\sigma_S^2 = \sigma_\phi^2$. If we assume (10), we can derive the following results for σ_ϕ^2 in homogeneous turbulence using the general results given in Ref. 18:

$$\sigma_\phi^2 = 0.782\, k^2\, L_o^{5/3}\, c_n^2\, L - \sigma_\chi^2 \tag{15}$$

where σ_χ^2 is (12). As is expected, the phase fluctuations, unlike the amplitude fluctuations, receive contributions from blob sizes larger than L_o (Refs. 8, 18). Although L_o is unknown, some estimate can be derived from the Mariner 5 data as will be shown in Section IV. L_o appears to be approximately 100 m. If L_o is 100 m, we let L = 55 km and from (12) and (15) we obtain for the probe on the surface of Venus

$$\begin{aligned} \sigma_\phi &= 0.4535 \text{ rad} \\ \sigma_\phi^2 &= 0.2057 \text{ rad}^2 \end{aligned} \tag{16}$$

It should be pointed out that according to Ref. 20, Venera 4 observed stronger turbulence than Veneras 5 - 7. In fact, the value of c_n is approximately twice that inferred from Veneras 5 - 7. If we use this worst case estimate, we have

$$\begin{aligned} \sigma_\chi &= 0.2378 \\ \sigma_\chi^2 &= 0.056 \\ \sigma_\phi &= 0.9373 \text{ rad} \\ \sigma_\phi^2 &= 0.8786 \text{ rad}^2 \end{aligned} \tag{17}$$

Until now we have discussed only the variances of the log-amplitude and phase fluctuations. It is important in the design of a coherent communications link to know how these fluctuations are distributed in frequency. We shall therefore consider the temporal frequency spectra of the log-amplitude fluctuations $W_\chi(f)$ and the phase fluctuations $W_S(f)$. If the time correlation functions of χ and S are $B_\chi(t)$ and $B_S(t)$, respectively, their Fourier Transforms are the corresponding frequency spectra. Thus

$$\begin{aligned} W_\chi(f) &= 4\int_{-\infty}^{\infty} B_\chi(t)\, e^{-i2\pi ft}\, dt \\ W_S(f) &= 4\int_{-\infty}^{\infty} B_S(t)\, e^{-i2\pi ft}\, dt \end{aligned} \tag{18}$$

To determine the variations in time and consequently the frequency spectra of the log-amplitude and phase fluctuations, Taylor's frozen-in hypothesis is generally assumed (Refs. 1, 2, 9). Under this assumption, the atmospheric inhomogeneities are frozen-in and the time variations of the received signal are due to movement of the inhomogeneities across the propagation path by the wind. Essentially, only the component of wind velocity perpendicular to the propagation path need be considered and we denote it $v_\perp$. The frozen-in model is valid as long as the lives of the individual eddies of the turbulent atmosphere are longer than the time it takes for an eddy to cross the propagation path. Tatarski (Ref. 2) has shown that this condition is met when

$L \ll L_o^2/\lambda$. For L_o = 100 m, L_o^2/λ = 77 km. The frozen-in hypothesis is, therefore, valid even when the Pioneer Venus probe is on the surface of Venus. Another point worth mentioning is the fact that Tatarski (Refs. 2, 9) has also analyzed the case where the motion of the eddies is completely random. His results indicate that the spectra for completely random motion and those for constant motion (frozen turbulence) are similar.

We assume that the Pioneer Venus probe in Fig. 1 is transmitting a spherical wave. Then, using Rytov's method and the frozen-in hypothesis, the received spectra at a distance L' away are (Ref. 25):

$$\left.\begin{matrix} W_\chi(f) \\ W_S(f) \end{matrix}\right\} = 8\pi^2 k^2 \int_{\frac{2\pi f}{v_\perp}}^{\infty} K\, dK \int_0^{L'} d\eta \left\{\begin{matrix} h_\chi(\eta,K) \\ h_S(\eta,K) \end{matrix}\right\} \Phi_n(K) \frac{1}{\sqrt{k^2 v_\perp^2 - (2\pi f)^2}} \tag{19}$$

where

$$h_\chi(\eta,K) = 1 - \left[\cos \frac{\eta}{L}(L-\eta)\frac{K^2}{\eta}\right] \tag{20}$$

$$h_S(\eta,K) = 1 + \left[\cos \frac{\eta}{L}(L-\eta)\right] \tag{21}$$

Letting L' = L + L" (see Fig. 1) and noting that L" >> L, L' in (19) becomes L, and (20) and (21) reduce to

$$h_\chi(\eta,K) = 1 - \cos \frac{\eta K^2}{k} \tag{22}$$

$$h_S(\eta,K) = 1 + \cos \frac{\eta K^2}{k} \tag{23}$$

It should be noted that (22) and (23) along with resultant (19) are the same as the frequency spectra for a plane wave received at a distance L away. Again we will use $\Phi_n(K)$ as given by (10) and will assume the turbulence to be homogeneous. In addition, we will assume that the distribution of $v_\perp$ throughout the atmosphere is constant even though the Venera probes indicate that it is far from it (Ref. 16). Still, the wind velocity distribution should not significantly affect the spectra in terms of their bandwidth, a parameter which we are primarily interested in estimating. In the future we hope to evaluate (19), (22) and (23) with the aid of a computer taking into account the wind velocity profiles observed by the Venera space probes. When $L_o = \infty$, the following asymptotic expressions can be obtained (Refs. 1, 2, 9)

$$\underset{f\to 0}{W_\chi(f)} = 0.44\,\frac{\sigma_\chi^2}{f_\perp} \qquad \text{where} \quad f_\perp = \frac{v_\perp}{2\pi}\sqrt{\frac{k}{L}} \tag{24}$$

$$\underset{f\to 0}{W_S(f)} = \underset{f\to\infty}{2W_\chi(f)} \tag{25}$$

$$\underset{f\to\infty}{W_\chi(f)} = 32.26\,W_\chi(0)\left(\frac{f}{f_\perp}\right)^{-8/3} = 1.13\,\frac{\sigma_\chi^2}{f_\perp}\left(\frac{f}{f_\perp}\right)^{-8/3} \tag{26}$$

$$\underset{f\to\infty}{W_S(f)} = \underset{f\to\infty}{W_\chi(f)} \tag{26}$$

It must be emphasized that (24) - (26) are asymptotic values only and the fact that W_S is written in terms of W_χ and vice versa does not mean that W_χ and W_S are dependent on each other.

The computer was used to calculate the intermediate values as well as the spectra corresponding to finite values of L_o. These results are summarized in Figs. 3 and 4 and are normalized with respect to $W_\chi(0)$ for $L_o = \infty$, i.e., (24). The various values of $\beta = \frac{1}{L_o}\sqrt{\frac{L}{k}}$ plotted correspond to L_o = 50, 100 and ∞ m for L = 55 km. The dependence of the spectra on L_o indicates the consequences of using von Kármán's representation of the Kolmogorov spectrum (10) instead of (9). For the amplitude fluctuations, the variation of the spectra with L_o is small. The reason of course is that the contribution of scattering from blob sizes larger than L_o to the amplitude fluctuations is very small. On the contrary, phase fluctuations do depend on scattering from blob sizes larger than L_o and the difference between von Kármán's representation (finite L_o) and the Kolmogorov spectrum (infinite L_o) is consequently most pronounced at frequencies lower than $f_\perp$. Another reason for using von Kármán's representation is demonstrated in Fig. 4 where it can be seen that the Kolmogorov spectrum ($L_o = \infty$) leads to a singularity in $W_S(f)$ at the origin.

Many features of the spectra shown in Figs. 3 and 4 have been observed by experiment at various microwave and laser frequencies in the earth's atmosphere (Refs. 26-29). The most consistent is the -8/3 slope at the higher fluctuation frequencies, which is a consequence and therefore verification of the Kolmogorov spectrum. The breakpoint in $W_\chi(f)$ which occurs at approximately $f = f_\perp$ has also been used to derive estimates of c_n and $v_\perp$ (Refs. 25, 28).

As previously mentioned, an important parameter in the frequency spectra for the communications engineer is the bandwidth. Denoting the frequency corresponding to the half power point for $L_o = \infty$, f_{3dB}, we have

$$f_{3dB} = 1.847\, f_\perp = 0.294\, v_\perp \sqrt{\frac{k}{L}} \tag{27}$$

We note that neither the shape nor the half power point of the log-amplitude spectrum is dependent on c_n or σ_χ^2. On the other hand, f_{3dB} is proportional to $v_\perp$. It is also clear from Fig. 3 that the dependence of bandwidth on L_o is very small. This of course means that the choice of either (9) or (10) as the spectrum has little effect on the bandwidth. The spectra given in Figs. 3 and 4 and (27) should be valid for $L >> \sqrt{\lambda \ell_o}$, where ℓ_o is the inner scale of turbulence. In the earth's atmosphere, ℓ_o is of the order of 1 cm. If we assume a similar value for Venus, the spectra and (27) should be valid for distances as short as 0.036 m. An interesting result of (27) is that the spectrum becomes narrower as the entry probe penetrates deeper into the Venusian atmosphere. Actually, this is not surprising in view of the fact that at a distance L, the predominant scale size is the Fresnel-zone size $\sqrt{\lambda L}$ (Refs. 9, 18). Thus, for longer L, the predominant scale size increases, and the contribution to the lower frequencies in the frequency spectrum correspondingly increases since $v_\perp$ remains constant. To summarize, as L increases the frequency spectrum becomes narrower even though the variance increases.

We have obtained estimates for Pioneer Venus based on the values of structure constant and $v_\perp$ inferred from Venera 4 and these are shown in Table 1. Venera 4 is the worst case analysis since the peak horizontal wind velocity and structure constant inferred from Venera 4 were twice those inferred from Venera 7. Additional calculations of f_{3dB} are summarized in Fig. 5.

The results discussed so far assume that the sub-earth direction corresponds to the zenith of Venus (Fig. 1). If the sub-earth direction makes an angle θ with the zenith of Venus, then L in (12), (15) and (27) must be replaced

by L sec θ, while $v_\perp$ in (27) must be replaced by $v_\perp \cos\theta$. These results are, of course, not valid when θ is large ($\theta \simeq 90°$). We see that while σ_χ^2 and σ_ϕ^2 increase with θ, the spectra become narrower. Thus as far as the bandwidth is concerned, $\theta = 0$ represents the worst case.

In conclusion, let us once again emphasize that our predictions for Pioneer Venus rely heavily on our knowledge of the dependence of the structure constant on altitude and the measurement and calculation of σ_χ^2 from the Venera radio data. Let us further point out that σ_χ^2 has a very small value and is consequently subject to substantial experimental error. More important, however, is the fact that we have little assurance that the fluctuations are due to turbulence and not noise or some other cause such as absorption layers in the atmosphere or spacecraft motion. Computation of the frequency spectrum in addition to σ_χ^2 and its comparison with the spectrum shown in Fig. 3 would go a long way toward providing supporting evidence for atmospheric turbulence. Although some form of spectral analysis was performed on the Venera data (Ref. 30), its purpose was not to compare the spectrum with theory. There are two reasons for raising this point. First of all, we will demonstrate the importance and usefulness of the spectrum in our analysis of the Mariner 5 data in the following section. Secondly, it should be apparent from our discussion that with proper analysis, the Pioneer Venus radio link could be utilized to provide valuable information on turbulence in the atmosphere of Venus.

IV. Observations of Turbulence in the Atmosphere of Venus by Mariner 5

It should be clear from the previous section that in order to make engineering estimates for Pioneer Venus, we must have information on the turbulence characteristics of the atmosphere of Venus and how it interacts with wave propagation. On the other hand, the only way we are going to gain this knowledge is through interpretation of radio signals received from previous missions to Venus. The engineering and scientific aspects of atmospheric turbulence are therefore closely related, and consideration of one cannot be made without the other. It is obvious that in spite of the Venera missions, our knowledge about turbulence in the atmosphere of Venus is severely limited. The confidence in our predictions for Pioneer Venus would be enhanced if similar results could be obtained based on the radio data of Mariner 5. However, since Mariner 5 was a fly-by mission, new techniques for analysis and data interpretation will have to be developed.

Let us first review what has been done with the Mariner 5 data to date. In his study, Gurvich (Ref. 17) computed the variance of log-amplitude fluctuations σ_χ^2 for Mariner 5 during occultation using the published results of Kliore, et. al. (Ref. 31). The structure constant inferred from σ_χ^2 was found to be at least two orders of magnitude lower than that inferred from Venera 4. De Wolf (Refs. 22, 23) also investigated Mariner 5, and concluded that the observed scintillations were much weaker than those that would have been predicted from the observed Venera 4 scintillations because the Mariner 5 fluctuations had been smoothed by data processing. Golitsyn and Gurvich (Ref. 32) examined the feasibility of extracting the turbulence-induced fluctuations from the noisy Mariner 5 exit occultation radio signal, and concluded that the signal-to-noise ratio was sufficiently high in the S-band

link. In a recent paper, Woo and Ishimaru (Ref. 18) showed that the analysis employed by Gurvich (Ref. 17), although adequate for entry missions, was inadequate for fly-by missions because it neglected the effects of turbulence inhomogeneity and finite extent in the direction transverse to the direction of propagation. A new analysis for σ_χ^2 was developed and it was shown that the structure constant inferred from Mariner 5 was within an order of magnitude of that inferred from Venera 4.

In a totally different interpretation, Rasool (Ref. 33) suggests that the rapid changes in the Mariner 5 amplitude data may be due to absorption by cloud layers containing substantial amounts of Hg and its compounds. Thus, even the presence of turbulence effects in the Mariner 5 data is questionable.

It is clear that a careful and thorough study of the amplitude and phase fluctuations of Mariner 5 is highly desirable. This study should be based on the power spectra of the amplitude and phase fluctuations instead of just the variances. Two approaches should be used: a theoretical analysis of Mariner 5 and spectral analysis of the Mariner 5 occultation data. It should be pointed out that the power spectra and phase fluctuations have never been studied in previous work. We have undertaken such a study of Mariner 5 and its purpose is (1) to examine and ascertain the effects of data processing, (2) to distinguish turbulence-induced fluctuations from those due to noise, (3) to obtain supporting evidence of atmospheric turbulence in the atmosphere of Venus, (4) to derive the theoretical spectra for the turbulence-induced fluctuations of Mariner 5, (5) to infer the turbulence characteristics of the Venusian atmosphere by comparing the processed and theoretical spectra, and (6) to compare the inferred results of Mariner 5 with those of Venera 4 - 7 in order to enhance our confidence in our estimates for Pioneer Venus. The results obtained so far and described in this report are those based on the amplitude fluctuations.

4.1 Mariner 5 Processed Results

Although the Mariner 5 occultation data were processed in previous work (Refs. 31, 34 and 35), the primary interest was the average atmosphere so that substantial smoothing was generally introduced into the data and little attention was paid to the very delicate measurement of variance. Since we are interested in the fluctuations, we have had to reprocess the Mariner 5 data, a somewhat difficult task in view of the age and volume of the data.

A complete description of data processing would make this section prohibtively long. We have therefore described most of the details in Appendix A, which is organized in the following manner. In A.1 signal reception and pre-processing are discussed. The pre-processing includes digitization, frequency shifting, filtering and decimation of the original Mariner 5 analog tapes. In the present study, the starting point is the digitized tapes. The phase-locked-loop processing is described in A.2 and consists of a discussion of amplitude and phase extraction, errors and tracking. Finally in A.3 we present an account of the amplitude spectrum calculation.

As mentioned earlier, the results obtained to date deal only with the amplitude fluctuations. Although they are preliminary, they are nevertheless significant. The signal level as a function of time during entrance and exit occultation is shown in Figs. 6 and 7, respectively. These results are similar to those previously published (Refs. 31 and 32). We have also indicated the altitudes corresponding to the lowest penetration of the propagation path. The information contained in Ref. 35 was used for the case of entrance occultation while that in Ref. 32 for the case of exit occultation. We expect to obtain more accurate data on the exit case in the future. We have divided Figs. 6 and 7 into three regions: A, B and C. The reason for this is that the fluctuations

in Figs. 6 and 7 suggest noise in regions A and C and turbulence in region B which corresponds to the approximate altitude range of 41 - 49 km. Of course, verification of these results will emerge from the spectral study. As discussed in Appendix A, we fit quadratic time functions to Figs. 6 and 7 assuming that they represent the average atmospheric attenuation as well as the changing antenna pointing and earth-spacecraft distance effects. The quadratic time function is then subtracted from the data in Figs. 6 and 7 and the results spectrum analyzed.

The power spectra of the amplitude fluctuations for the various regions are shown in Figs. 8 - 12. At the writing of this report only the results for region A of the entrance case had not been completed. The spectra are plotted for frequencies up to $1/2\pi\tau_{AGC}$ since this is the maximum frequency at which amplitude fluctuations may be observed (see Appendix A). Noise levels as well as 90% confidence intervals were calculated using the formulas developed in Appendix A and are shown on the various spectra. The 90% confidence interval is indicated by error bars. Errors of the spectral estimates are expected to lie within the error bars in 90% of all cases. For smoothing, we used running point averages consisting of 11, 21, 31, 41 and 51 points (m is the number of points).

Let us first examine the results obtained for the exit case. It is apparent that the spectra of regions A and C do indeed resemble noise (flat spectrum), and that in contrast the spectrum for region B shows structure above the noise level at the lower frequencies. The calculated noise levels seem to agree with the apparent noise levels in the spectra. The spectra for the entrance case are similar to those for the exit case. In region B the apparent noise level appears to be twice as high as the calculated noise level. The important point, however, is that again the spectrum in region B has structure.

A careful examination of the results for region B reveals the difficulties involved in spectral analyzing the Mariner 5 data. On one hand, because the spacecraft is moving very fast, the record length available for spectral analysis is very short. As a result, there is a severe limitation on the low frequency end of the spectrum. On the other hand, the signal-to-noise ratio is so low that the spectrum very quickly reaches the noise level at the high frequency end of the spectrum. As a result, frequency averaging would make the already very narrow frequency range of the spectrum even narrower. Fortunately, despite these limitations, the results are good enough to allow the distinction and separation of noise and structure.

We have utilized the computer to calculate the probability density function of $\chi = \ell n \frac{A}{A_o}$, the log-amplitude fluctuations. The result for Region B in the entrance case is shown in Fig. 13. It can be seen that the probability density function for χ resembles a gaussian function, so that the probability density function for A would be log-normal as expected if the fluctuations were turbulence-induced (see Section III). It should be pointed out that for small fluctuations, the difference between log-normal and gaussian functions would be small. The result in Fig. 13 is consequently not too meaningful.

Although the structure in the spectra of region B is very likely due to turbulence-induced fluctuations, we definitely need additional supporting evidence. We hope to provide part of this with the results of our theoretical study which will be discussed in the next section. For the moment, we will assume that the structure in the spectra in region B represents turbulence. The processed results, therefore, indicate that turbulence exists predominantly in the altitude range of 41 - 49 km in the atmosphere of Venus. It is interesting to point out that strong wind shear, a condition necessary for the existence of turbulence, was indeed observed at altitudes higher than 40 km by Venera 4 (Ref. 16) and more recently

by Venera 8 (Ref. 37). Kerzhanovich, et. al. (Ref. 16) have recently discussed the presence of turbulence in the altitude range 45 - 53 km in view of the wind velocity observations of Venera 4. The processed results of Mariner 5 are therefore significant because they furnish for the first time information on the variation of turbulence in the atmosphere of Venus as a function of altitude.

4.2 Mariner 5 Theoretical Results

The results obtained in Section 4.1 indicate that turbulence in the atmosphere exists predominantly in the altitude range of 41 - 49 km. We will therefore assume that the structure constant c_n has the following spatial variation

$$c_n^2(x_c,y_c,z_c) = c_{no}^2 \exp\left[- \left(\frac{x_c - L}{a}\right)^2 - \left(\frac{y_c}{b}\right)^2 - \left(\frac{z_c}{a}\right)^2 \right] \tag{28}$$

where the coordinate system is depicted in Fig. 14 and the peak structure constant c_{no} occurs at the altitude of 45 km. The extent of the turbulence in the $x_c - z_c$ plane is characterized by a, while that in the y_c direction by b. These two characteristic distances are approximately related by the following relationship (see Fig. 14):

$$a = 6095 \tan\theta \tag{29}$$

$$\cos^{-1}\theta = \frac{6095}{6095 + b}$$

where a and b are in kilometers and the radius of the planet Venus is assumed to be 6050 km. Since the turbulence exists in the altitude range of 41 - 49 km, b is expected to lie in the range 4 - 6 km. The corresponding range for a is 220 - 270 km. It should be pointed out that (28) assumes essentially no turbulence

for altitudes less than 35 km. Of course no information was provided by Mariner 5 since it did not probe below this altitude on account of super-refractivity. We will discuss this point further later in the report.

Since the outer scale size L_o is expected to be somewhere around 100 m, the distance L (see Fig. 14) which is of the order of 10^4 km substantially exceeds kL_o^2. The theory for wave propagation in homogeneous turbulence utilized in Section III for analyzing entry missions such as Venera and Pioneer Venus is therefore no longer adequate (Refs. 18 and 36). To account for the effects of turbulence inhomogeneity and finite extent in the direction transverse to the direction of propagation, the planetary atmosphere is represented by a localized homogeneous and isotropic turbulence with smoothly-varying mean characteristics. Although a general study of the variances of log-amplitude and phase fluctuations for wave propagation in localized turbulence has been conducted (Ref. 36), no study of the corresponding frequency spectra has ever been made. Furthermore, the results described in Refs. 18 and 36 do not include the effects of the moving spacecraft. The mathematical details of the present theoretical study are rather involved and consequently described in Appendix B. The formulation of the general problem of wave propagation in localized smoothly-varying turbulence is given in B.1. The variances are derived in B.2 and the frequency spectra in B.3 and B.4.

For the sake of comparison we will normalize the frequency spectra of the log-amplitude and phase fluctuations, $W_\chi(f)$ and $W_S(f)$, respectively, to their values at $f = 0$. $W_\chi(0)$ and $W_S(0)$ can be obtained from (91) - (95) in Appendix B:

$$W_\chi(0) = K'(W_1' - W_2') \tag{30}$$

$$W_S(0) = K'(W_1' + W_2') \tag{31}$$

where

$$K = 0.033\, c_{no}^2\, 4\,\pi^3\, \frac{L_o^{8/3}}{v}\, k^2 a \exp\left[-\left(\frac{vt_c}{b}\right)^2\right]$$

$$W_1' = \frac{\Gamma\left(\frac{4}{3}\right)}{\Gamma\left(\frac{11}{6}\right)}$$

$$W_2' = \sqrt{\frac{k}{L}}\, L_o \cos\frac{\pi}{4}$$

Some typical normalized spectra of the log-amplitude fluctuations are plotted in Figs. 15 - 17. The most prevalent result is that the major contribution to the spectra occurs at a frequency approximately equal to $\frac{1}{2\pi}\frac{v}{L_o}$. In other words, the predominant scale size is L_o. This is reasonable since the predominant scale size is the Fresnel-zone size $\sqrt{\lambda L}$ when $L << kL_o^2$. When $L >> kL_o^2$, as is the case in Mariner 5, the largest scale size is L_o and this then becomes the predominant scale size.

The spectra in Figs. 15 - 17 correspond to the range of parameters expected for entrance and exit occultation of Mariner 5. Several features are apparent. First of all, there is little difference between the spectra for entrance and exit occultation. Secondly, the shape of the spectrum depends to a large extent on the values of b and L_o. Thirdly, the shape of the spectrum is not dependent on velocity v, at least for the range of values considered (100 - 150 m/sec). In the next section we will compare the theoretical spectra with the processed spectra of Mariner 5 and infer the turbulence characteristics of the Venusian atmosphere.

4.3 Turbulence Characteristics of the Atmosphere of Venus

We have compared the theoretical spectra in Figs. 15 and 16 with the processed spectra of Mariner 5 for region B (Figs. 9 and 11). We selected a best fit theoretical curve by adjusting only the ordinate. The best fit for both entrance and exit occultation occurs when L_o = 100 m, b = 6 km and the corresponding value of a is 270 km. We have superimposed this best fit on the spectra with varying amounts of frequency averaging in Figs. 9 and 11 and the agreement is remarkable. It can be seen that the theoretical spectra serve very well to define the shape of the processed spectra.

The processed spectra indicated the existence of turbulence in the approximate altitude range of 41 - 49 km. The y_c dependence of c_n is plotted in Fig. 18 and it can be seen that the value of 6 km obtained for b in the best fit theoretical curve is consistent with the altitude variation obtained in Section 4.1.

If we examine the theoretical spectra plotted in Figs. 15 and 16 we see that they depend on v, L, b, a and L_o. We know v and L to a good degree of accuracy from the trajectory information and b and a to a reasonably good degree from the data in Figs. 6 and 7 and the processed spectra. As a result, the process of matching the theoretical and processed spectra essentially provides a valuable means for measuring L_o. In the case of Pioneer Venus, the phase fluctuations depend very much on scattering from large eddies of turbulence. The outer scale size L_o defines the largest scale size of turbulence and consequently is an important parameter for predicting the phase fluctuations of Pioneer Venus (see equation 15 in Section II). A discussion is given in Ref. 16 pointing out that the expected L_o for the Venusian atmosphere would be larger than that of the earth's atmosphere. In the earth's atmosphere L_o generally lies in the range of 10 - 50 m. The correlation function of the fluctuations of wind velocity inferred from

Venera 4 also indicates that L_o would measure 100 - 200 m (Ref. 16). Thus, the estimate of L_o derived from Mariner 5 is consistent with these aforementioned results.

Let us infer the peak structure constant c_{no} from σ_χ^2. For entrance occultation σ_χ^2 was 1.856×10^{-2} while for exit occultation σ_χ^2 was 3.398×10^{-2}. It comes as no surprise that these results are considerably higher than those obtained by Golitsyn and Gurvich (Ref. 32). It is obvious that too much smoothing was used in the data studied by Golitsyn and Gurvich, so that the contribution from the higher frequencies was lost. This of course points up the necessity of a spectral analysis even if one is only interested in the variance and supports our concern that the measurement of variance due to turbulence in the case of Venera may be inaccurate.

The appropriate region for the values obtained for L_o, b and a is region II (see Fig. B-4 in Appendix B) and we will use (49) in Appendix B to infer c_{no}. For the nightside atmosphere,

$$c_{no} = 2.9 \times 10^{-7}\ m^{-1/3} \tag{32}$$

while for the dayside atmosphere,

$$c_{no} = 3.9 \times 10^{-7}\ m^{-1/3} \tag{33}$$

As would be expected, the dayside atmosphere is more turbulent than the nightside atmosphere. However, since the difference in temperature between the dayside and nightside atmospheres is small (Ref. 35), the differences in c_{no} would also be expected to be small.

In summary, the results obtained from Mariner 5 consistently support the assumption that the fluctuations observed are indeed turbulence-induced. It should also be pointed out that since Kolmogorov's spectrum was used in our

theoretical spectra, the good agreement with the processed spectra provides evidence that the turbulence is indeed fully developed. In our future work we hope to study the effect of the shape of the spectrum of the refractive index fluctuations on $W_\chi(f)$.

4.4 Comparison of Mariner 5 and Venera Results

As mentioned in the previous section, the wind velocity profiles measured by Venera 4 showed high wind velocities and wind shear above 40 km and low wind velocities below. The processed results of Mariner 5 indicate that turbulence begins to disappear for altitudes lower than 40 km and are consistent with the Venera wind velocity observations. Thus, even though Mariner 5 only probed to an altitude of 35 km, it is reasonable to expect that the turbulence would continue to be absent or remain weak from 35 km down to the surface of the planet. The lack of turbulence in the lower atmosphere could be explained by the fact that large amounts of energy that might not be available are required to move the very dense atmosphere.

Our predictions for Pioneer Venus in Section III were based on a model of the turbulent atmosphere characterized by c_n being constant from 0 to 55 km and zero above 55 km. Let us re-examine these predictions in view of the Mariner 5 findings. We will assume the variation of c_n shown in Fig. 19; c_n is constant ($c_n = c_{no}$) in the altitude range 41 - 49 km and zero elsewhere. Using (11) we obtain the following result:

$$\sigma_\chi^2 = 0.308\, k^{7/6}\, L_2^{11/6} \left[1 - \left(\frac{L_1}{L_2}\right)^{11/6}\right] c_{no}^2 \qquad (34)$$

When $L_1 = 0$, (34) reduces to (12). As in Section III, we will infer c_{no} from the measurement of σ_χ^2 by Venera 7 ($\sigma_\chi^2 = 5.3 \times 10^{-2}$). For $L_1 = 41$ km and $L_2 = 49$ km, we obtain

$$c_{no} = 2.1 \times 10^{-6}\ m^{-1/3} \tag{35}$$

Comparing (35) with (13) we see that the difference is small. The predictions made for Pioneer Venus in Section III therefore remain representative.

Comparing (35) with (32) and (33), we find that c_n inferred from Mariner 5 is within an order of magnitude of that inferred by Venera 7. The important point however is that confidence in our predictions for Pioneer Venus has been greatly enhanced as a result of the Mariner 5 study.

V. Venus Radar Experiment

An additional crude estimate of radio spectral broadening due to turbulence in the Venusian atmosphere can be made obtained by analyzing the received spectra from the Venus radar experiment.

During his radar scan of Venus, Goldstein (Ref. 38) reported that the observed spectral broadening between the half power points was 0.07 Hz. We can use (27) to obtain a crude estimate of $v_\perp$ by taking L to be twice the extent of the atmosphere, i.e., 110 km. We obtain $v_\perp$ = 0.9 m/sec which is within an order of magnitude of the average $v_\perp$ observed on Venera 7 (Ref. 16).

VI. Summary and Conclusions

We have shown that our ability to determine the effects of turbulence in the atmosphere of Venus on Pioneer Venus radio depends a great deal on our knowledge of the turbulence. Although very little is known about the turbulence in the Venusian atmosphere, valuable information can be inferred from the radio link of spacecraft that have probed the planet's atmosphere. These of course include the Venera and Mariner 5 spacecraft. Our predictions for Pioneer Venus, therefore, rely heavily on radio measurements of the Venusian atmosphere made by previous space probes.

Even though Venera 7 reached the surface of Venus, the information provided on atmospheric turbulence was very limited. Still, we estimated the effects of turbulence on Pioneer Venus based on Venera 7, but pointed out the urgent need for additional turbulence information to establish confidence in the estimates.

In an effort to increase our understanding of turbulence in the atmosphere of Venus, we have conducted a thorough and careful investigation of the Mariner 5 occultation data. The results described in this report were obtained by studying the amplitude fluctuations. Unlike previous work, the present study is based on the power spectrum rather than the variance of the amplitude fluctuations. The results obtained so far have considerably advanced our scientific knowledge of turbulence in the atmosphere of Venus. These results were made possible by the development of new techniques in two major areas: data processing and theory of wave propagation in turbulent medium. The study of data processing revealed its effect on the amplitude fluctuations and enabled noise to be distinguished from the turbulence-induced fluctuations. On the

other hand, the theoretical study of wave propagation in localized smoothly varying turbulence led to the theoretical prediction of the variance and power spectrum of the Mariner 5 amplitude fluctuations.

The results obtained with Mariner 5 can be summarized as follows. Mariner 5 provides evidence of turbulence in the atmosphere of Venus, and for the first time, information on its variation with altitude down to 35 km. The remarkable agreement between the processed and theoretical power spectra of the amplitude fluctuations furnishes strong evidence that the fluctuations are indeed turbulence-induced. Turbulence exists predominantly in the 41 - 49 km altitude range, and appears to be fully developed since Kolmogorov's spectrum was used to describe the refractive index fluctuations. The variation of turbulence with altitude is consistent with the high wind velocities and wind shear observed by Venera 4 above 40 km. The outer scale size of turbulence L_o is on the order of 100 m. The inferred structure constant for the dayside atmosphere is $3.9 \times 10^{-7}\ m^{-1/3}$ and, as expected, it is slightly lower for the nightside atmosphere ($2.9 \times 10^{-7}\ m^{-1/3}$).

It is shown that the structure constants inferred from Mariner 5 are within an order of magnitude of that inferred from Venera 7. The estimates made for Pioneer Venus radio which were based on Venera 7, therefore, remain valid. The significant result of our study of Mariner 5 is that the confidence in our estimates for Pioneer Venus has been greatly enhanced.

Our estimates for Pioneer Venus indicate that the variance of log-amplitude fluctuations should be less than 0.056, the variance of phase fluctuations less than 0.88 rad^2, and the bandwidth of both amplitude and phase fluctuations no more than a few Hz.

In future work we plan on (1) reducing and inferring turbulence from the Mariner 5 phase data, (2) studying the dependence of the Pioneer Venus power spectra of amplitude and phase fluctuations on wind velocity distribution and spectrum of refractive index fluctuations and (3) studying the cross correlation between amplitude and phase fluctuations for Pioneer Venus.

References

1. Tatarski, V. I., "Wave Propagation in a Turbulent Medium", McGraw-Hill, New York, 1961.

2. Tatarski, V. I., "The Effects of the Turbulent Atmosphere on Wave Propagation", Nauka, Moscow, 1967. Translated and available from the U.S. Dept. of Commerce, Springfield, Va.

3. Batchelor, G. K., "Homogeneous Turbulence", Cambridge University Press, Cambridge, England, 1953.

4. Lumley, J. L. and Panofsky, H. A., "The Structure of Atmospheric Turbulence", John Wiley and Sons, New York, 1964.

5. Panchev, S., "Random Functions and Turbulence", Pergamon Press, Oxford, 1971.

6. Wheelon, A. D., "Radio Wave Scattering by Tropospheric Irregularities", J. Res. NBS (Radio Propagation), Vol. 63D, pp. 205-233, September-October, 1959.

7. Wheelon, A. D., "Radio Scattering by Tropospheric Irregularities", J. Atmosph. Terrest. Phys., Vol. 15, pp. 185-205, 1959.

8. Strohbehn, J. W., "Line-of-Sight Wave Propagation Through the Turbulent Atmosphere", Proc. of the IEEE, Vol. 56, No. 8, pp. 1301-1318, August, 1968.

9. Lawrence, R. W. and Strohbehn, J. W., "A Survey of Clear-Air Propagation Effects Relevant to Optical Communications," Proc. of the IEEE, Vol. 58, No. 10, pp. 1523-1545, October 1970.

10. Clifford, S. F. and Strohbehn, J. W., "The Theory of Microwave Line-of-Sight Propagation Through a Turbulent Atmosphere", IEEE Trans. Antennas and Propagation, Vol. 18, No. 2, pp. 264-274, March 1970.

11. Barabznenkov, Yu.N., Kravstov, Yu.A., Rytov, S. M., and Tamarskii, V. I., "Status of the Theory of Propagation of Waves in a Randomly Inhomogeneous Medium", Usp. Fiz. Nank, Vol. 102, pp. 3-42, September 1970. Translated in Soviet Physics Uspekhi, Vol. 13, No. 5, pp. 551-680, March-April, 1971.

12. Brookner, E., "Atmosphere Propagation and Communication Channel Model for Laser Wavelengths", IEEE Trans. Comm. Technology, Vol. 18, No. 4, August 1970.

13. Brookner, E., "Atmospheric Propagation and Communication Channel Characterization at Optical Wavelengths", paper presented at the 1972 URSI Fall Meeting in Williamsburg, Va., December, 1972.

14. Kerr, J. R., et. al., "Atmospheric Optical Communications Systems", Proc. of the IEEE, Vol. 58, pp. 1691-1709, October, 1970.

15. Fried, D. L., "Aperture Averaging of Scintillation", J. of Opt. Soc., Vol. 57, No. 2, pp. 169-180, February 1967.

16. Kerzhanovich, V. V., Yarov, M. Ya., and Rozhdestvensky, M. K., "Data on Dynamics of the Subcloud Venus Atmosphere from Venera Spaceprobe Measurements", Icarus, Vol. 17, pp. 659-674, December 1972.

17. Gurvich, A. S., "An Estimate of the Parameters of Small-Scale Turbulence in the Atmosphere of Venus Obtained from Fluctuations of Radio Signals from Venus-4 and Mariner-5", Dokl. Akad. Nauk. SSSR, Vol. 5, No. 11, pp. 1172-1178, 1969.

18. Woo, R. and Ishimaru, A., "Remote Sensing of the Turbulence Characteristics of a Planetary Atmosphere by Radio Occultation of a Space Probe", Radio Science, Vol. 8, No. 2, pp. 103-108, February, 1973.

19. Kolosov, M. A., Yakovlev, O. I., and Yefimov, A. I., "Study of the Propagation of Decimeter Radiowaves in the Atmosphere of Venus with the Aid of AIS Venera-4", Dokl. Akad. Nauk SSSR, Geofiz., Vol. 182, No. 1, pp. 93-94, 1968.

20. Kolosov, M. A., Yakovlev, O. I., and Yefimov, A. I., "Propagation of Radiowaves in the Atmosphere of Venus from the Data of Venus-4, Venus-5 and Venus-6", Radio Engr. and Elect. Phys., Vol. 15, No. 12, pp. 2183-2188, 1970.

21. Yakovlev, O. I., Efimov, A. I., and Timofeeva, T. S., "Venera-7 Spaceprobe Data on Propagation of Radio Waves Through the Venusian Atmosphere and Through the Interplanetary Plasma", Kosm. Issle., Vol. 9, No. 5, pp. 748-753, September-October, 1971.

22. De Wolf, D. A., "Evidence for Severe Microwave Signal Fading in the Atmosphere of Venus due to Turbulence", J. of Geophys. Research, Vol. 75, No. 7, pp. 1202-1208, March, 1970.

23. De Wolf, D. A., "Atmospheric Turbulence on Venus: Venera 4, 5, 6 and Mariner 5 Estimates", J. of Geophys. Research, Vol. 76, No. 13, pp. 3154-3158, May 1971.

24. Hufnagel, R. E. and Stanley, N. R., "Modulation Transfer Function Associated with Image Transmission Through Turbulent Media", J. of Opt. Soc., Vol. 54, No. 1, pp. 52-61, January 1964.

25. Ishimaru, A., "Temporal Frequency Spectra of Multifrequency Waves in Turbulent Atmosphere", IEEE Trans. Antennas and Propagation, Vol. 20, No. 1, pp. 10-19, January 1972.

26. Janes, H. B., Thompson, M. C., Smith, D., and Kirkpatrick, A. W., "Comparison of Simultaneous Line-of-Sight Signals at 9.6 and 34.5 GHz", IEEE Trans. Antennas and Propagation, Vol. AP-18, No. 4, July 1970.

27. Beard, C. I., "Phase Quadrature Components of the 10.4 GHz Scattered Field on a Short Tropospheric Path", Proc. of IEEE, Vol. 56, pp. 1398-1399, August 1968.

28. Mandics, P. A., Lee, R. W., and Waterman, Jr., A. T., "Spectra of Short-Term Fluctuations of Line-of-Sight Signals: Electromagnetic and Acoustic", Radio Science, Vol. 8, No. 3, pp. 185-201, March 1973.

29. Kerr, J. R., "Experiments on Turbulence Characteristics and Multiwavelength Scintillation Phenomena", J. of Opt. Soc., Vol. 62, No. 9, pp. 1040-1049, September 1972.

30. Aleksandrov, Yu.N., Rzhiga, O. N., and Shakhovskoi, A. M., "Digital Computer Analysis of Radio Signals Transmitted by the Soviet Venera-7 Interplanetary Station Landing on the Surface of Venus", Kosm. Issle., Vol. 9, No. 6, pp. 904-911, November-December 1971.

31. Kliore, A., Levy, G. S., Cain, D. L., Fjeldbo, G., and Rasool, S. I., "Atmosphere and Ionosphere of Venus from the Mariner 5 S-Band Radio Occultation Measurement", Science, Vol. 158, No. 3809, pp. 1683-1688, December 29, 1967.

32. Golitsyn, G. S. and Gurvich, A. S., "An Estimate of Refractive Index Fluctuations in the Venus Atmosphere from Mariner 5 Data", J. of Atm. Sci., Vol. 28, pp. 138-140, January 1971.

33. Rasool, S. I., "The Structure of Venus Clouds — Summary", Radio Science, Vol. 5, No. 2, pp. 367-368, February 1970.

34. Kendall, W. B., "A Precision Frequency Measurement Technique for a Moving Signal with a Low Signal-to-Noise Ratio", IEEE Trans. on Instr. and Meas., Vol. IM-17, No. 4, pp. 358-365, December 1968.

35. Fjeldbo, G., Kliore, A. J. and Eshleman, Von R., "The Neutral Atmosphere of Venus as Studied with the Mariner 5 Radio Occultation Experiments", Astron. J., Vol. 76, No. 2, pp. 123-140, March 1971.

36. Ishimaru, A., "A New Approach to the Problem of Wave Fluctuations in Localized Smoothly Varying Turbulence", IEEE Trans. Antennas and Propagation, Vol. AP-21, No. 1, January 1973.

37. Marov, M. Ya., et. al., "Preliminary Results of Measurements of the Venera 8 Automatic Spacecraft", Predvaritel'nyye Rezul'taty Izmereniy AMS 'Venera-8, Academy of Sciences, USSR, Moscow, 1973, Unpublished Report, NASA Technical Translation, NASA TT F-14, 909.

38. Goldstein, R. M., Correspondence to T. Grant of Ames Research Center dated July 14, 1972.

TABLE 1

L, km	σ_χ^2	σ_χ	σ_ϕ^2, rad^2	σ_ϕ, rad	f_{3dB}, Hz
55	0.056	0.2378	0.2282	0.472	0.436
30	0.018	0.136	0.134	0.367	0.59
10	0.0025	0.05	0.05	0.22	1.02
5	0.0007	0.026	0.025	0.16	1.45
1	4×10^{-5}	0.006	0.005	0.071	3.23

$c_n = 2.024 \times 10^{-6}$ m $^{-1/3}$ (inferred from Venera 4)

$v_\perp = 50$ m/sec and uniform (Venera 4 data)

Note that σ_χ^2, σ_χ, σ_ϕ^2 and σ_ϕ are independent of $v_\perp$

Table 1. Summary of Log-Amplitude and Phase Fluctuation Results

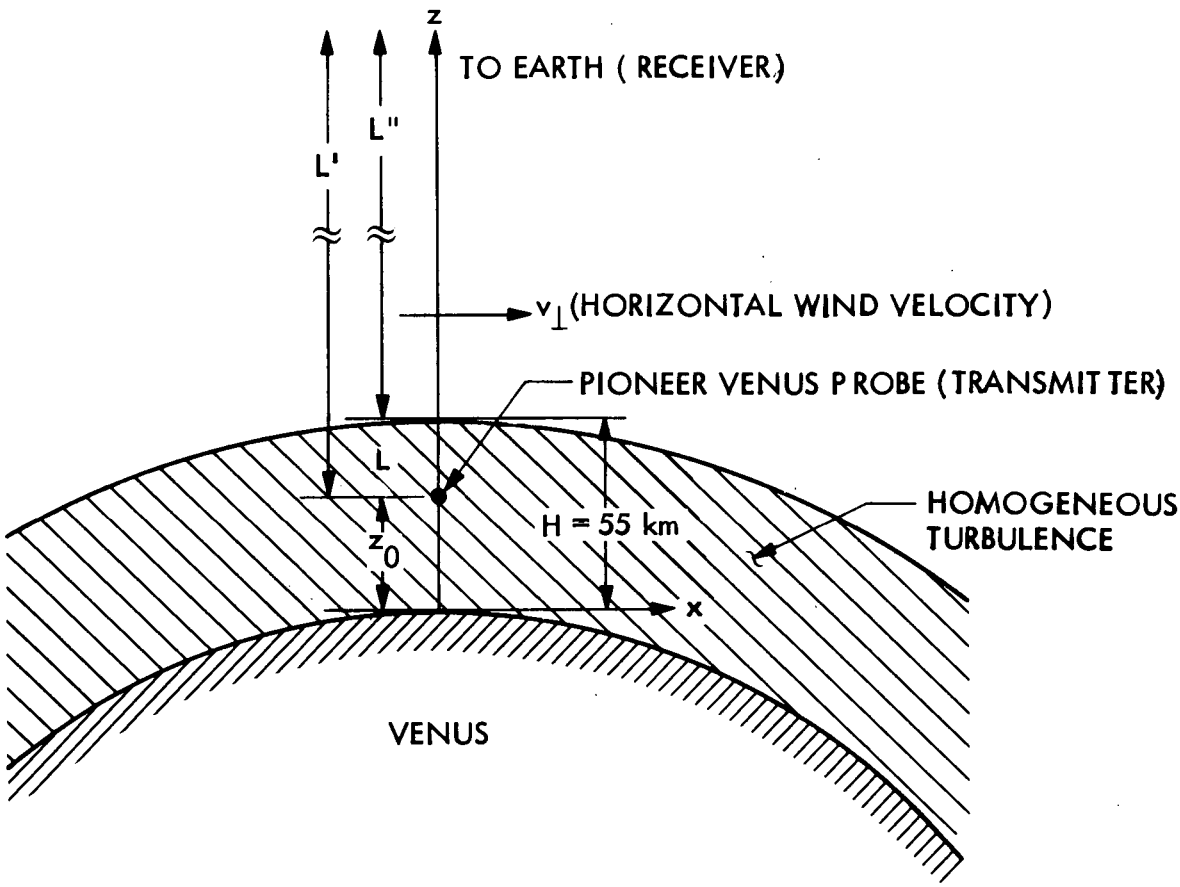

Figure 1. Pioneer Venus Entry Configuration

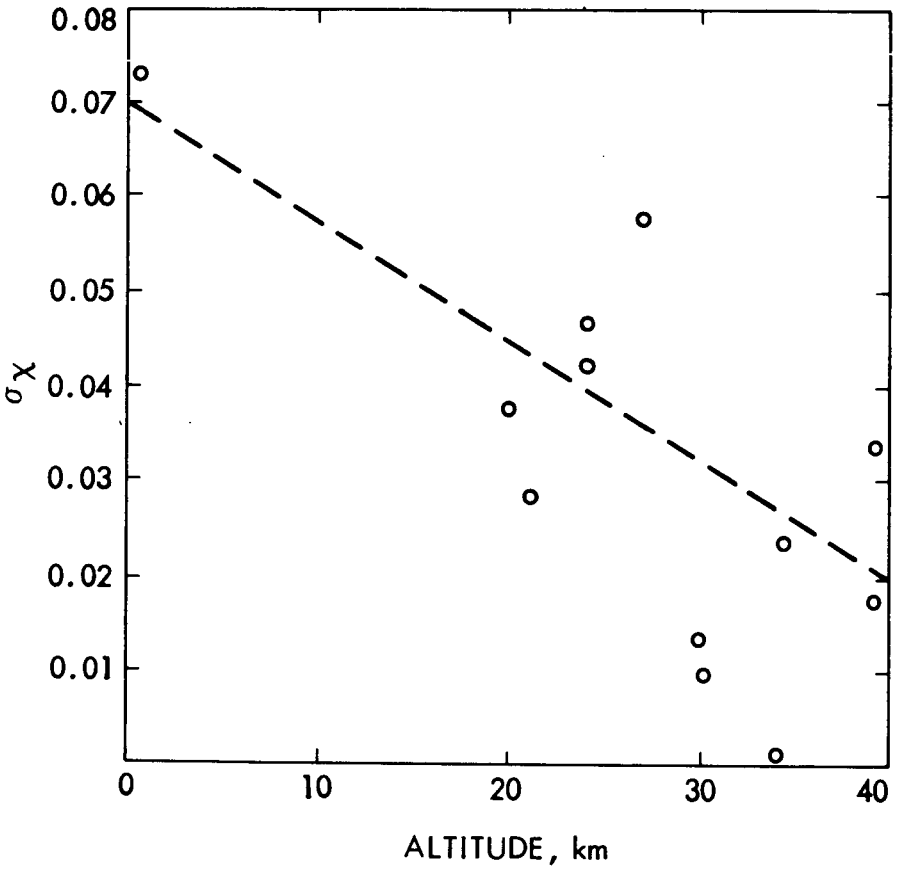

Figure 2. σ_χ for Veneras 5-7 as a Function of Altitude. Taken from Reference 21.

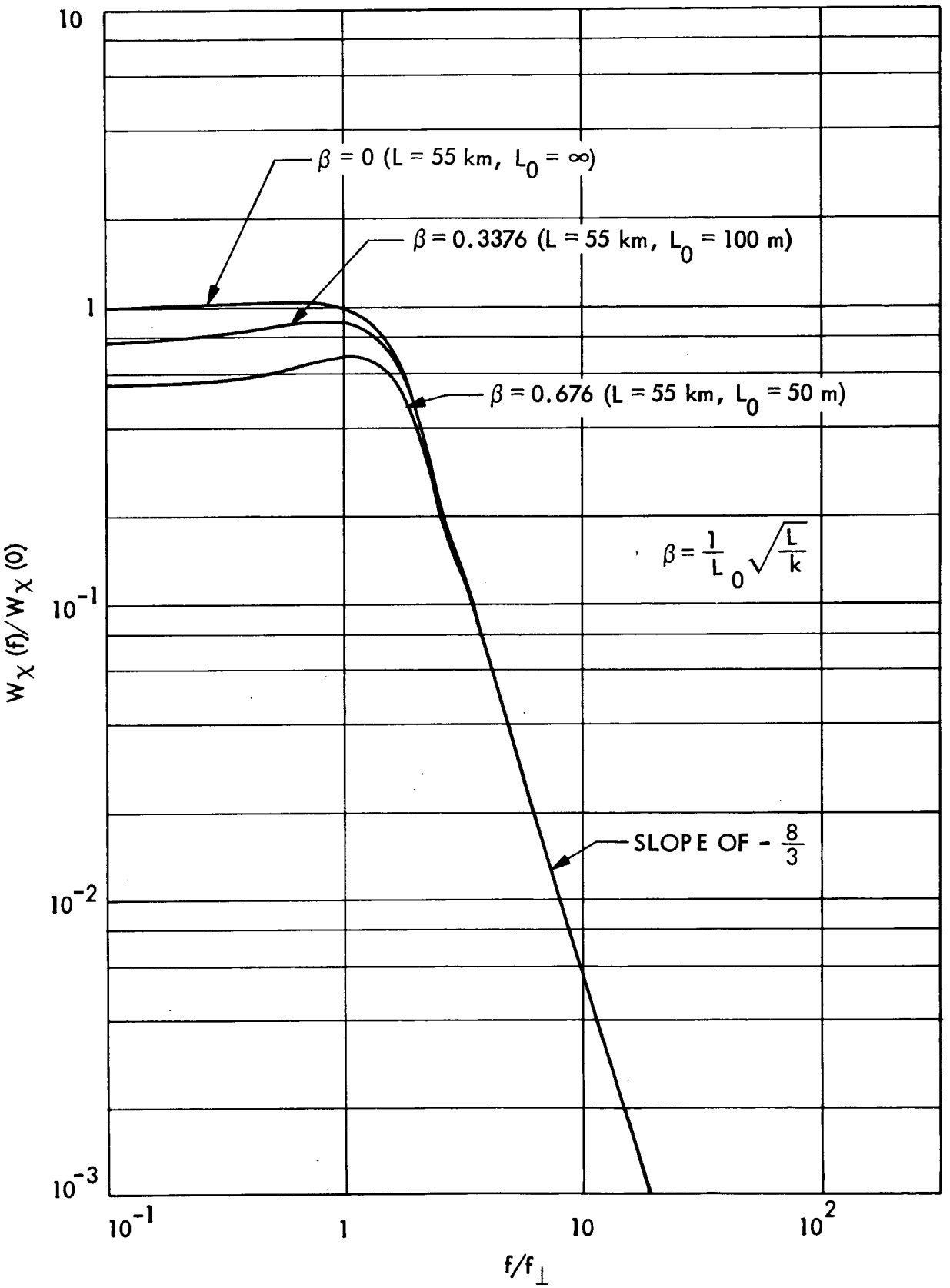

Figure 3. Power Spectra of Log-Amplitude Fluctuations

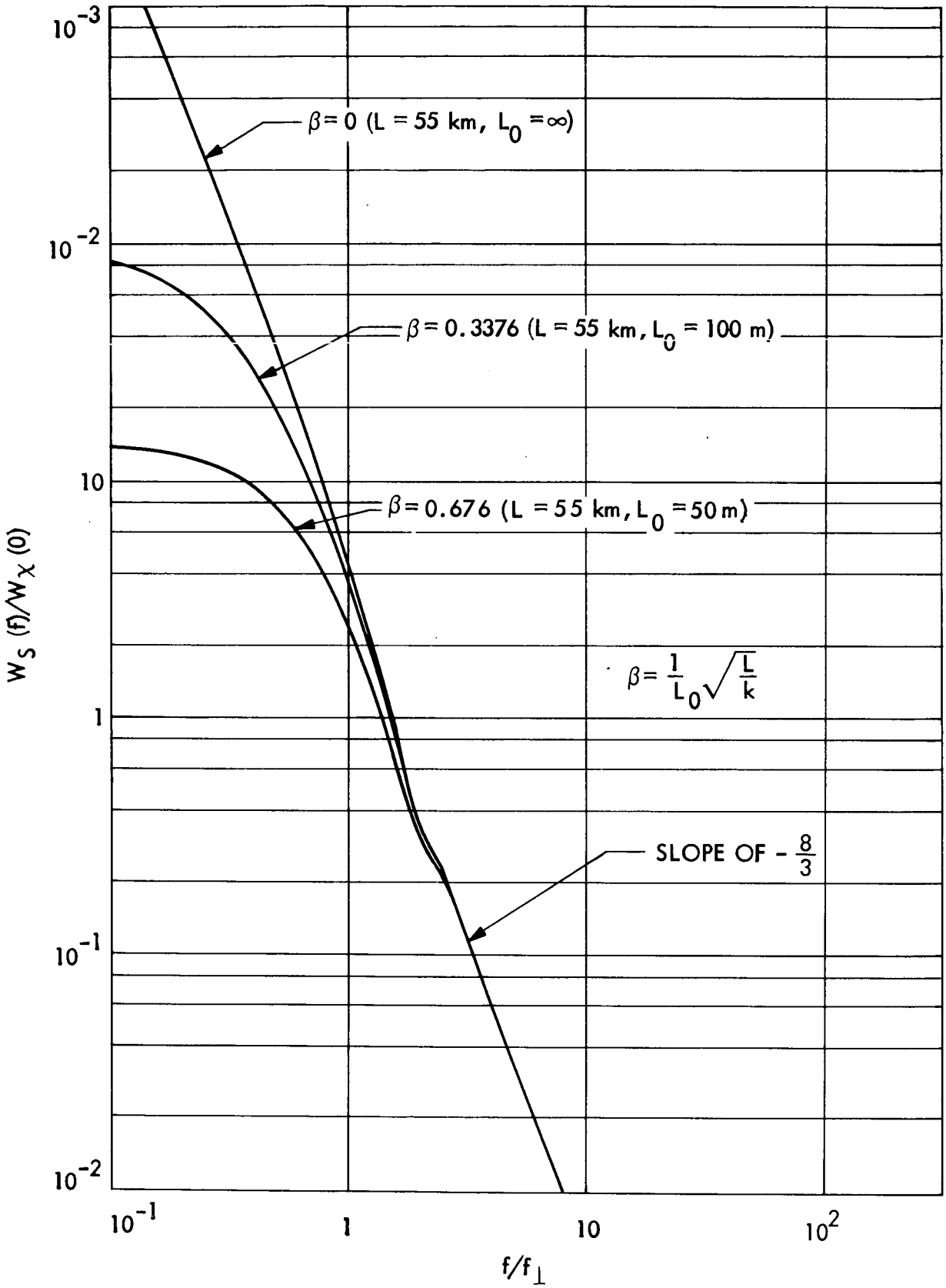

Figure 4. Power Spectra of Phase Fluctuations

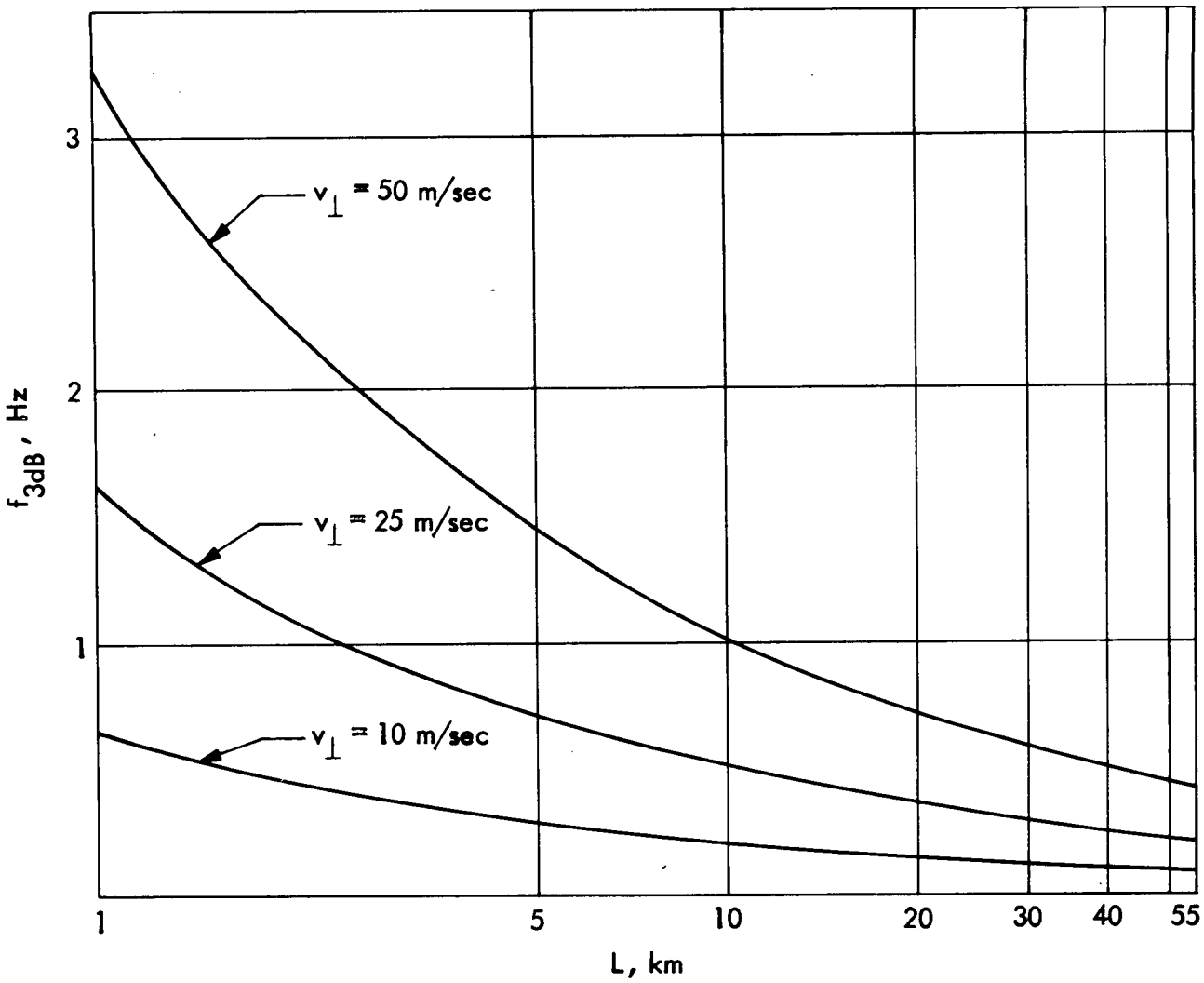

Figure 5. Variation of f_{3dB} with Respect to the Probe Penetration Distance

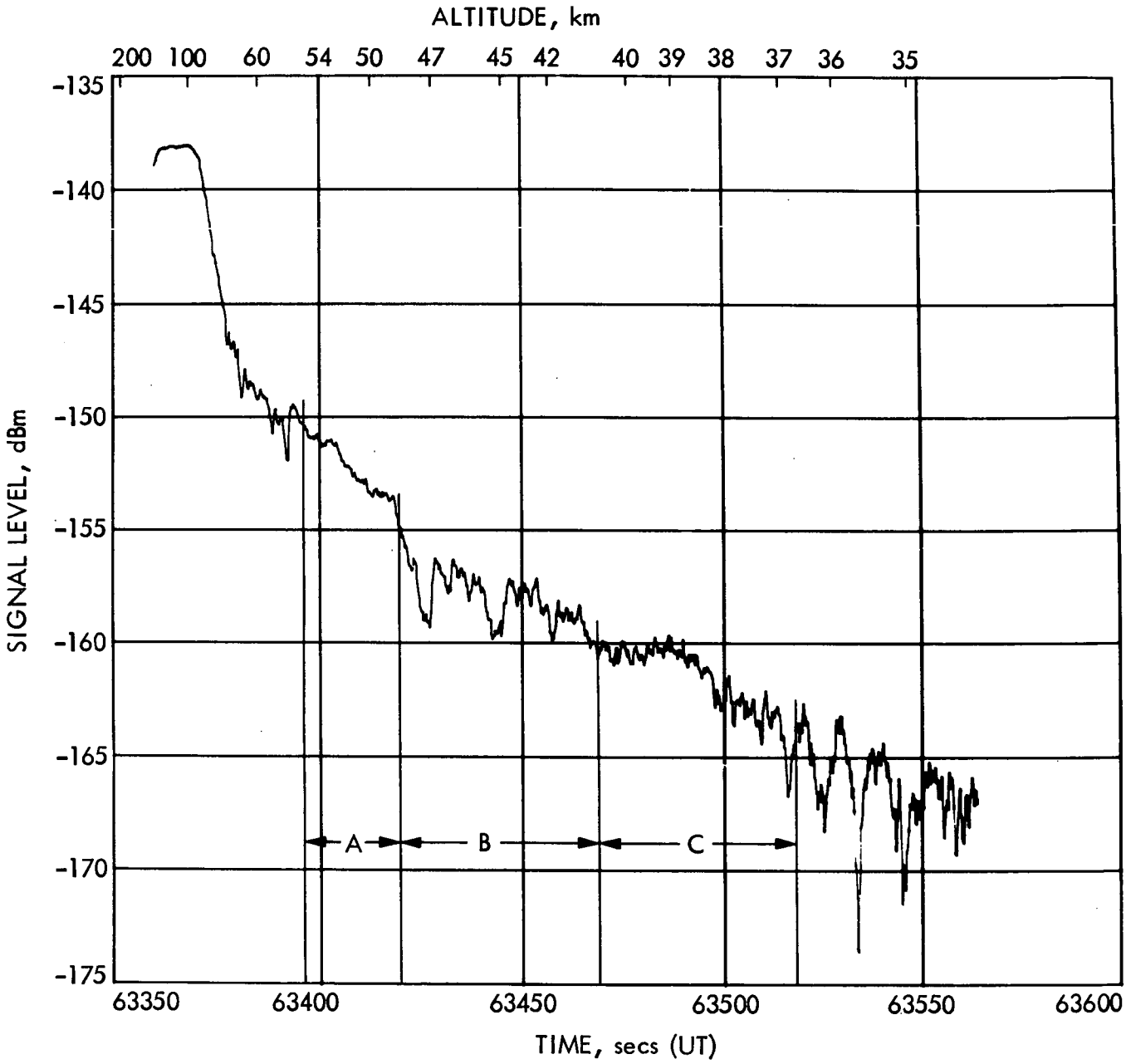

Figure 6. Signal Level vs Time in UT for Mariner 5 Venus Entrance Occultation: B_L = 10 Hz, τ_{AGC} = 1 sec, h = 0.2 sec

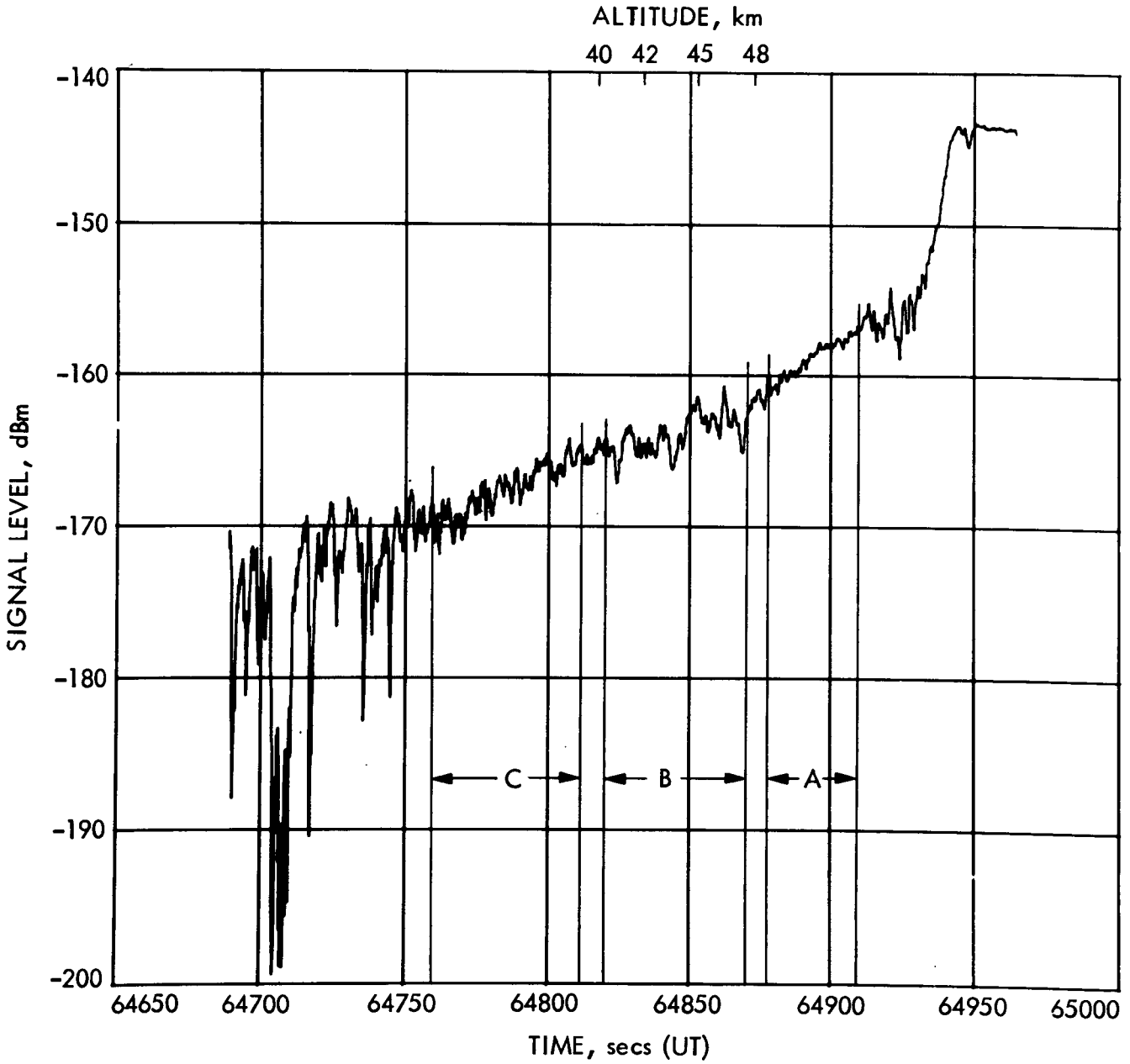

Figure 7. Signal Level vs Time in UT for Mariner 5 Venus Exit Occultation: B_L = 10 Hz, τ_{AGC} = 1 sec, h = 0.2 sec

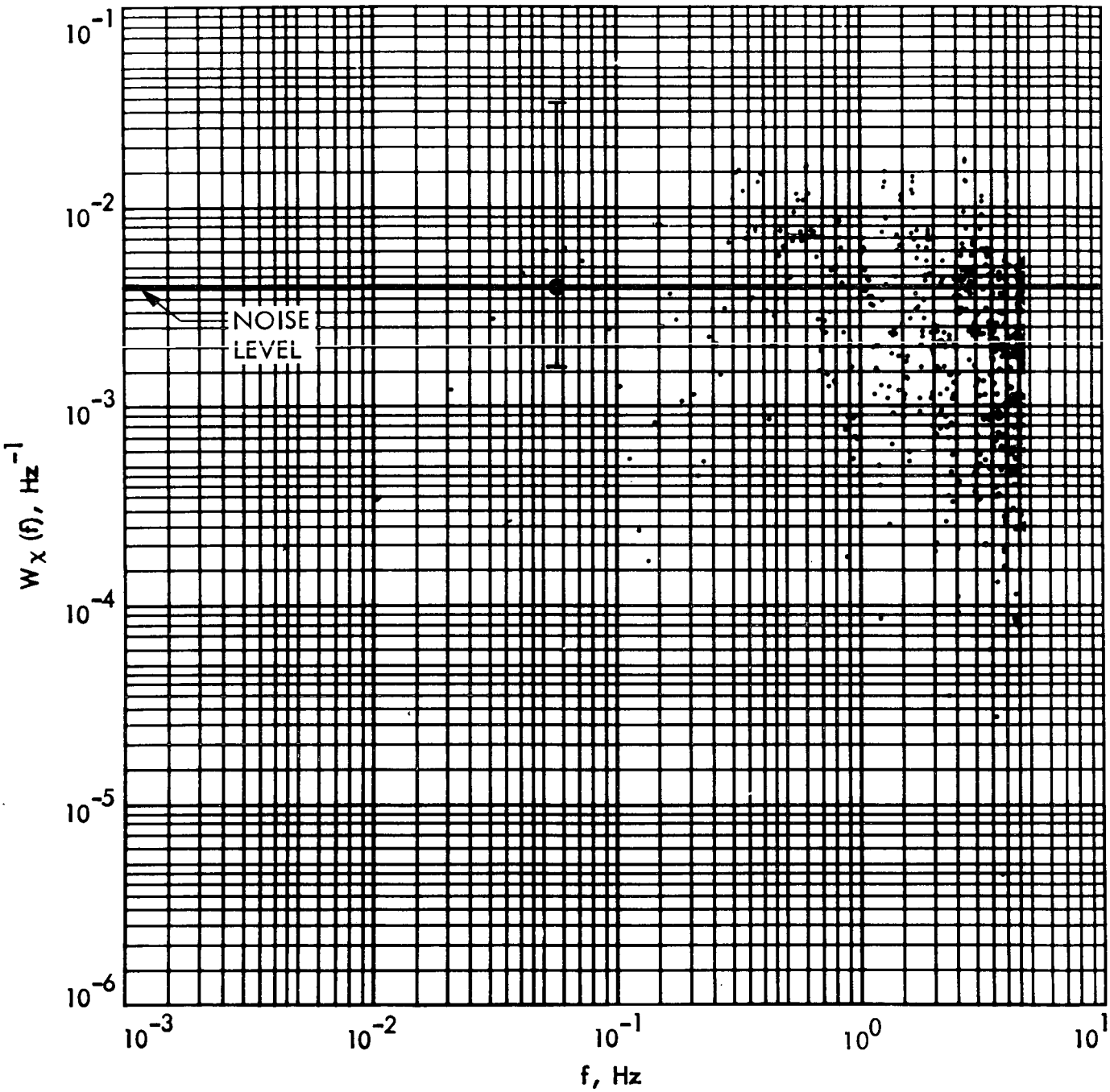

Figure 8a. Region A of Exit Occultation: B_L = 5 Hz, τ_{AGC} = 0.33 secs, h = 0.023 secs, m = 1

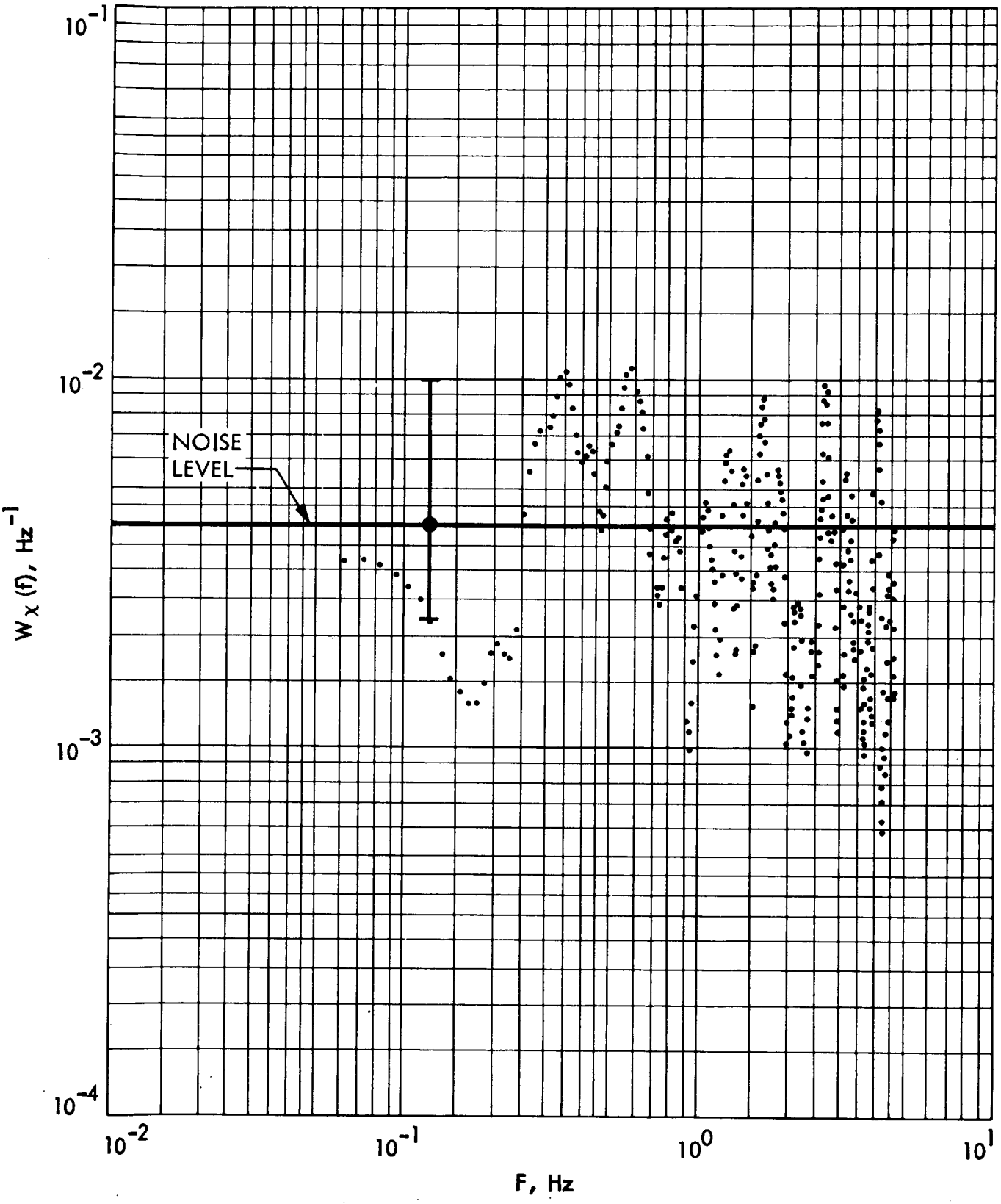

Figure 8b. Region A of Exit Occultation: B_L = 5 Hz, τ_{AGC} = 0.33 secs, h = 0.023 sec, m = 11

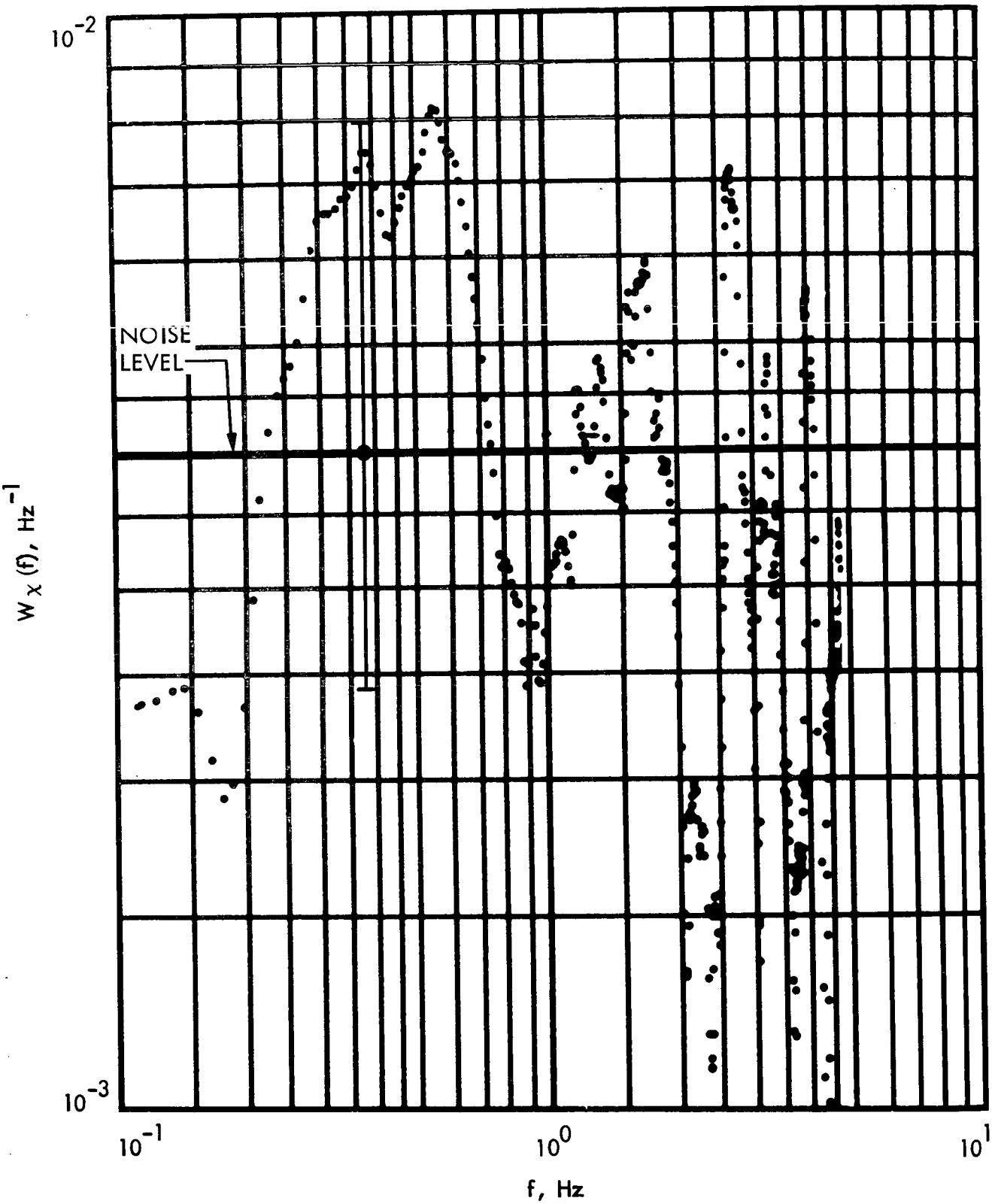

Figure 8c. Region A of Exit Occultation: B_L = 5 Hz, τ_{AGC} = 0.33 secs, h = 0.023 secs, m = 21

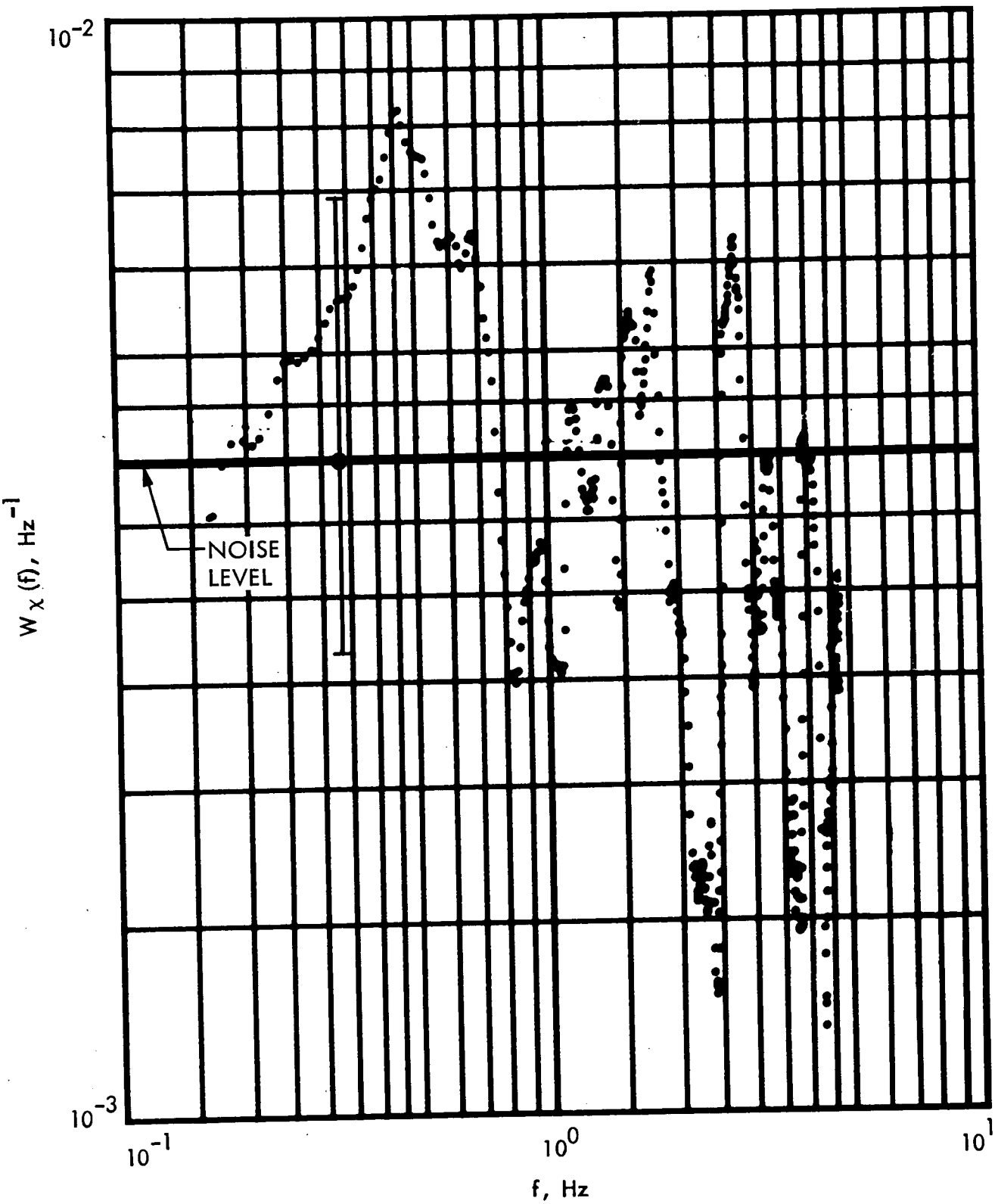

Figure 8d. Region A of Exit Occultation: B_L = 5 Hz, τ_{AGC} = 0.33 secs, h = 0.023 secs., m = 31

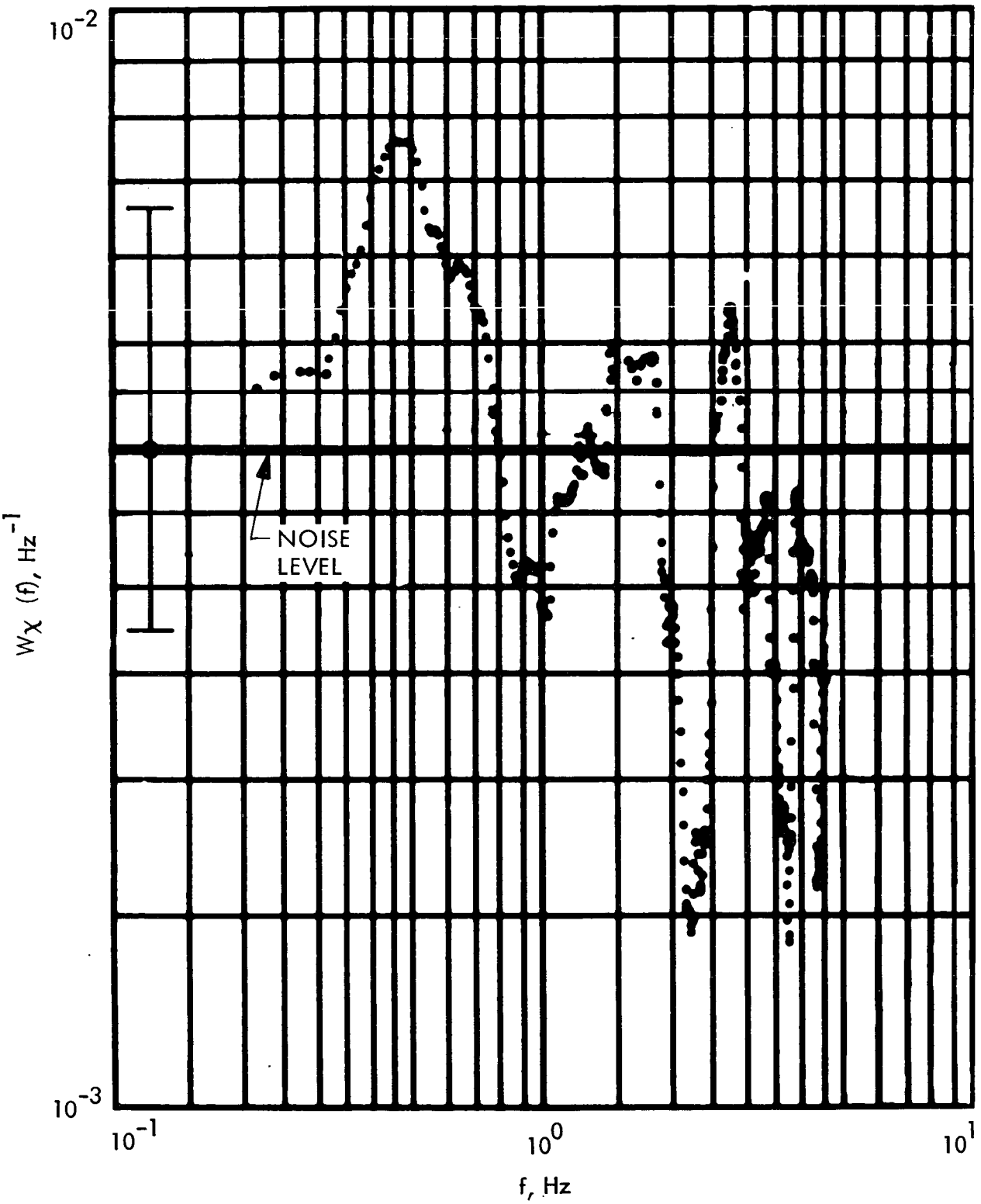

Figure 8e. Region A of Exit Occultation: B_L = 5 Hz, τ_{AGC} = 0.033 secs, h = 0.023 secs, m = 41.

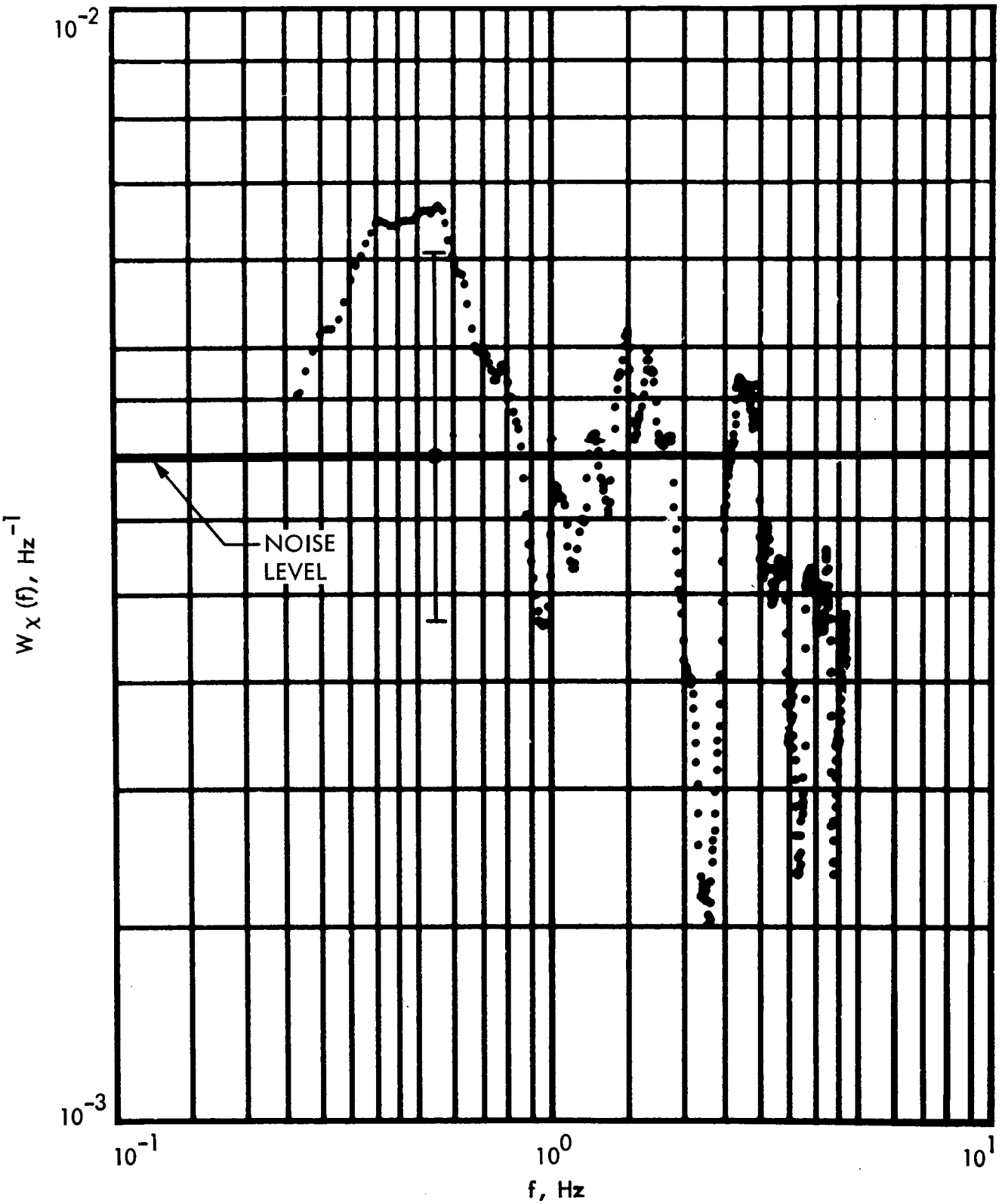

Figure 8f. Region A of Exit Occultation: B_L = 5 Hz, τ_{AGC} = 0.33 secs, h = 0.023 secs, m = 51

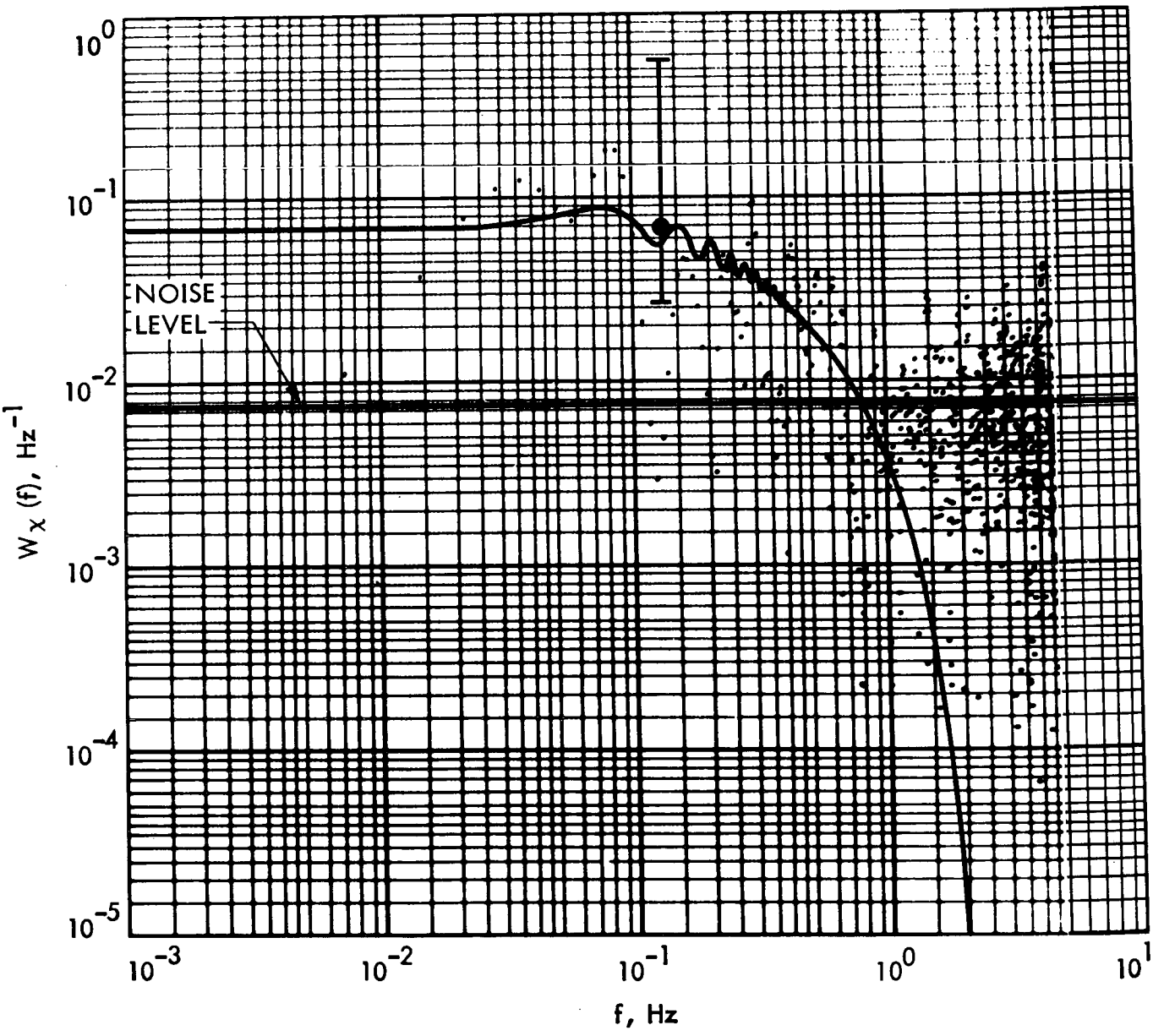

Figure 9a. Region B of Exit Occultation: B_L = 5 Hz, τ_{AGC} = 0.033 secs, h = 0.033 secs, m = 1.

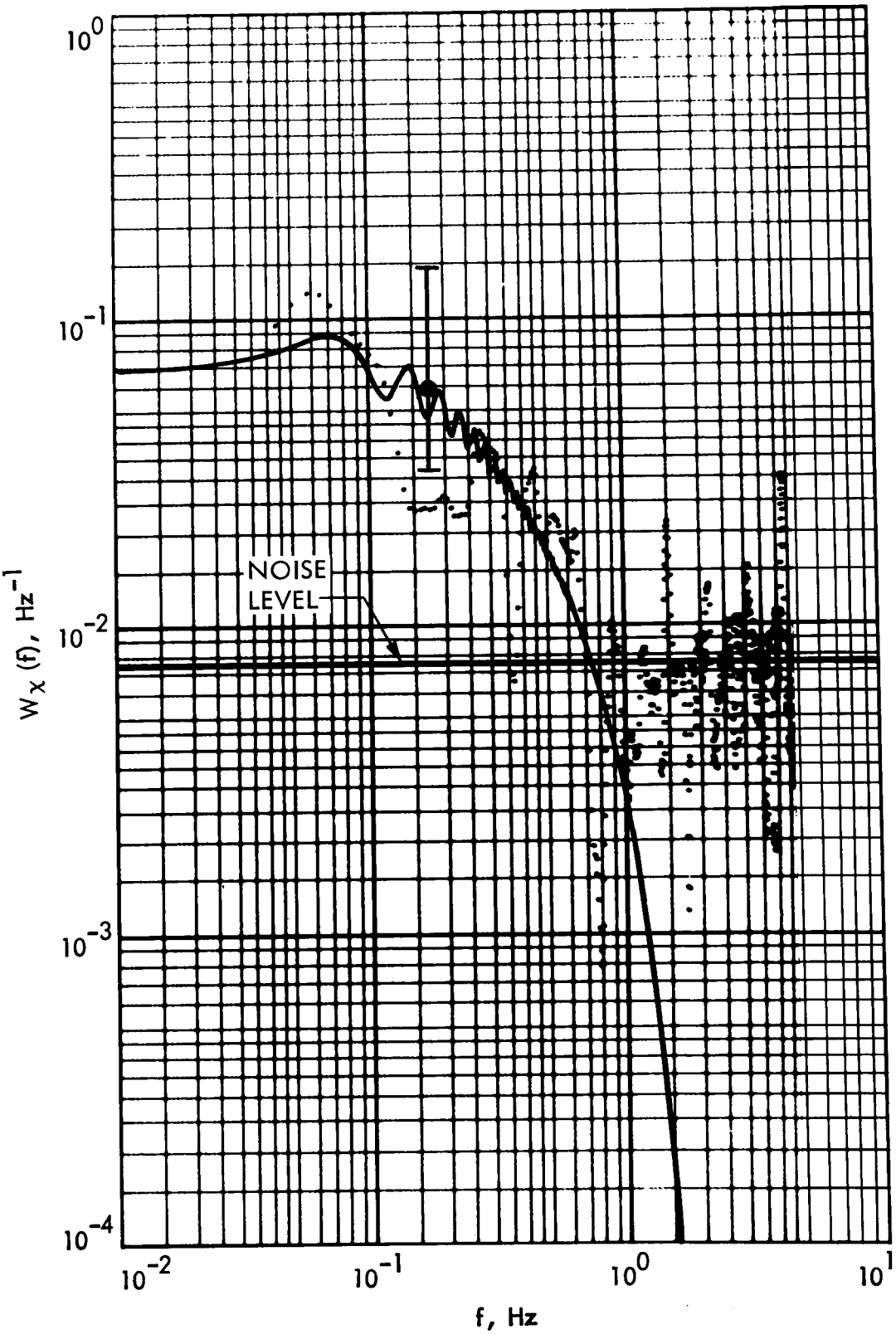

Figure 9b. Region B of Exit Occultation: B_L = 5 Hz, τ_{AGC} = 0.033 secs, h = 0.033 secs, m = 11.

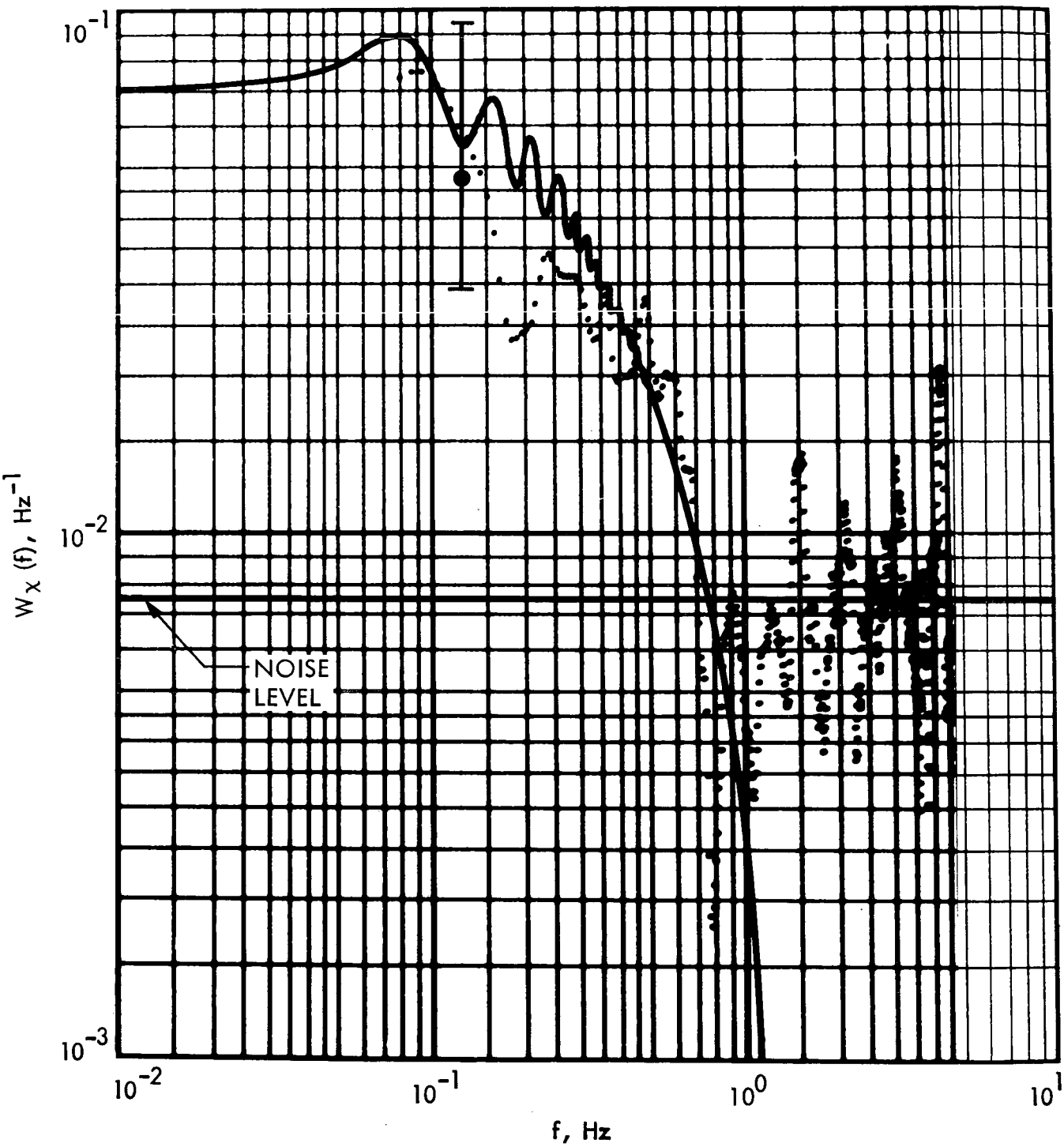

Figure 9c. Region B of Exit Occultation: B_L = 5 Hz, τ_{AGC} = 0.033 secs, h = 0.033 secs, m = 21.

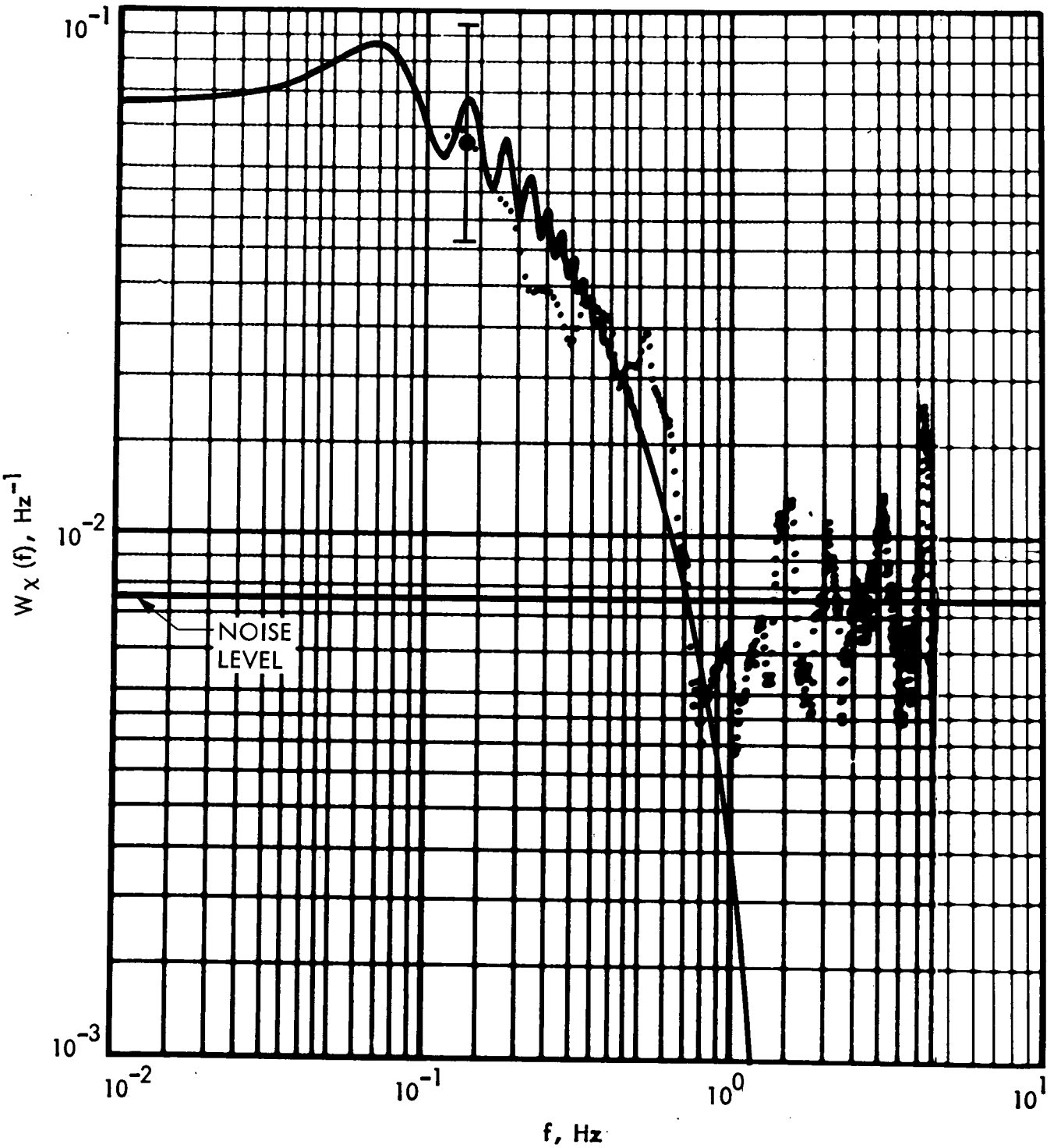

Figure 9d. Region B of Exit Occultation: B_L = 5 Hz, τ_{AGC} = 0.033 secs, h = 0.033 secs, m = 31.

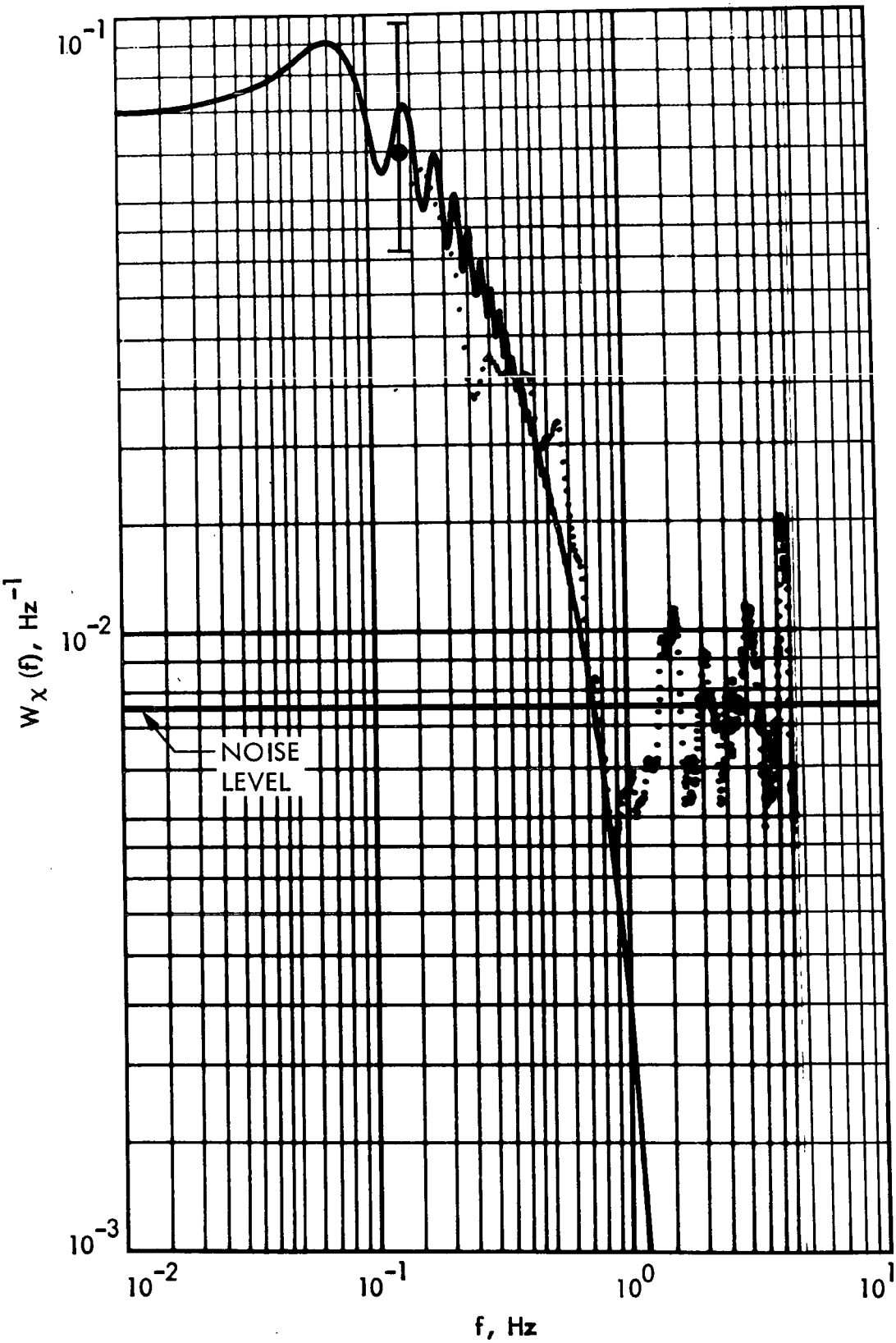

Figure 9e. Region B of Exit Occultation: B_L = 5 Hz, τ_{AGC} = 0.033 secs, h = 0.033 secs, m = 41.

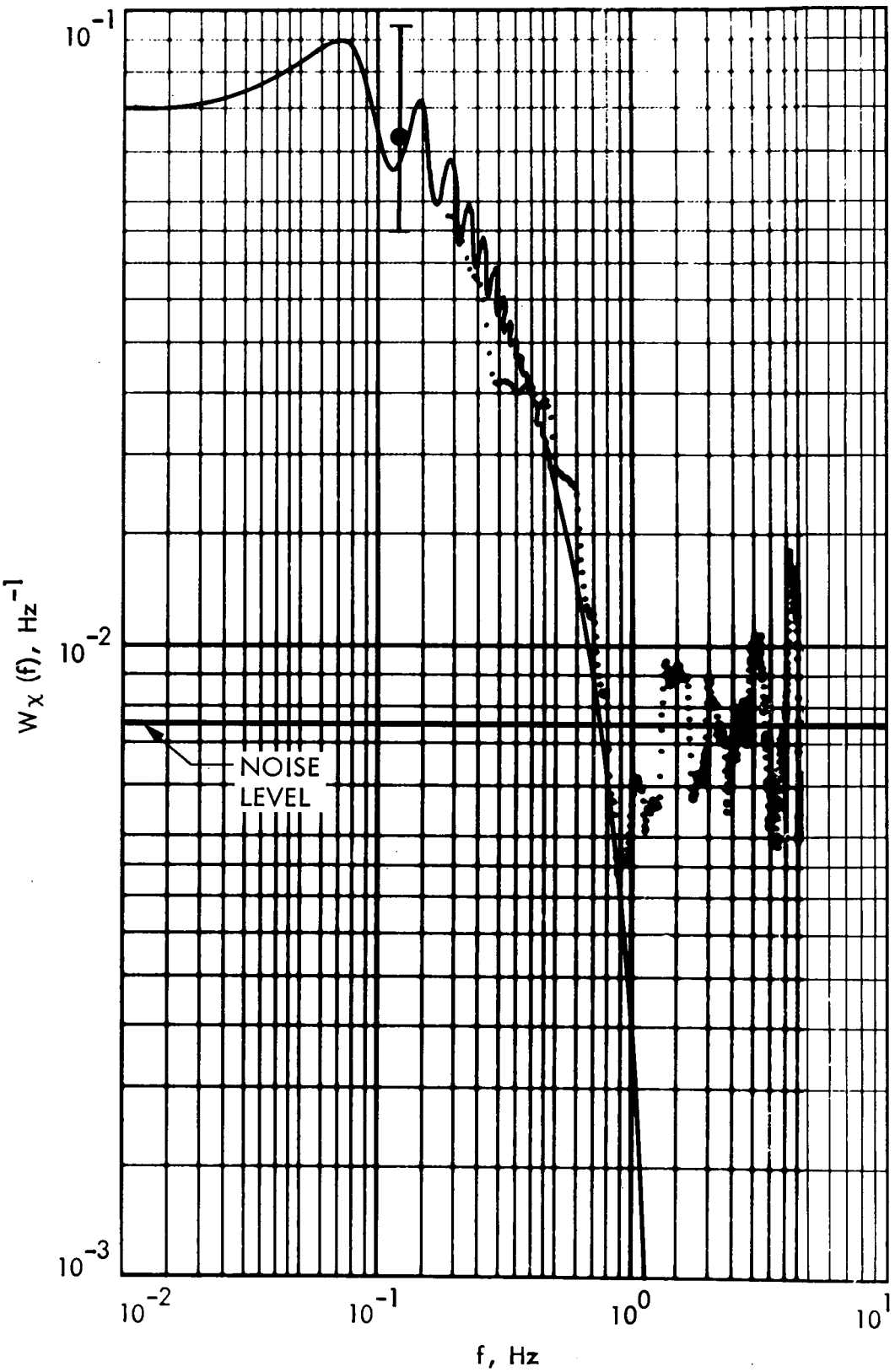

Figure 9f. Region B of Exit Occultation: B_L = 5 Hz, τ_{AGC} = 0.033 secs, h = 0.033 secs, m = 51.

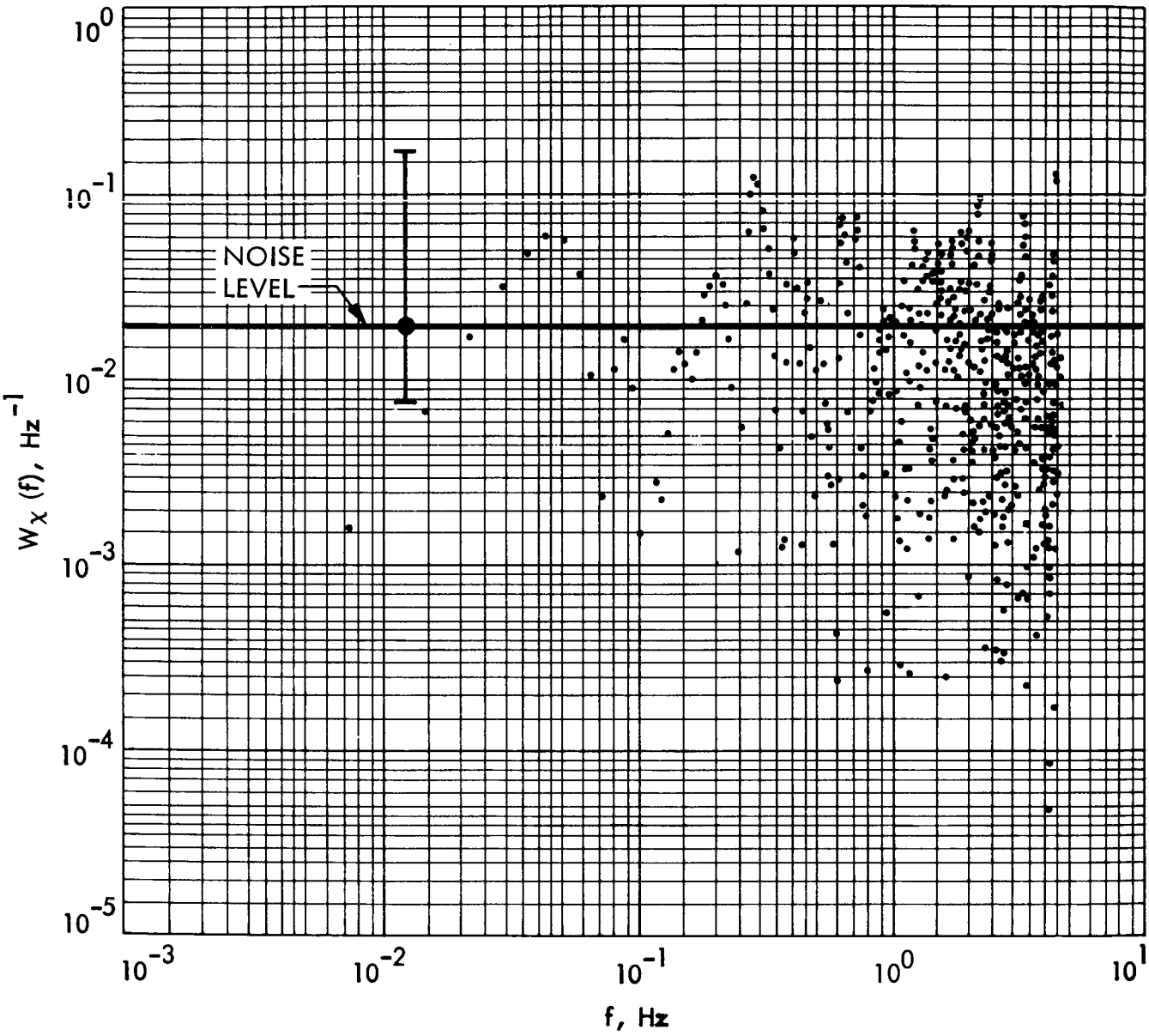

Figure 10a. Region C of Exit Occultation: B_L = 5 Hz, τ_{AGC} = 0.033 secs, h = 0.03 secs, m = 1.

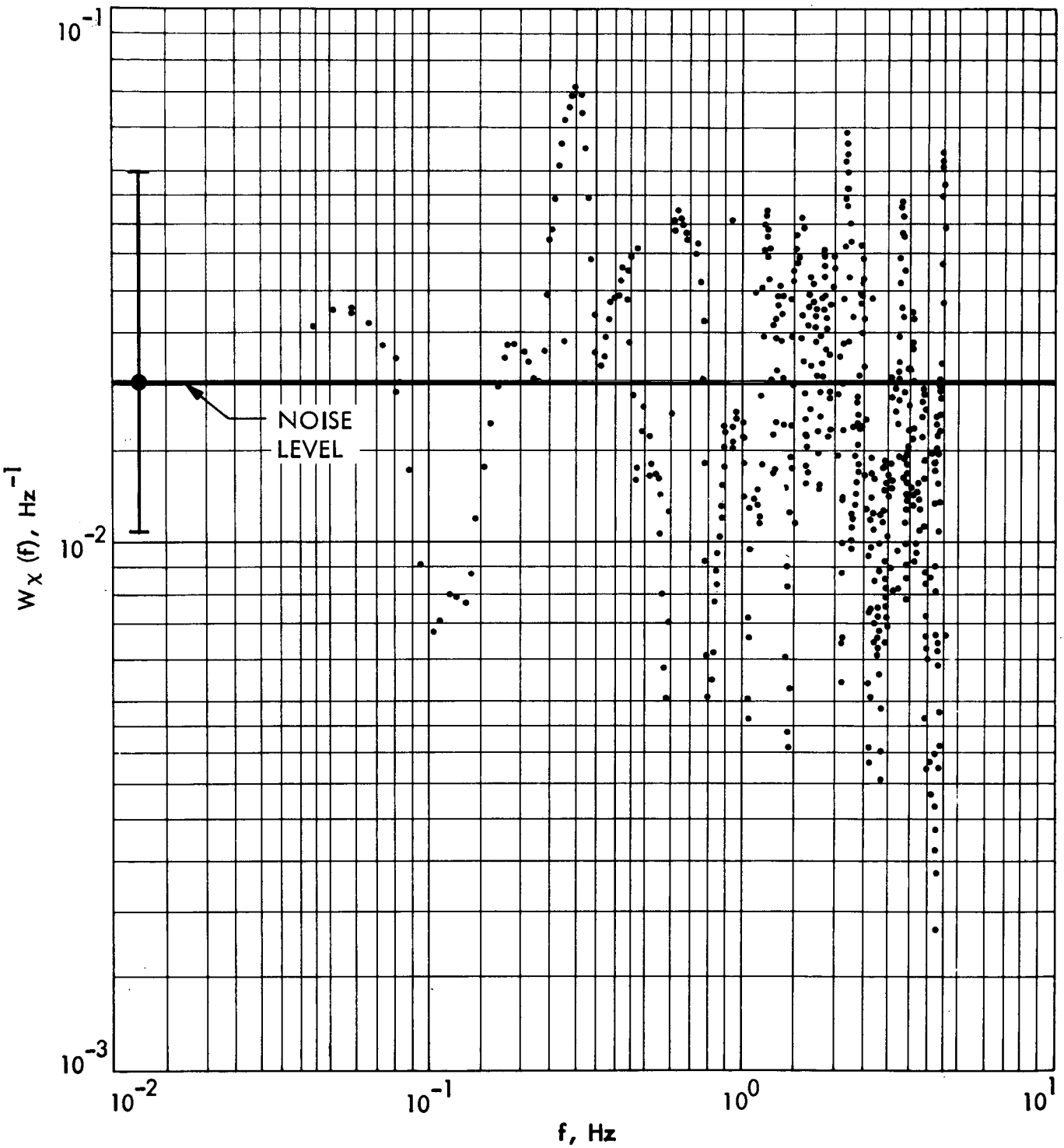

Figure 10b. Region C of Exit Occultation: B_L = 5 Hz, τ_{AGC} = 0.033 secs, h = 0.03 secs, m = 11.

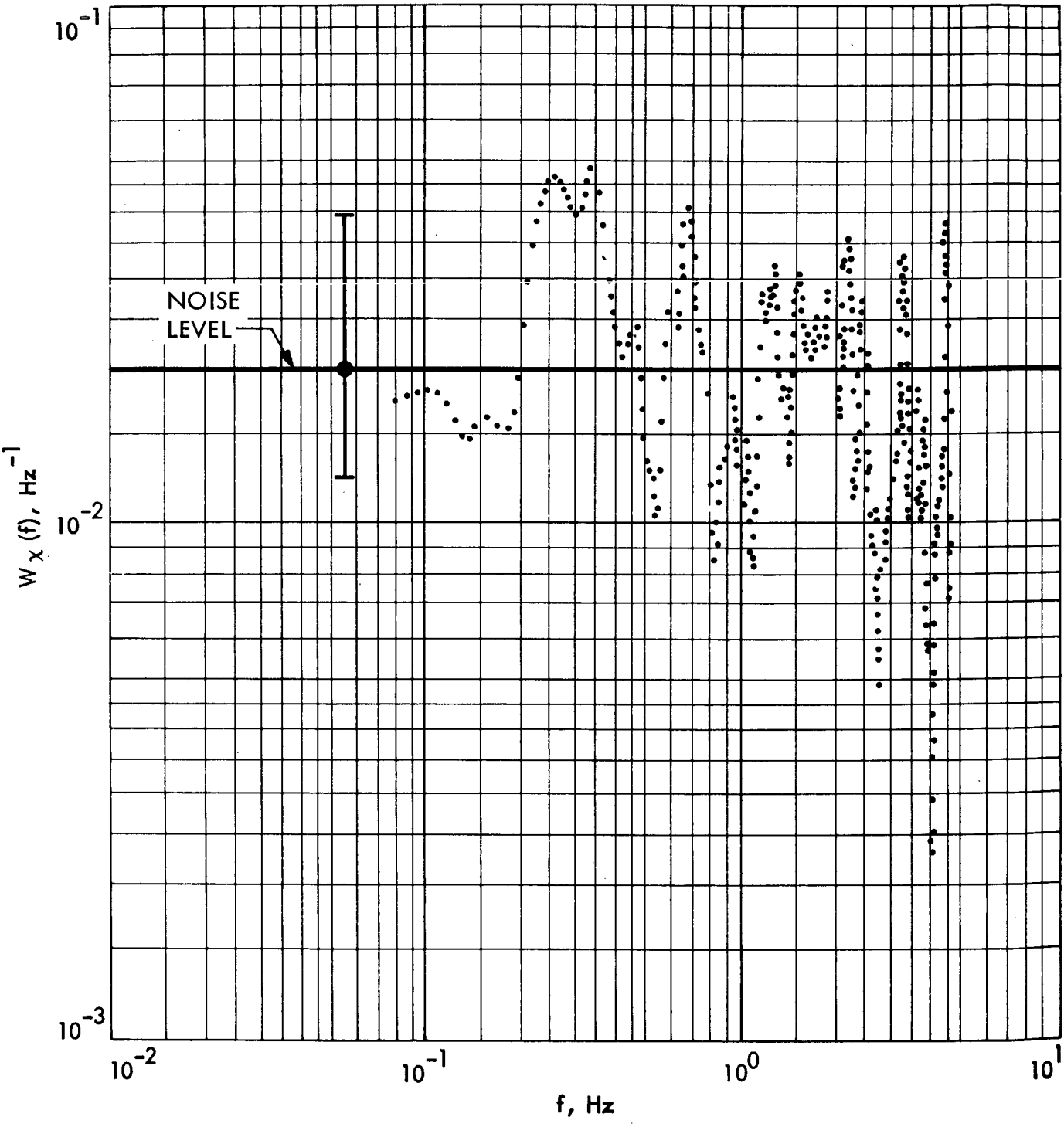

Figure 10c. Region C of Exit Occultation: B_L = 5 Hz, τ_{AGC} = 0.033 secs, h = 0.03 secs, m = 21.

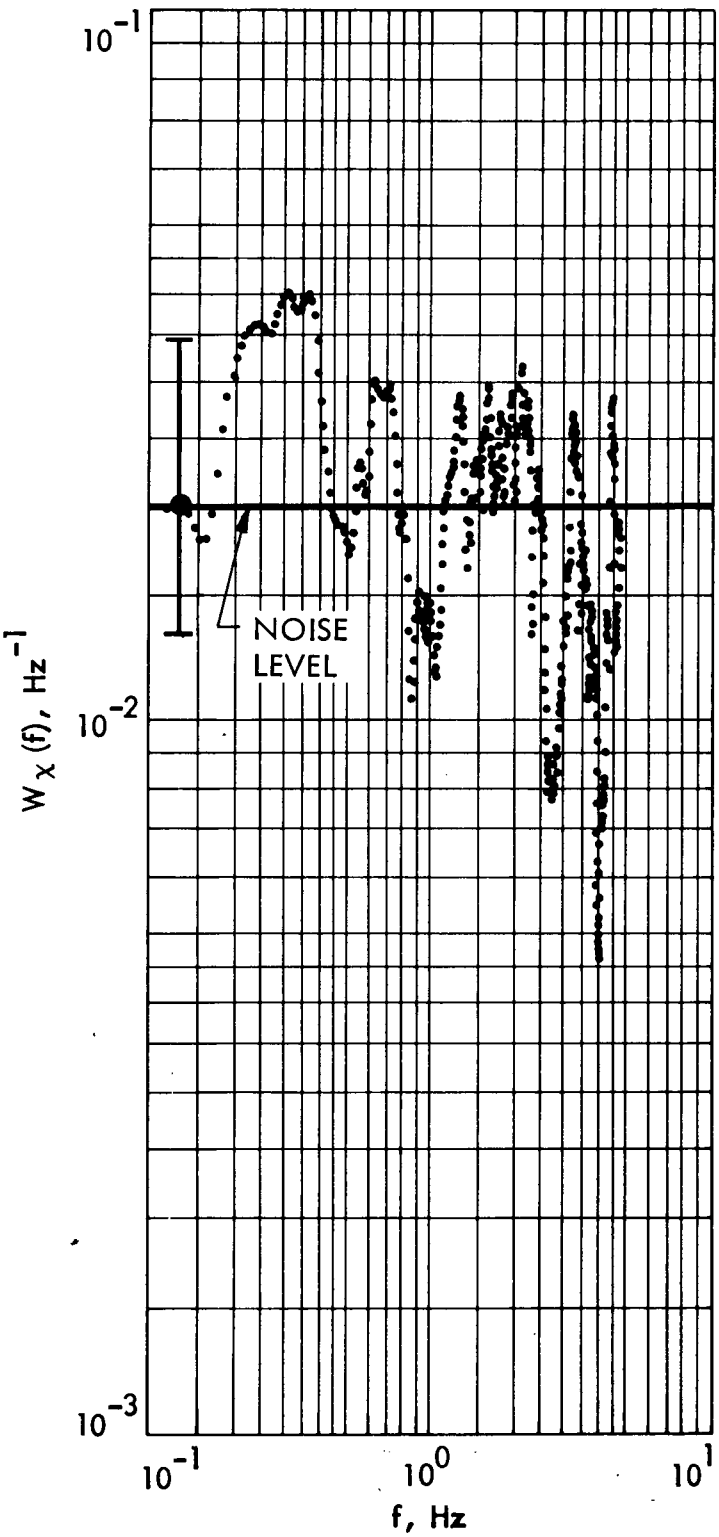

Figure 10d. Region C of Exit Occultation: B_L = 5 Hz, τ_{AGC} = 0.033 secs, h = 0.03 secs, m = 31.

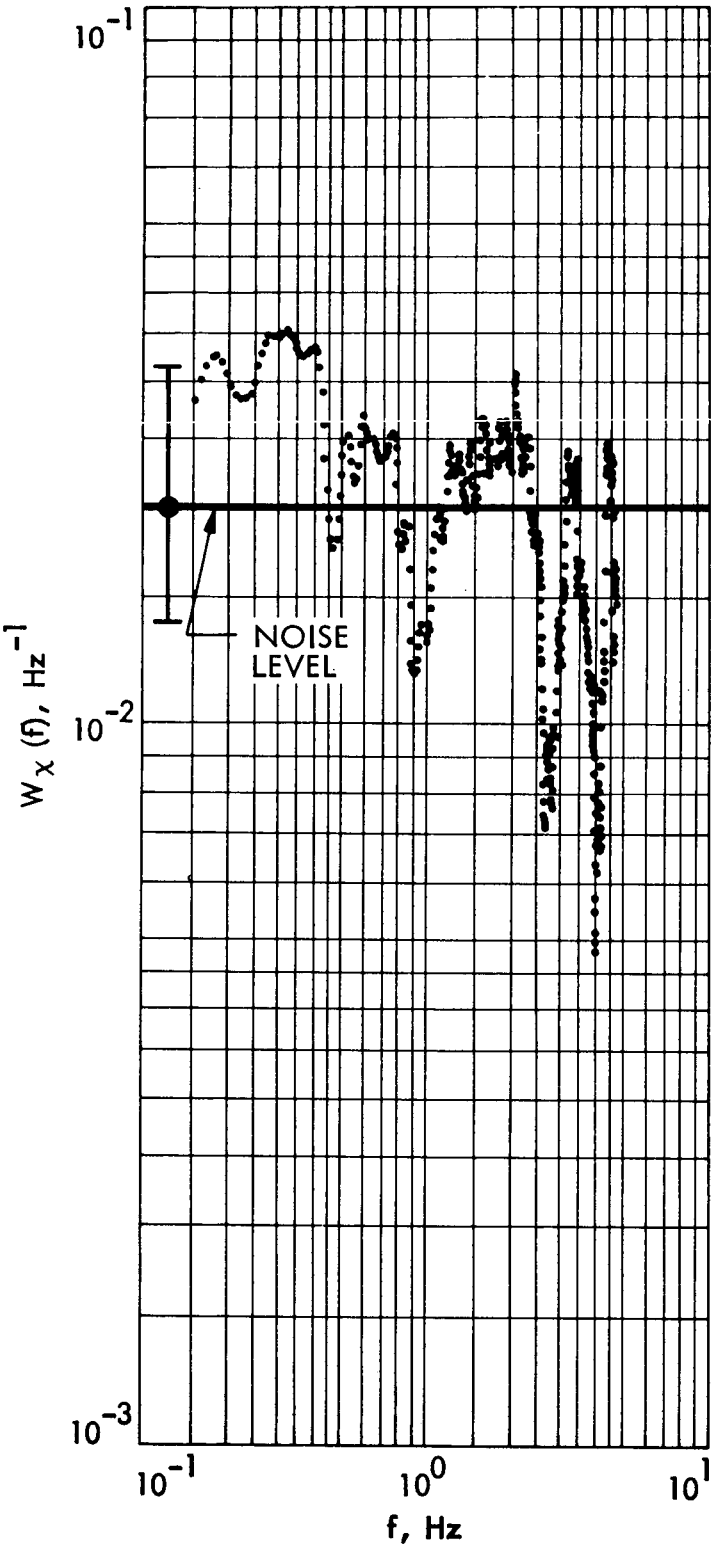

Figure 10e. Region C of Exit Occultation: B_L = 5 Hz, τ_{AGC} = 0.033 secs, h = 0.03 secs, m = 41.

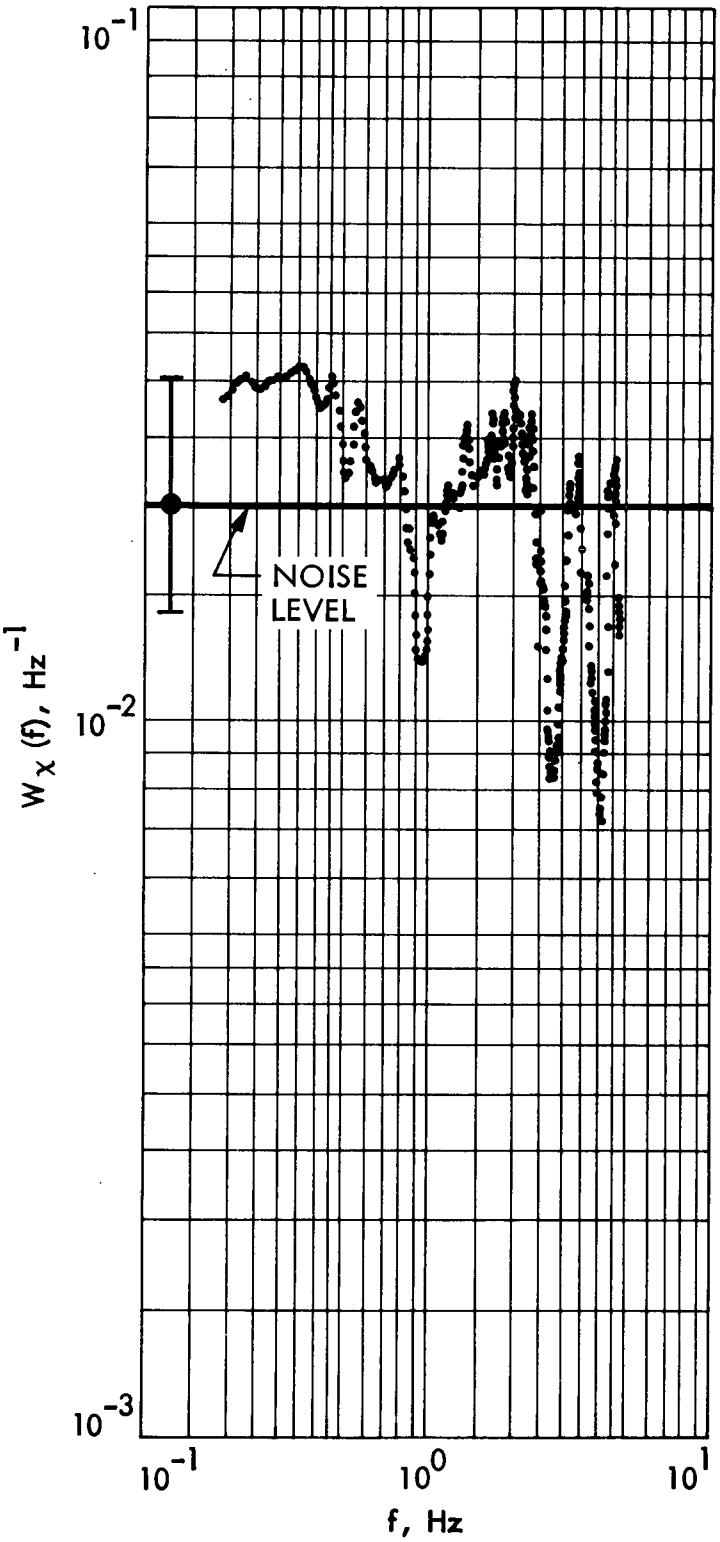

Figure 10f. Region C of Exit Occultation: B_L = 5 Hz, τ_{AGC} = 0.033 secs, h = 0.03 secs, m = 51.

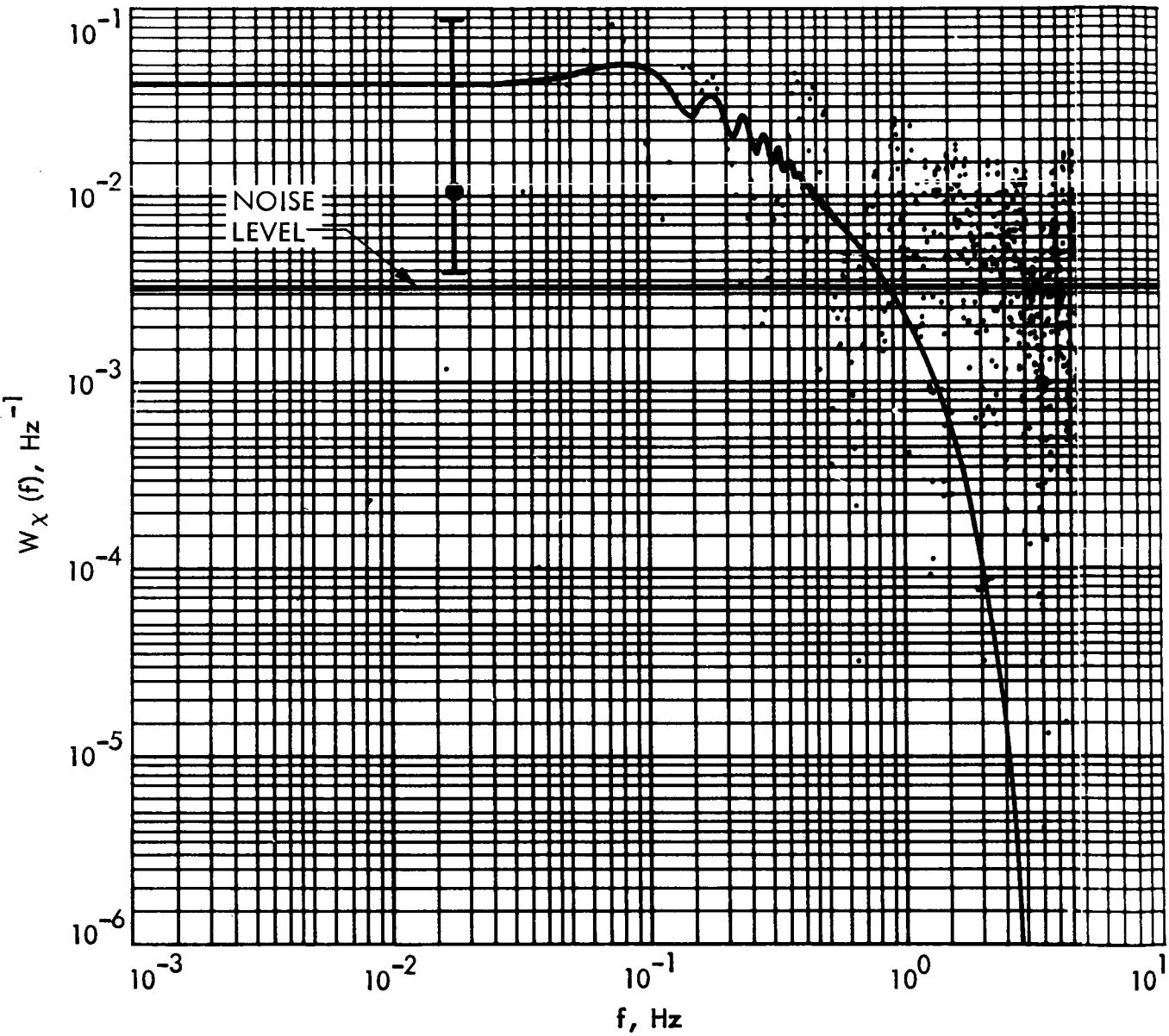

Figure 11a. Region B of Entrance Occultation: B_L = 5 Hz, τ_{AGC} = 0.033 secs, h = 0.03 secs, m = 1.

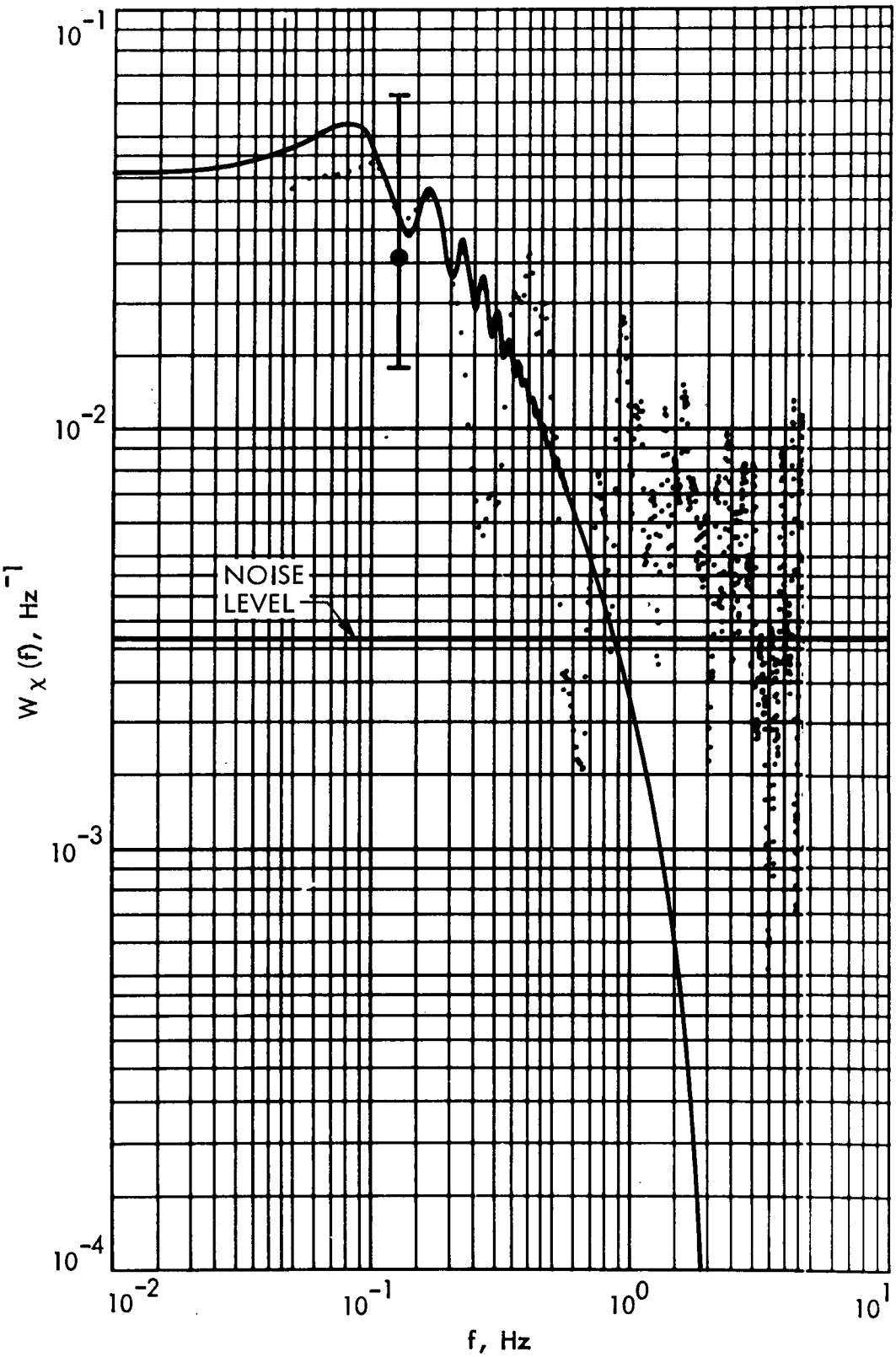

Figure 11b. Region B of Entrance Occultation: B_L = 5 Hz, τ_{AGC} = 0.033 secs, h = 0.03 secs, m = 11.

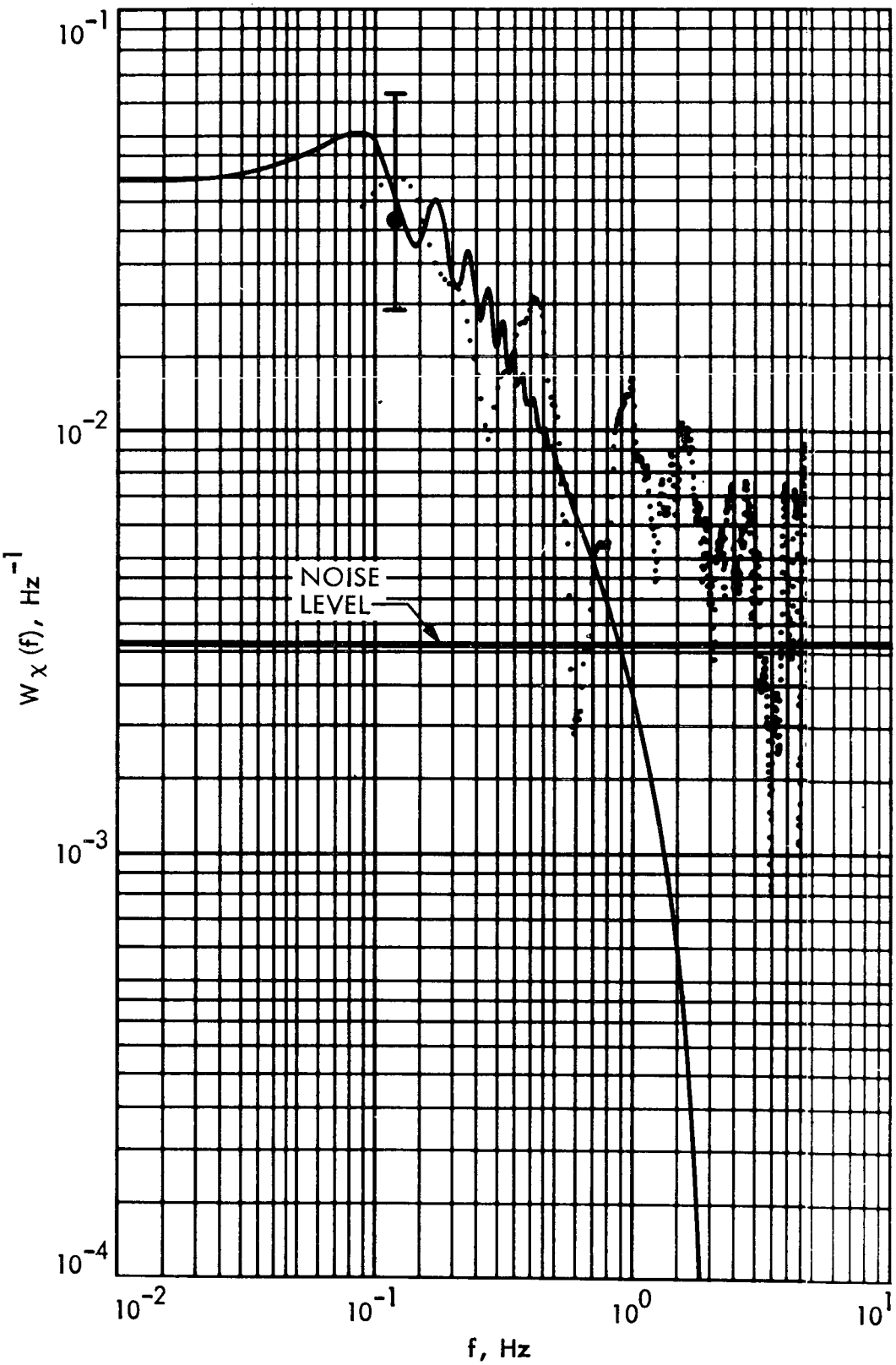

Figure 11c. Region B of Entrance Occultation: B_L = 5 Hz, τ_{AGC} = 0.033 secs, h = 0.03 secs, m = 21.

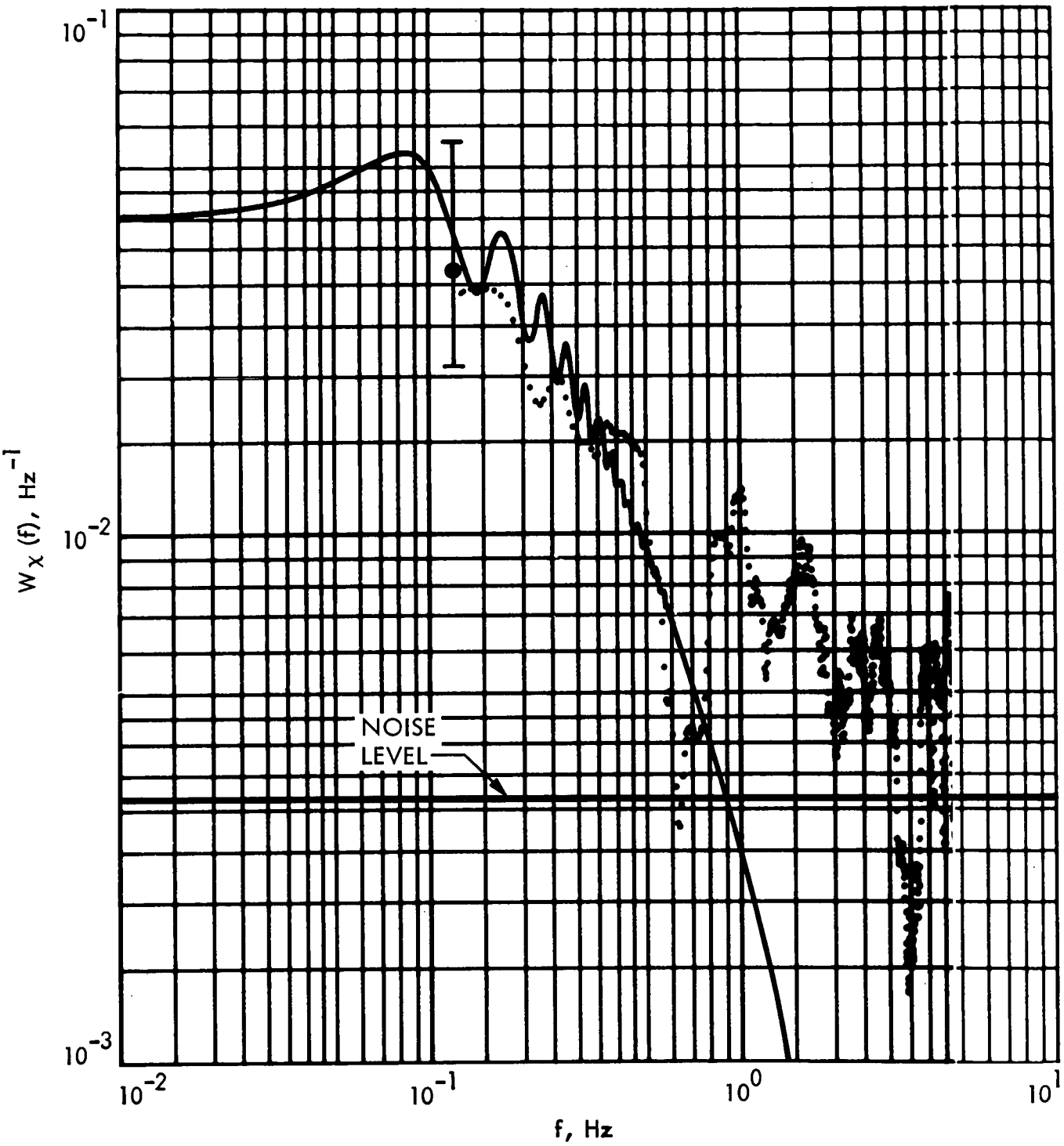

Figure 11d. Region B of Entrance Occultation: B_L = 5 Hz, τ_{AGC} = 0.033 secs, h = 0 03 secs, m = 31.

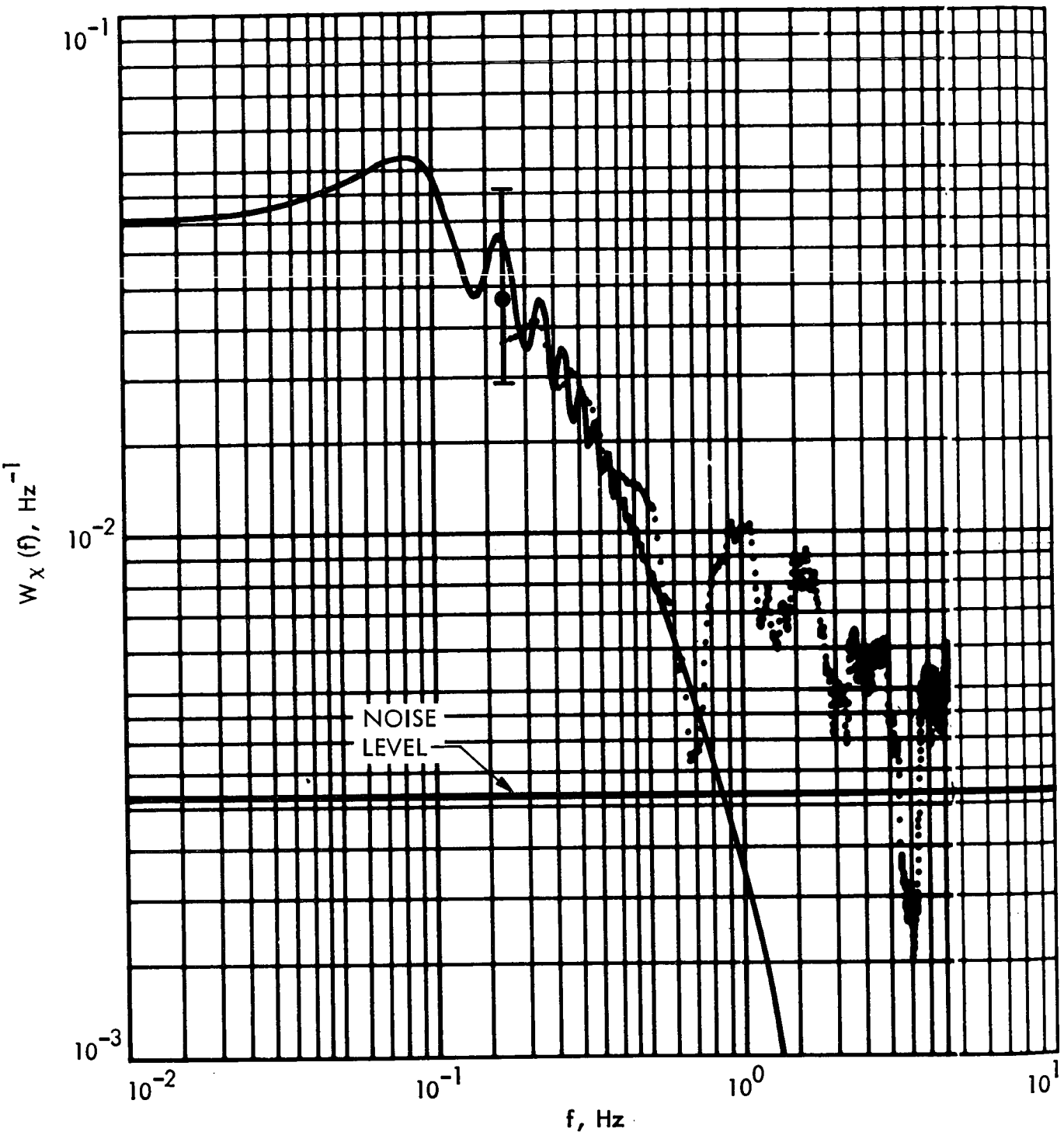

Figure 11e. Region B of Entrance Occultation: B_L = 5 Hz, τ_{AGC} = 0.033 secs, h = 0.03 secs, m = 41.

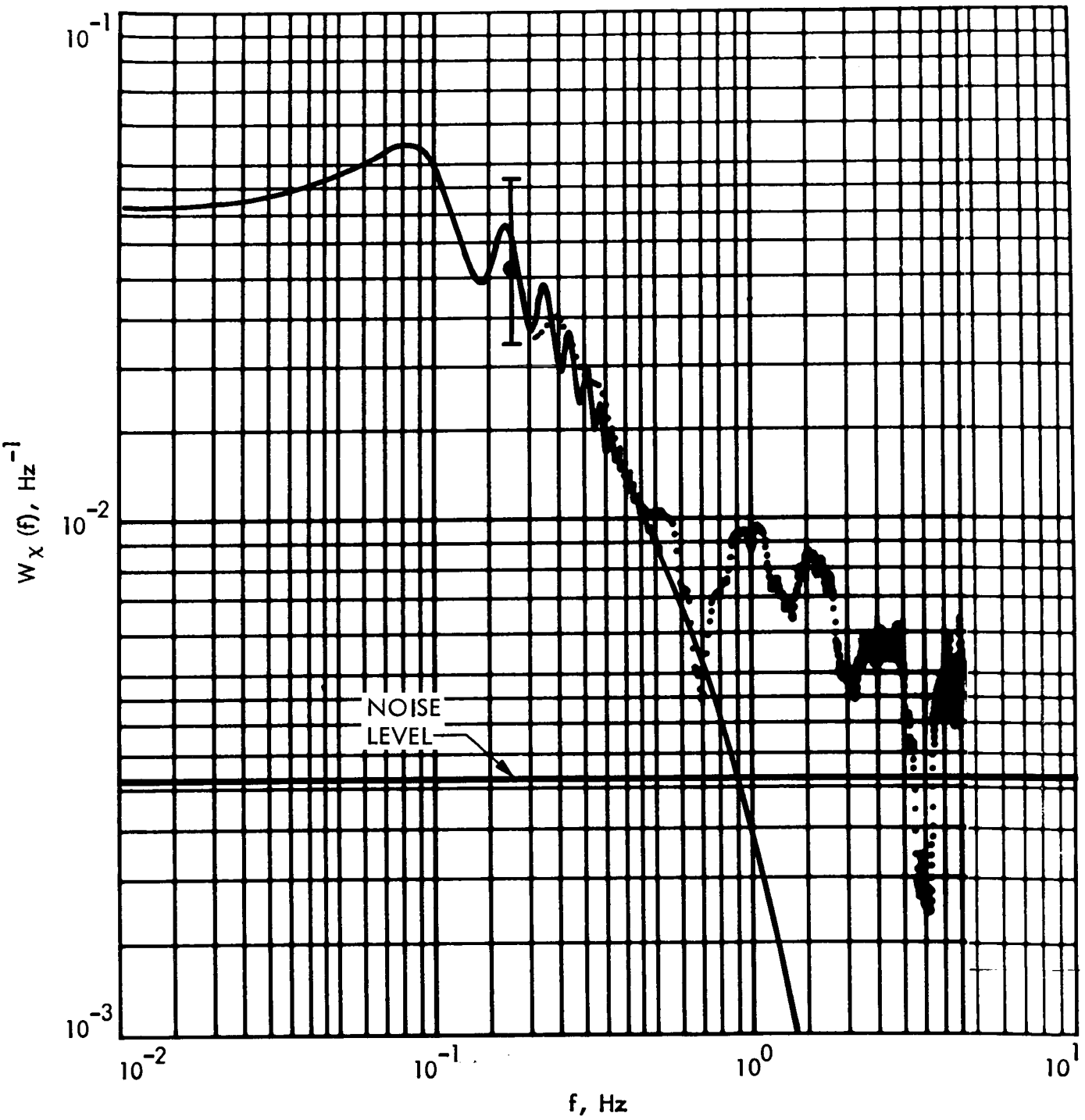

Figure 11f. Region B of Entrance Occultation: B_L = 5 Hz, τ_{AGC} = 0.033 secs, h = 0.03 secs, m = 51.

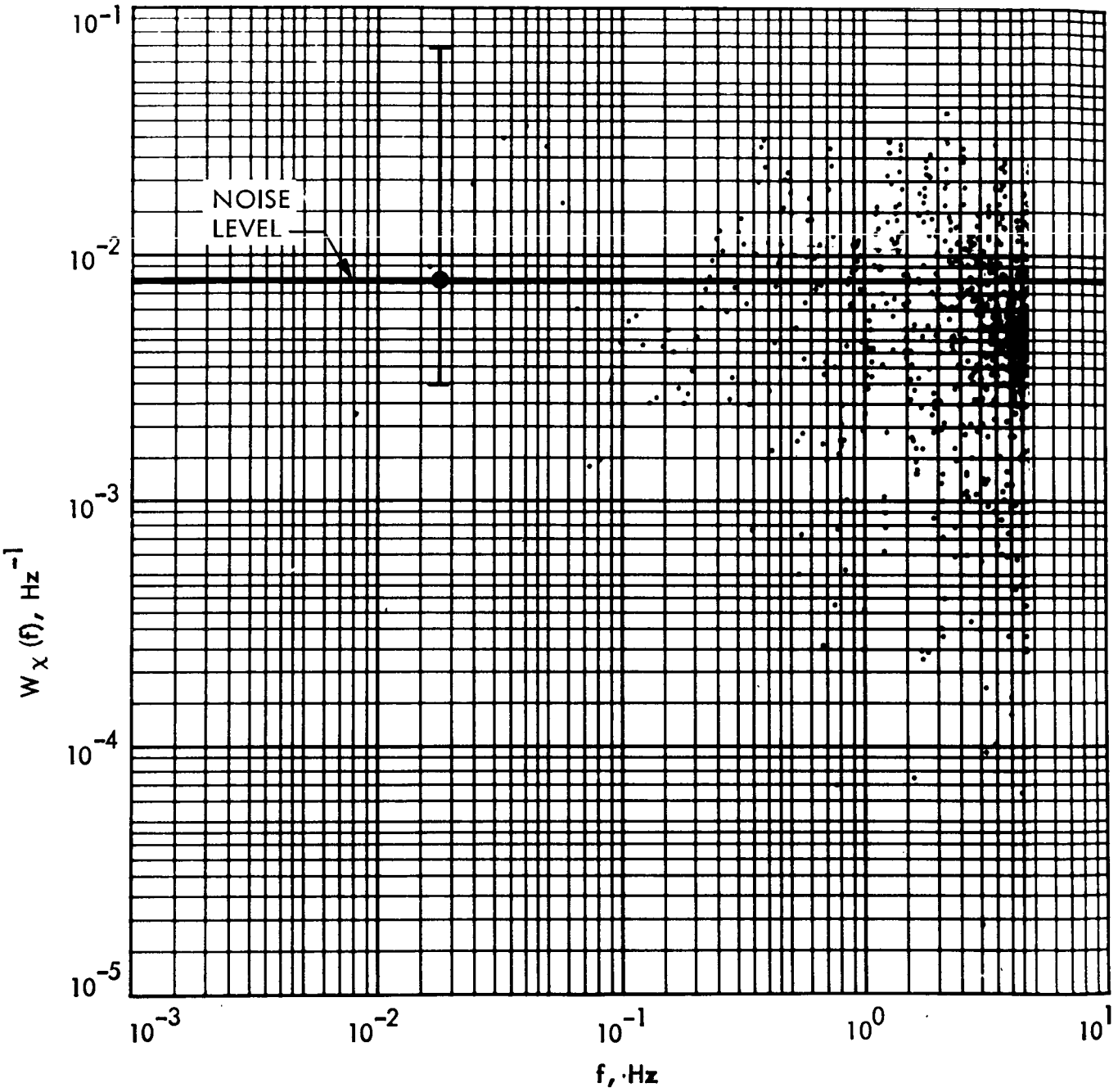

Figure 12a. Region C of Entrance Occultation: B_L = 5 Hz, τ_{AGC} = 0.033 secs, h = 0.03 secs, m = 1.

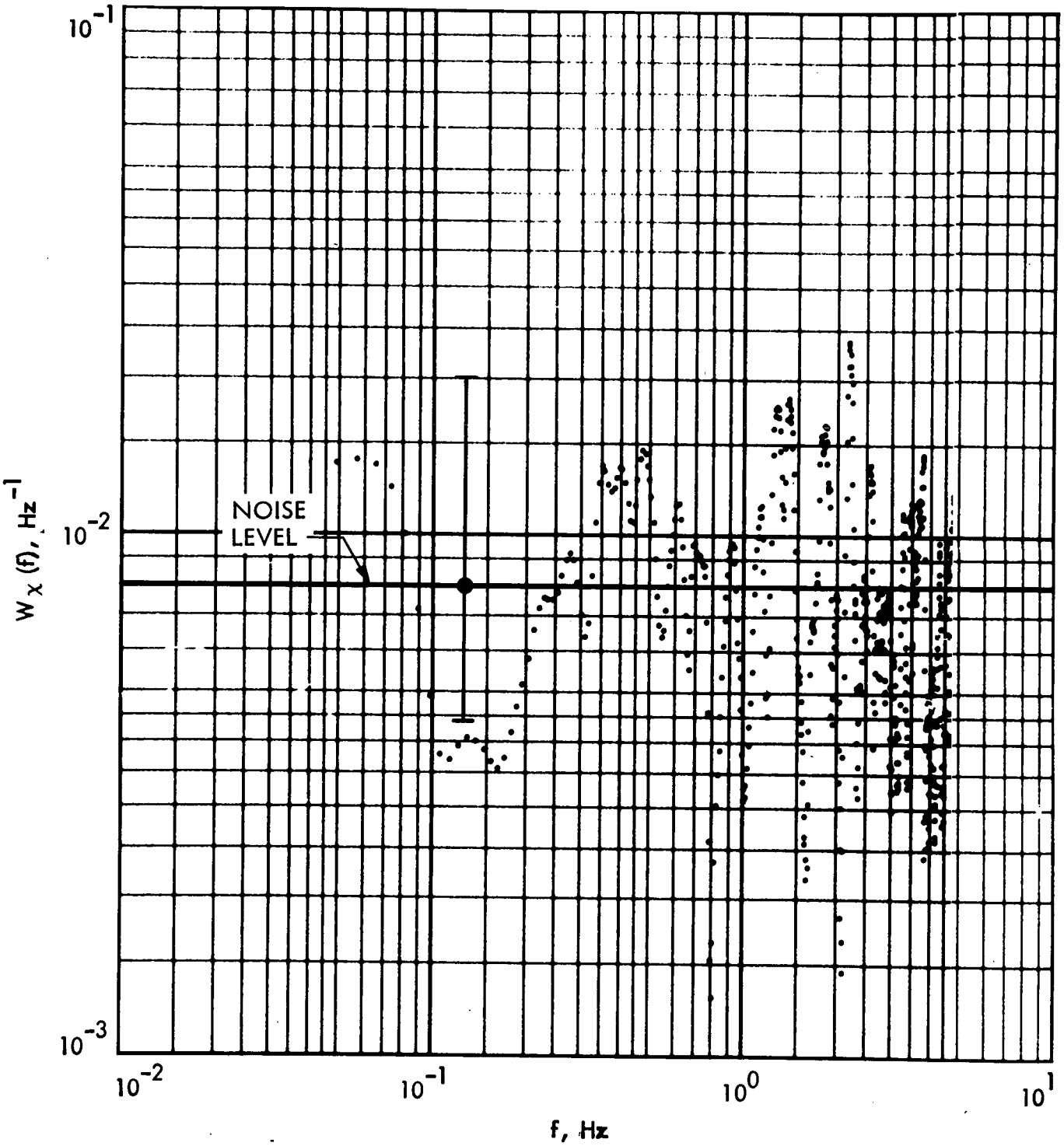

Figure 12b. Region C of Entrance Occultation: B_L = 5 Hz, τ_{AGC} = 0.033 secs, h = 0.03 secs, m = 11.

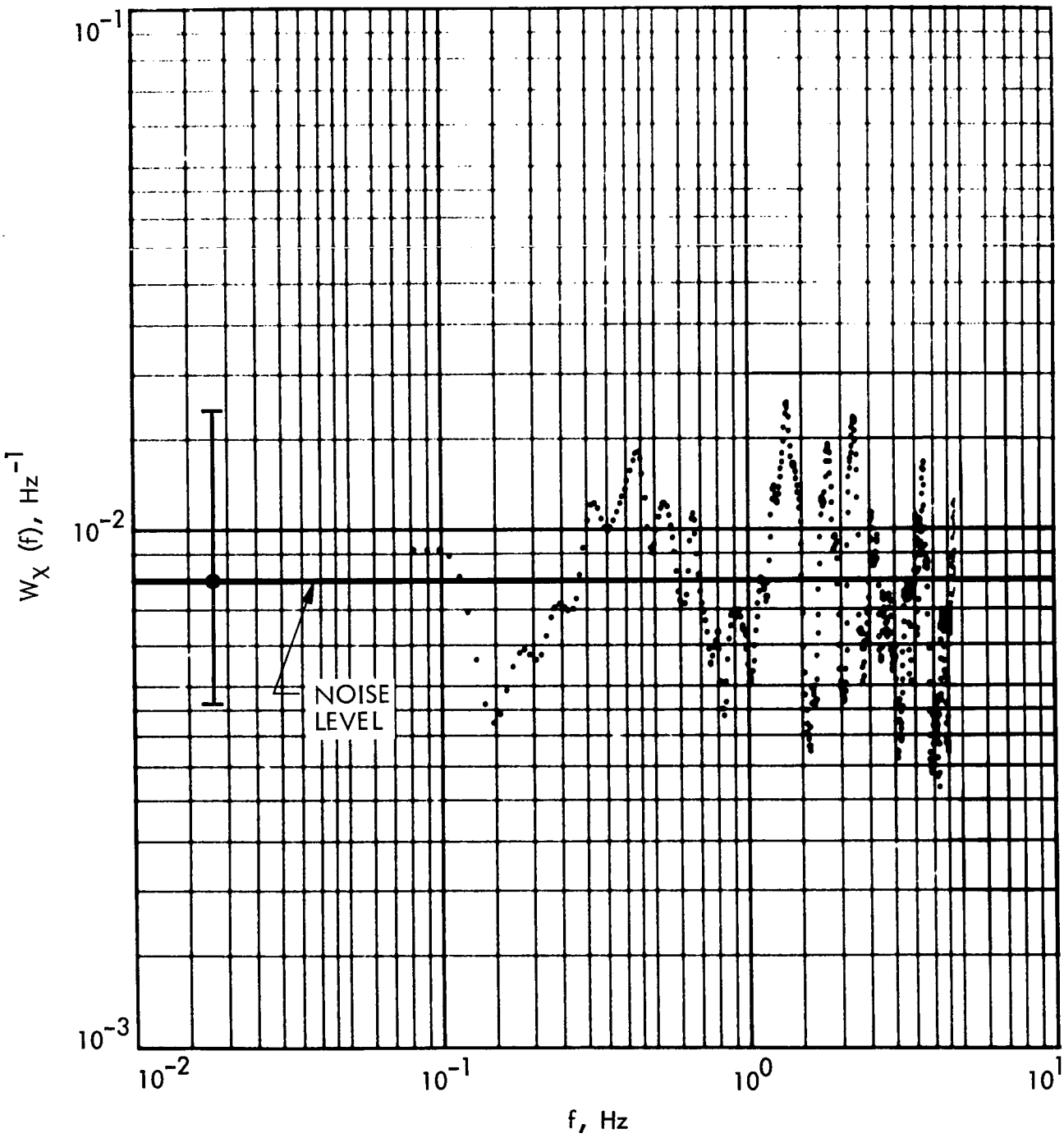

Figure 12c. Region C of Entrance Occultation: B_L = 5 Hz, τ_{AGC} = 0.033 secs, h = 0.03 secs, m = 21.

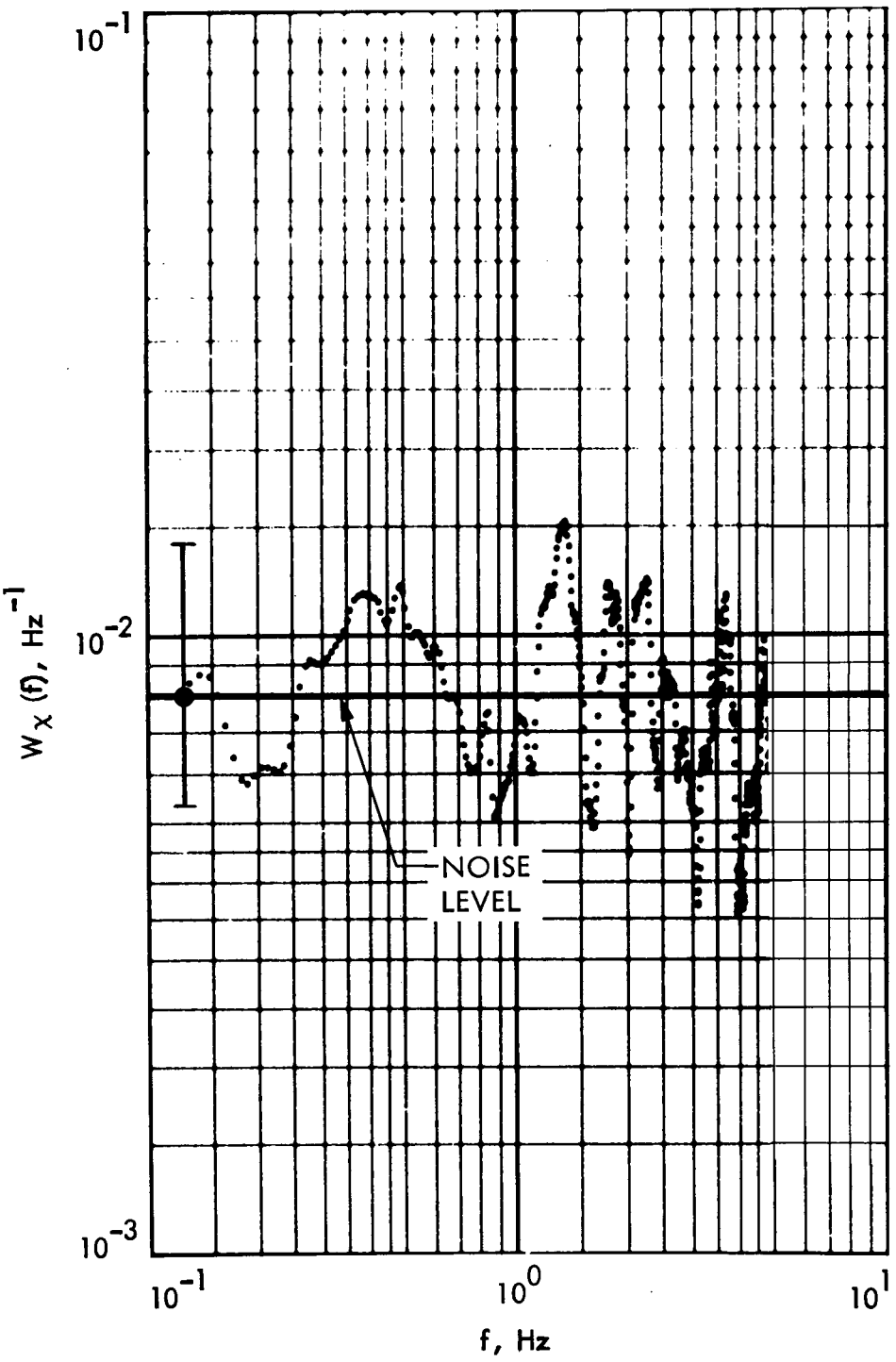

Figure 12d. Region C of Entrance Occultation: B_L = 5 Hz, τ_{AGC} = 0.033 secs, h = 0.03 secs, m = 31.

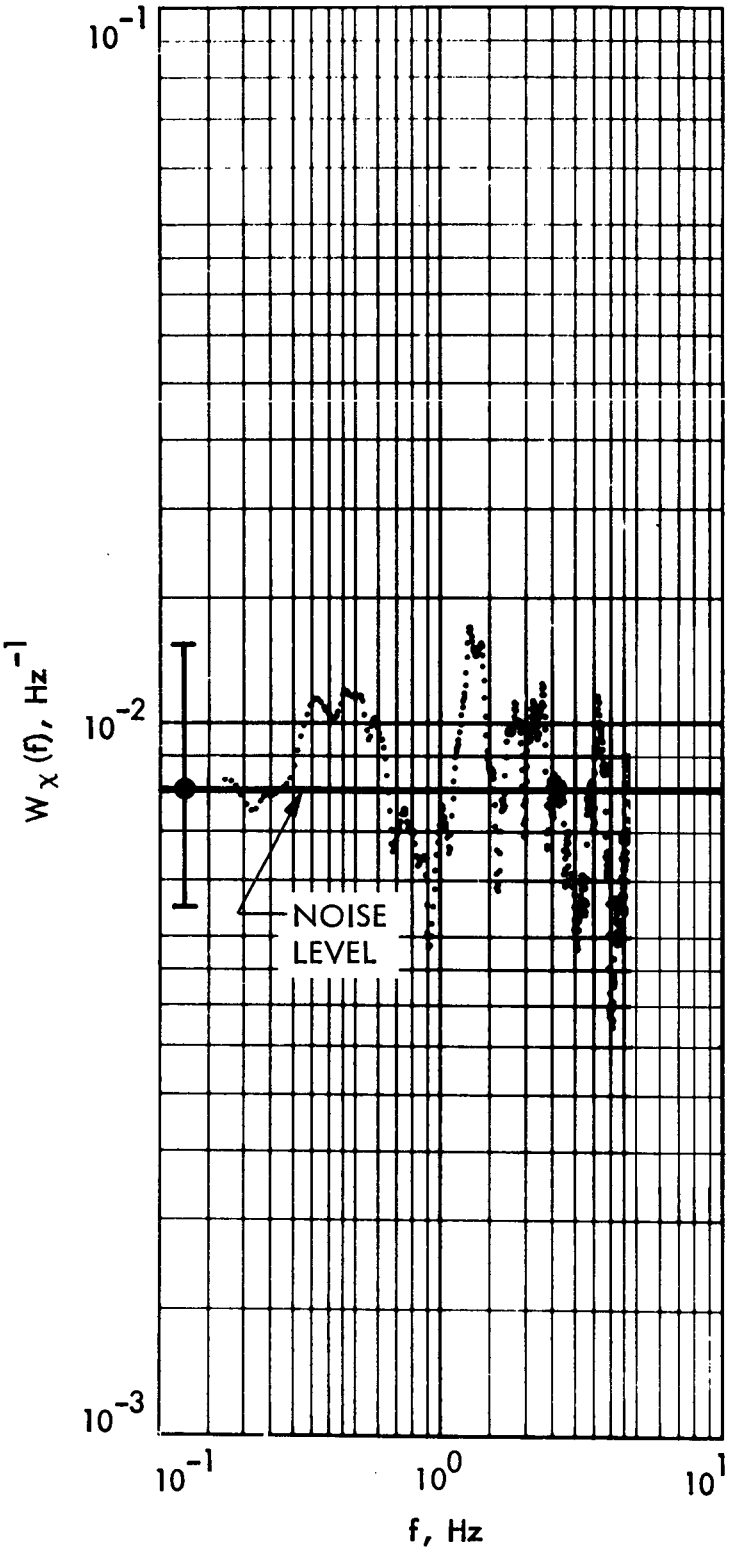

Figure 12e. Region C of Entrance Occultation: B_L = 5 Hz, τ_{AGC} = 0.033 secs, h = 0.03 secs, m = 41.

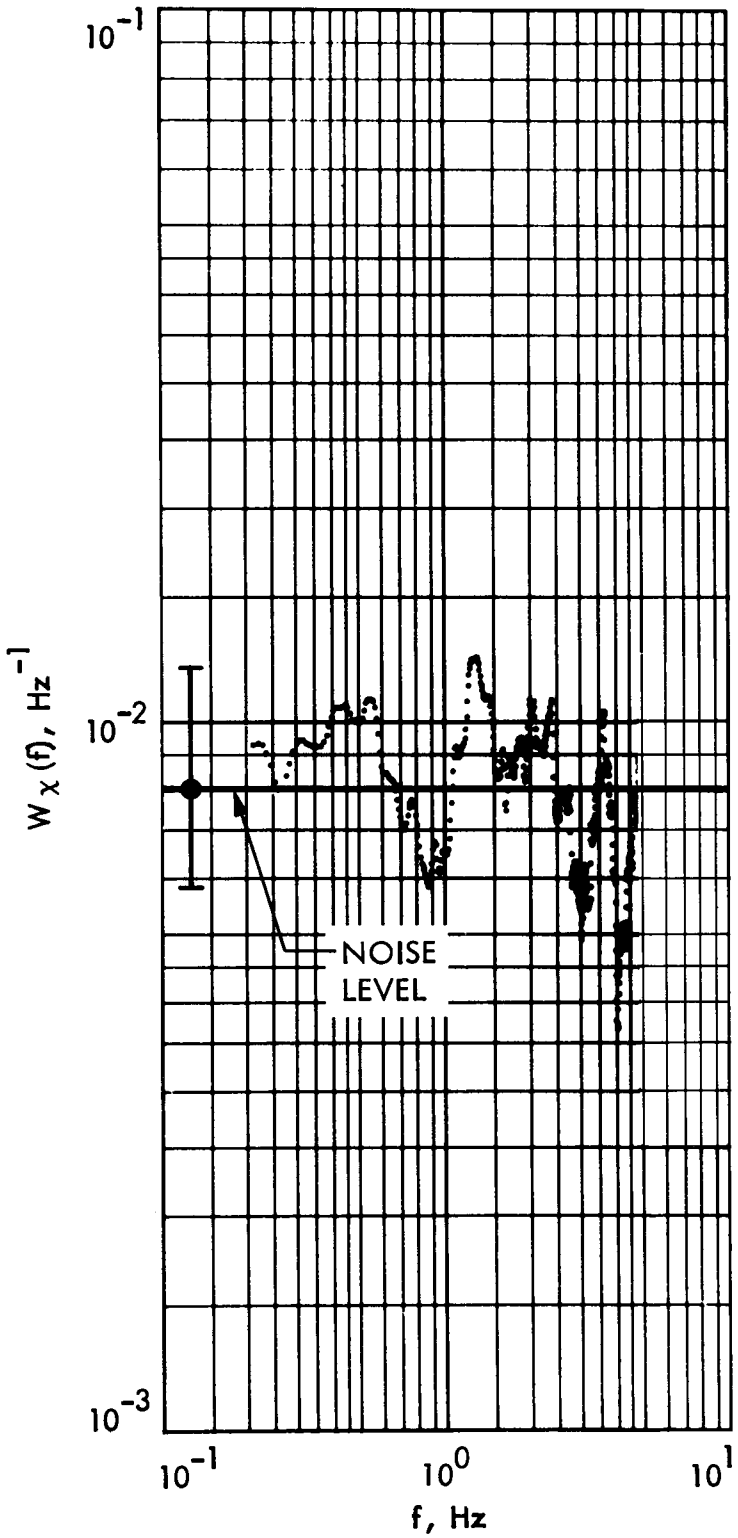

Figure 12f. Region C of Entrance Occultation: B_L = 5 Hz, τ_{AGC} = 0.033 secs, h = 0.03 secs, m = 51.

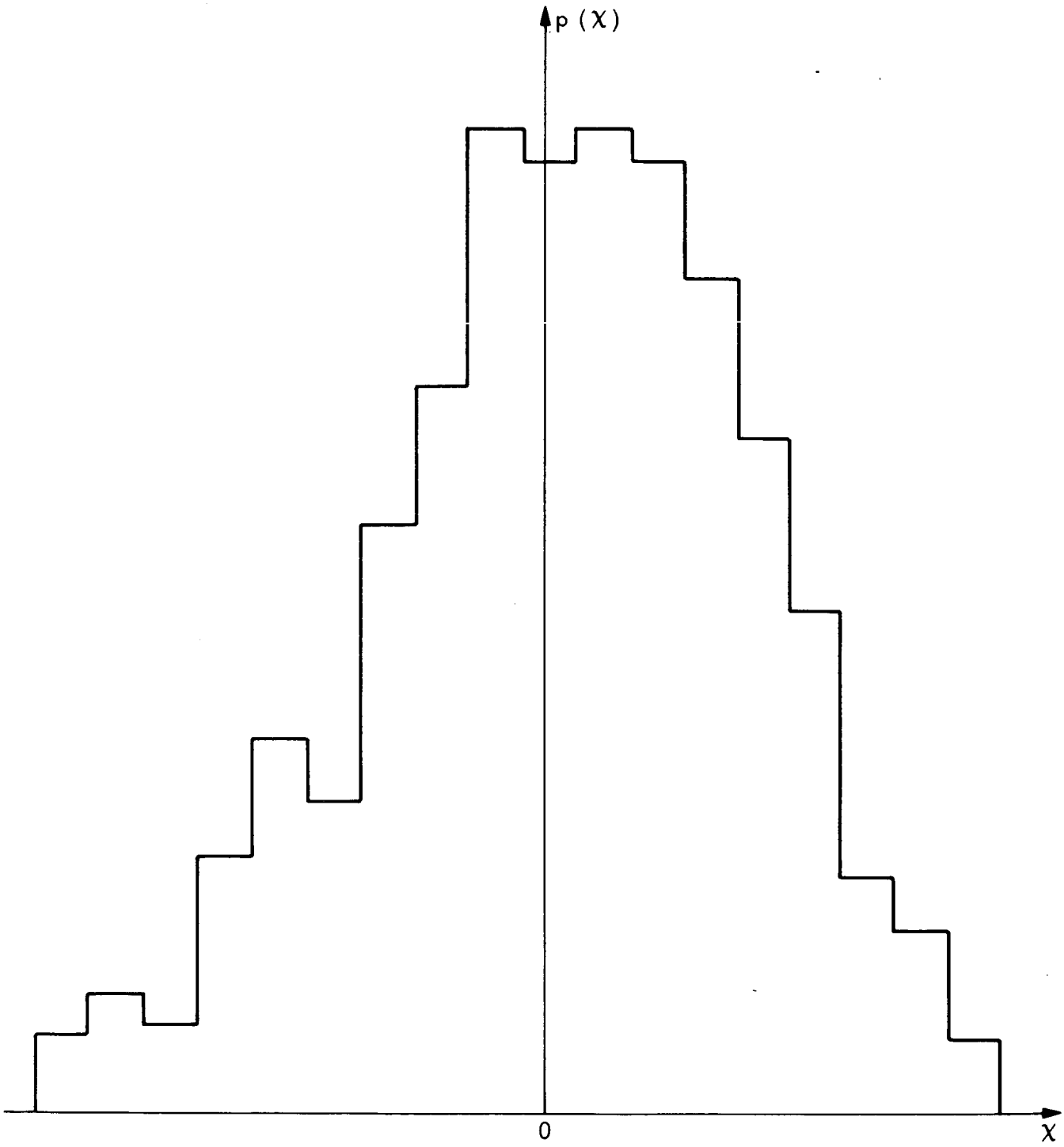

Figure 13. Histogram of χ

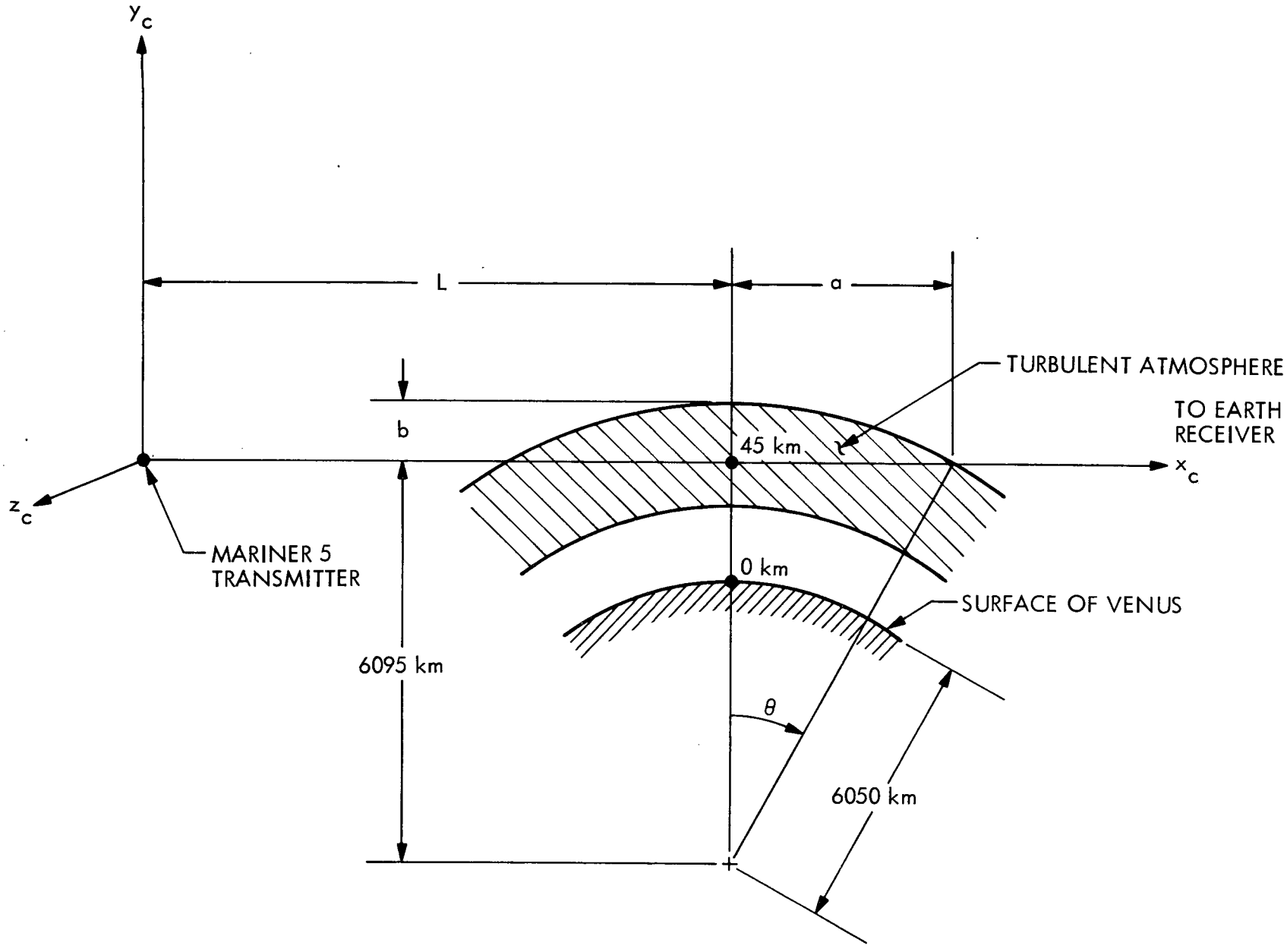

Figure 14. Mariner 5 Occultation Configuration

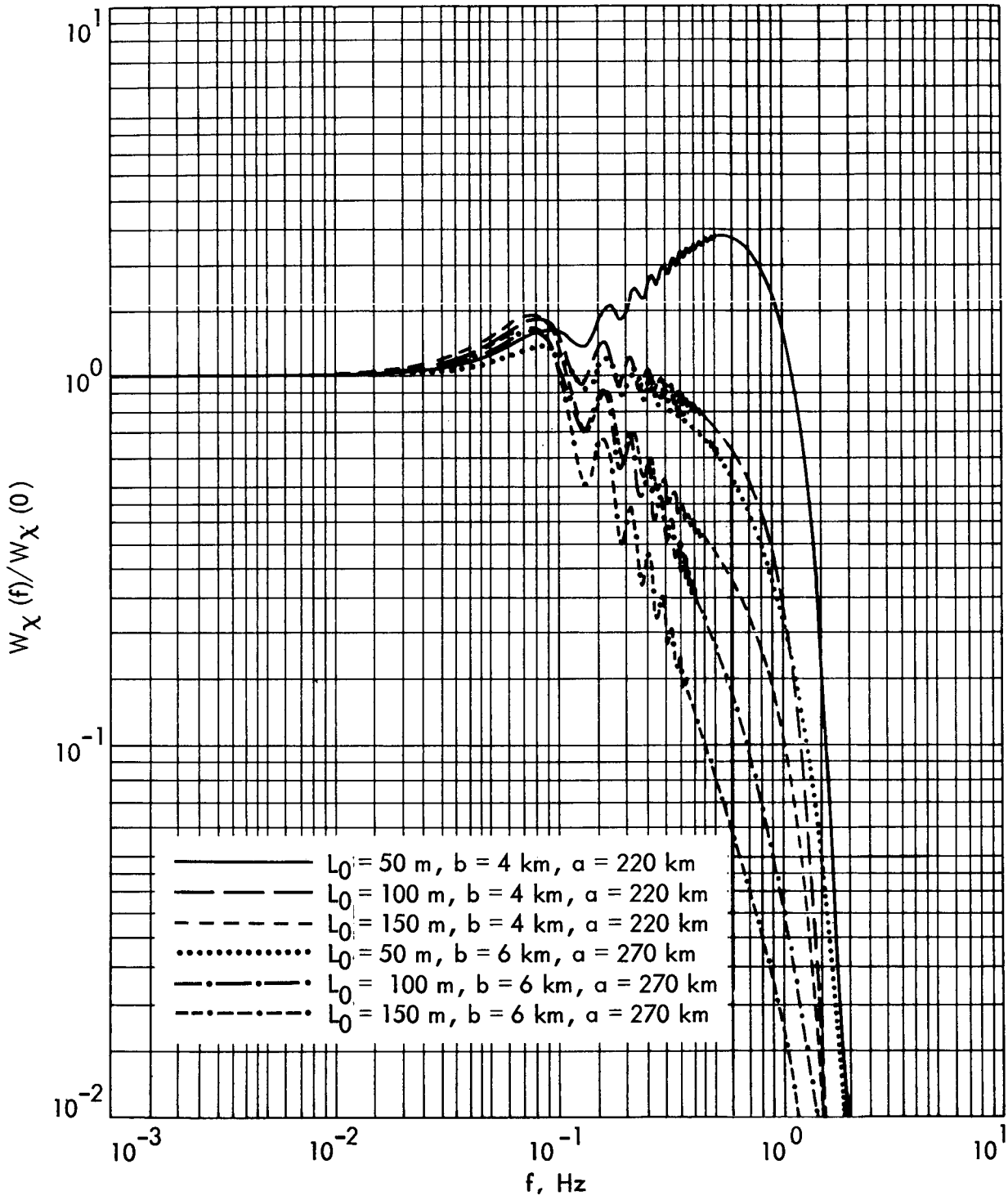

Figure 15. Theoretical Power Spectrum of the Log-Amplitude Fluctuations for Entrance Occultation for Various Values of L_0, b and a: v = 150 m/sec, t_c = 48 secs, L = 8,400 km.

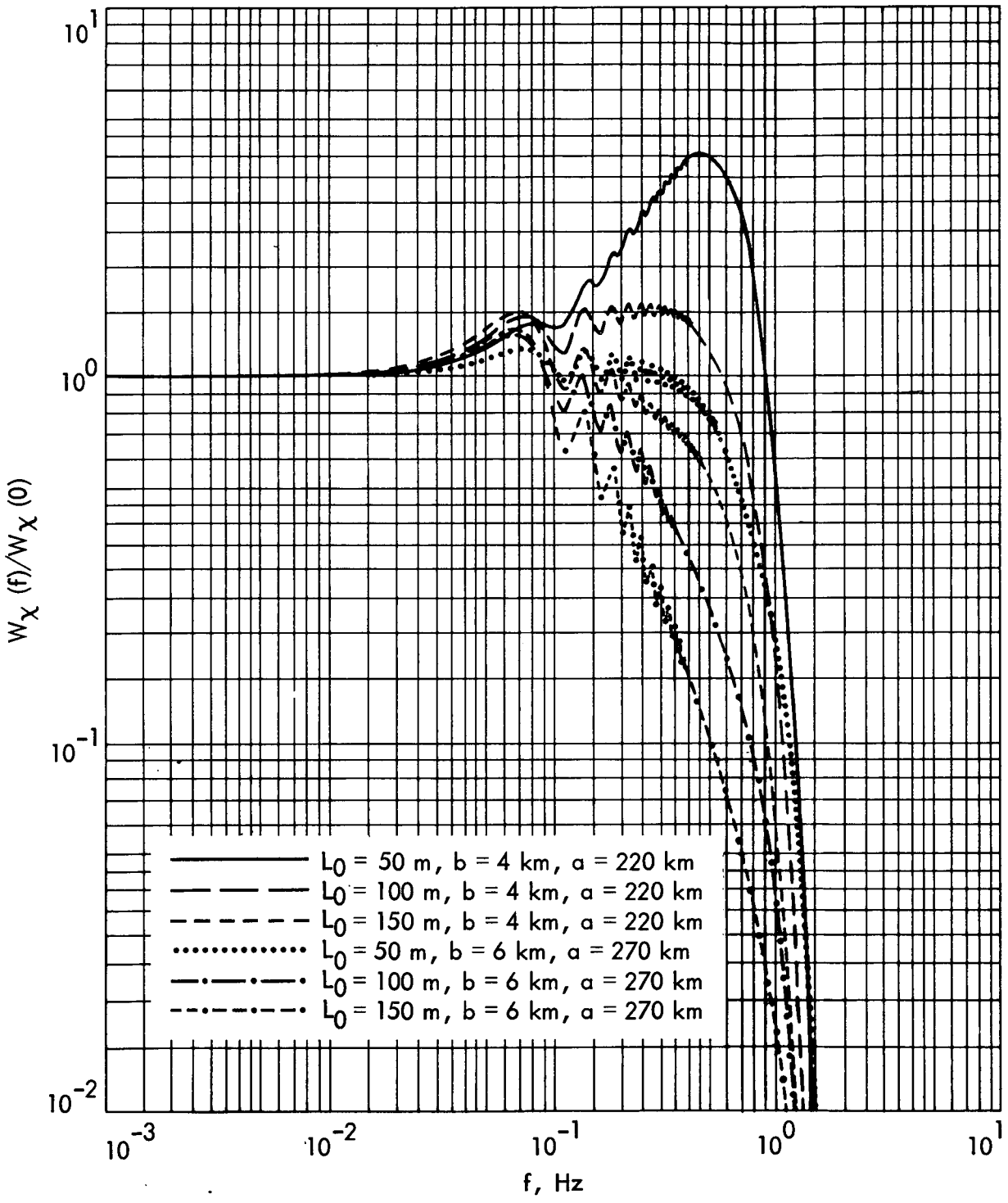

Figure 16. Theoretical Power Spectrum of the Log-Amplitude Fluctuations for Exit Occultation for Various Values of L_0, b and a: v = 150 m/sec, t_c = 48 secs, L = 12,000 km.

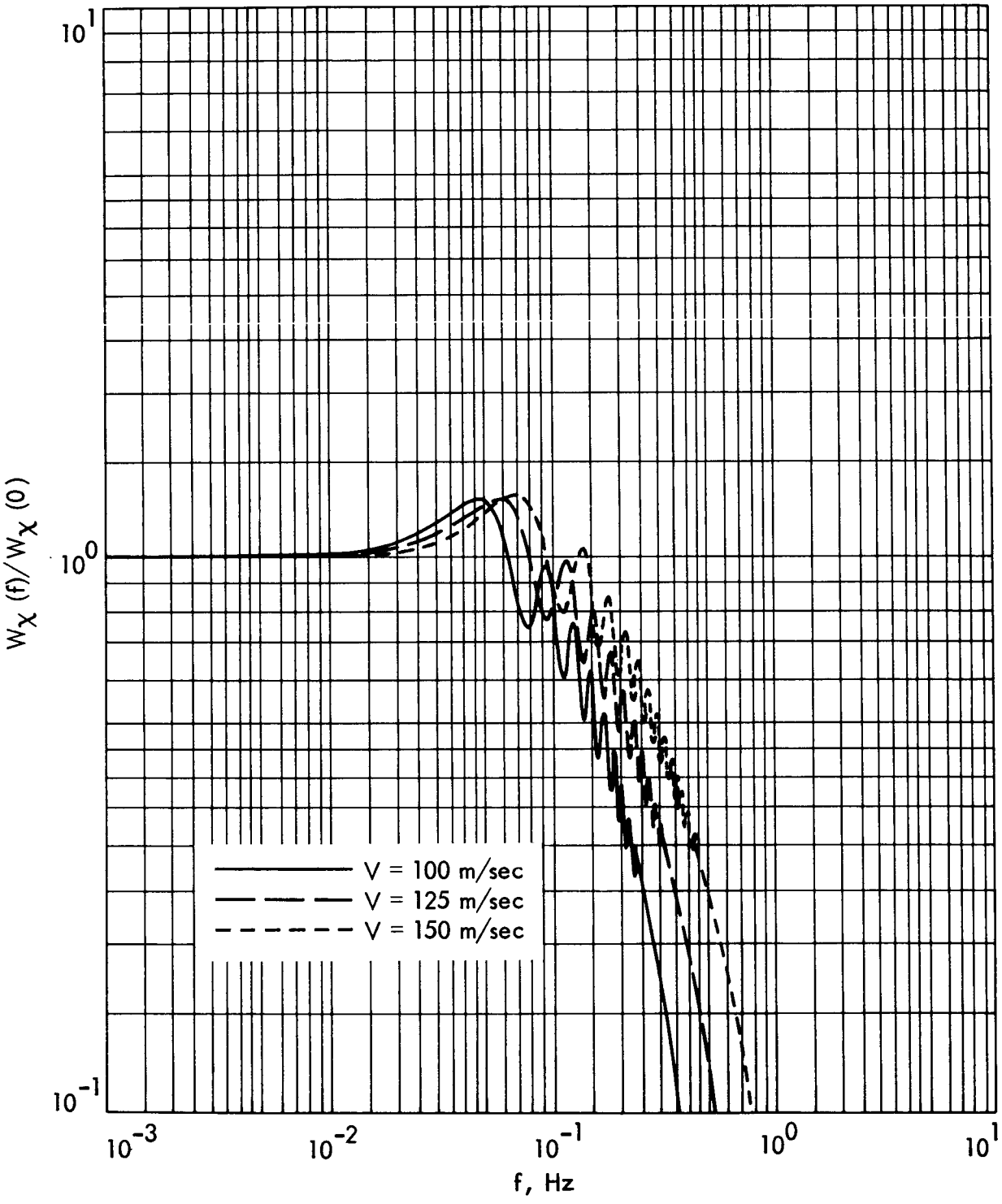

Figure 17. Theoretical Power Spectrum of the Log-Amplitude Fluctuations for Exit Occultation for Various Values of v : L_0 = 100 m, b = 6 km, a = 270 km, t_c = 48 secs, L = 12,000 km.

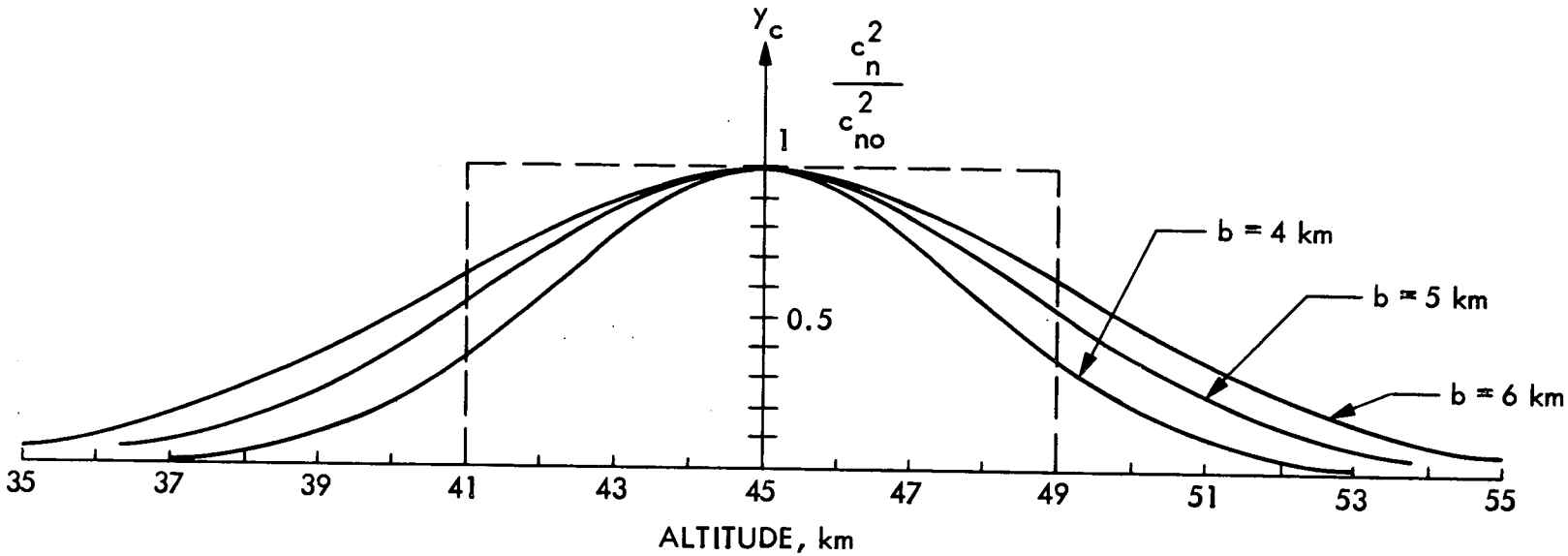

Figure 18. Variation of Normalized Structure Constant With Altitude

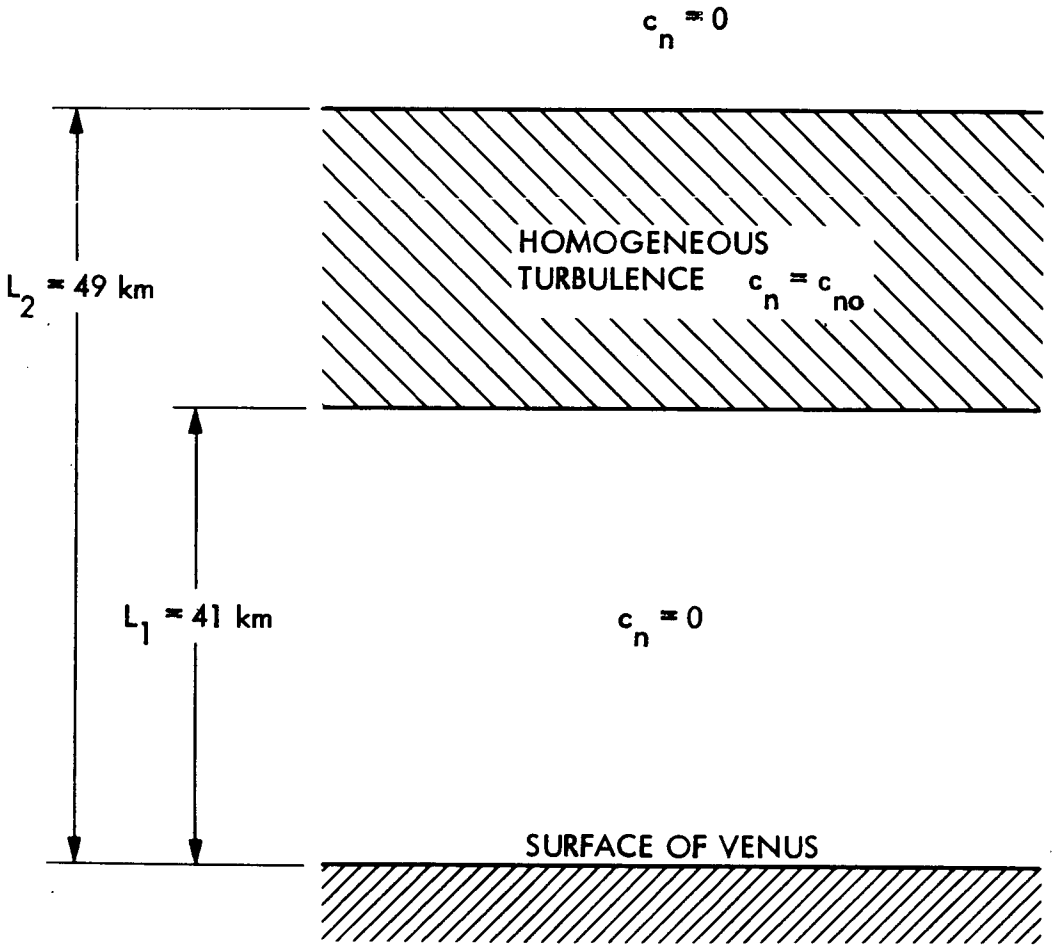

Figure 19. Turbulence Model

APPENDIX A

CONTENTS

APPENDIX A

SIGNAL PROCESSING TO EXTRACT TURBULENCE-INDUCED SIGNAL FLUCTUATIONS

In this Appendix we will describe the processing steps which are required to first extract the amplitude and phase variations which are imposed on a signal received from a spacecraft occulted by Venus, and to then measure the spectra of these variations and separate the resulting spectra into components attributable to (1) atmospheric turbulence, and (2) noise at the input to the receiver.

A.1 SIGNAL RECEPTION AND PRE-PROCESSING

A.1.1 The Received Signal

The signal transmitted from the spacecraft at time t will be received on earth some time later due to delays which can be attributed to several different effects. Generally these effects can be classified as Venusian atmospheric effects, and trajectory effects. By trajectory effects we mean simply the delay component caused by the propagation time (at the speed of light) required for the signal to propagate in a straight line from the spacecraft to the earth. For our purposes this component can be assumed known. There are two atmospheric effects which cause a further signal delay, viz., the lengthening of the propagation path due to refraction around Venus, and the slower propagation speed through the Venusian atmosphere. Both of these atmospheric effects can be divided into two more effects, viz., (1) the delay caused by the "average", or non-turbulent, Venusian atmosphere, and (2) deviations from this average caused by turbulence and other atmospheric non-homogeneities. It is this last component which it is desired to analyze.

Let the delay which the signal received at time t has undergone be denoted by d(t). [The signal received at time t was transmitted from the spacecraft at time t-d(t)]. Then we can write

$$d(t) = d_t(t) + d_a(t) + d_n(t) \tag{1}$$

where

$d_t(t)$ = delay caused by the spacecraft trajectory,

$d_a(t)$ = delay caused by the "average" Venusian atmosphere,

$d_n(t)$ = delay caused by non-homogeneities in the Venusian atmosphere.

The signal which is transmitted from the spacecraft for processing on the ground is a phase-modulated carrier with the carrier not completely suppressed. For estimating the signal delay the (assumed constant) carrier at frequency f_{sc} will be processed. Therefore, the signal received at time t is simply

$$s(t) = A\sqrt{2}\sin\{2\pi f_{sc}[t-d(t)]\} \tag{2}$$

where

A = rms received signal amplitude.

The phase (in radians) of this signal is

$$\phi(t) = 2\pi f_{sc}[t-d(t)] \tag{3}$$

and the frequency (in Hz) is

$$f(t) = \frac{\phi'}{2\pi} = f_{sc} - f_{sc}d'(t)$$

$$= f_{sc} - f_{sc}[d'_t + d'_a + d'_n]. \tag{4}$$

A.1.2 The Ground Receiver

For our purposes a simplified model of the ground receiver, as shown in Fig. A-1, can be used. In effect the receiver simply adds (unavoidable) noise

to the received signal, bandpass filters the sum, multiplies the result by a constant-frequency local oscillator (LO) which shifts the signal down to base band and also up to an image frequency, and then lowpass filters the result to reject the high-frequency image. The result of all this is just to add receiver noise to the signal and to shift all frequencies down by the LO frequency f_{LO}. Therefore, the output of the receiver can be represented as

$$r(t) = n(t) + A\sqrt{2}\sin\{2\pi[(f_{sc} - f_{LO})t - f_{sc}d(t)]\}. \tag{5}$$

This signal, along with a reference timing signal, is recorded on an analog tape recorder for subsequent processing.

A.1.3 Digitization

The next step in signal processing is digitizing the data for computer processing. If a signal is bandlimited to a bandwidth W Hz, then it can be represented exactly by its samples spaced no more than 1/2W sec apart. Mathematically, this can be expressed as

$$r(t) = \sum_i r_i \operatorname{sinc}\left(\frac{t-t_i}{\Delta t}\right) \tag{6}$$

where

$$\operatorname{sinc}(x) = \frac{\sin \pi x}{\pi x}$$

$r_i = r(t_i)$ = samples of the received signal,

t_i = time of i^{th} equispaced sample r_i,

Δt = time between samples.

Due to the bandpass and lowpass filters in the receiver, the signal r(t) is bandlimited to less than 80kHz, so it could be sampled at any rate greater than 160,000 samples/sec without losing any signal information. The actual signal is sampled at a rate of 320,000 samples/sec. This produces a digitized signal which contains all spectral components up to 160 kHz.

A.1.4 Frequency Shifting

The spectrum of the (digitized) recorded signal r(t) is typically as shown in Fig. A-2a. It consists of broadband noise plus a signal component at the time-varying frequency $f(t) - f_{LO}$. The purpose of the filter-and-decimate operation is to first frequency shift the signal so that the time variation of the signal frequency is eliminated, and then to pass the result through a very narrowband filter, and, finally, to reduce the data sampling rate to a value corresponding to the new narrow bandwidth. Once this is done, the signal will be represented by relatively few samples which can be efficiently further processed in a computer.

The signal component of the received signal r(t) is

$$r_s(t) = A\sqrt{2}\sin\{2\pi[(f_{sc} - f_{LO})t - f_{sc}d(t)]\}. \tag{7}$$

This is multiplied by the output of a programmed local oscillator whose frequency is $f_S(t)$, i.e., it is multiplied by $\sqrt{2}\sin[2\pi f_S(t)t]$. The result is

$$A\sin\{2\pi[(f_{sc} - f_{LO} + f_S(t))t - f_{sc}d(t)]\}$$
$$+ A\sin\{2\pi[(f_{sc} - f_{LO} - f_S(t))t - f_{sc}d(t)]\}, \tag{8}$$

i.e., half of the signal power is shifted up in frequency by $f_S(t)$ and half is shifted down by the same amount. In practice the frequency $f_S(t)$ is taken as a spline-curve which compensates for the trajectory and average-atmosphere components of the signal's frequency shift. In other words, $f_S(t)$ is taken to be

$$f_S(t) = 80 \text{ kHz} - \{f_{sc} - f_{LO} - f_{sc}(d'_t + d'_a)\} \tag{9}$$

where

f_{sc} = carrier frequency transmitted from spacecraft,

f_{LO} = receiver local-oscillator frequency,

d'_t = time derivative of trajectory delay component,

d'_a = time derivative of average atmosphere delay component.

Therefore, the upshifted signal component appears at frequency

$$f_{sc} - f_{LO} + f_S(t) - f_{sc}d'(t) = 80 \text{ kHz} - f_{sc}d'_n. \tag{10}$$

Of course, in order to do this it is necessary for the frequencies f_{sc} and f_{LO} and the delay-rate components d'_t and d'_a to be known. At this point we can accomplish this by simply defining these quantities to be our estimates of them. This will result in any errors in these estimates being included in the delay component $d_n(t)$ which, up until now, we have attributed to atmospheric non-homogeneities. Thus it must be remembered that in later stages of the processing these errors in our estimates of the other delays must be recognized and removed. This will be done primarily be assuming that the errors in our estimates if d'_t and d'_a are more slowly varying functions of time than is d'_n, i.e., separation will be done in the spectral domain.

The noise component of the received signal r(t) is shifted both up and down (half the power in each direction) in frequency by $f_S(t)$, just as the signal component is. The total upshifted spectrum is therefore as shown in Fig. A-2b, and the downshifted spectrum is as shown in Fig. A-2c. The spectrum of the multiplier is then the sum of the spectra shown in Figs. A-2b and A-2c. Note, however, that in the vicinity of 80 kHz only the upshifted spectrum of Fig. A-2b contributes to the sum. Therefore, a narrowband filter used to pass only the spectral components near 80 kHz will pass the signal components (half of the signal power), and half of the noise power present before multiplication. Thus, at no loss in signal-to-noise ratio, we have converted the received signal into a signal whose phase is

$$2\pi[(f_{sc} - f_{LO} + f_S(t))t - f_{sc}d(t)] = 2\pi[8x10^4 t - f_{sc}d_n] + k_1 \qquad (11)$$

where k_1 is an arbitrary (and unimportant) constant phase offset. The atmospheric-induced delay d_n will be extracted by further processing of this signal.

A.1.5 Filtering and Decimation

As indicated above, the output of the multiplier (mixer), which performs the multiplication of the received signal by the programmed local oscillator, is passed through a narrowband filter centered at 80 kHz. If the bandwidth of this filter is Δ, then the spectrum at its output will be similar to that illustrated in Fig. A-3.

It has already been indicated that a signal which is band limited to a bandwidth W can be completely represented by only its samples taken every 1/2W sec. More exactly, this theorem (the "sampling theorem") states that if a signal

is sampled every 1/2W sec, then its spectral components in each of the frequency intervals iW to (i+1)W, i=0,1,2,$\cdots$, are "folded" into the interval 0 to W. Of course, if the signal has no spectral components above W, then no higher frequency components are folded down, and the original signal is completely represented by its samples. However, if higher-frequency components are present, then a component at frequency f in the interval $iW \leq f \leq (i+1)W$ is "folded" down to appear at frequency f_W, where

$$f_W = \begin{cases} f - iW & i \text{ even} \\ (i+1)W - f & i \text{ odd.} \end{cases} \tag{12}$$

Thus, the frequency intervals corresponding to even i are simply frequency shifted down to the baseband (0,W), and the frequency intervals corresponding to odd i are shifted down to the baseband, but frequency reversed. This effect is used to shift the spectrum shown in Fig. A-3 down to the baseband $(0,\Delta)$, by reducing the sampling rate of the signal.

The original sampling rate of the recorded signal r(t) is 320,000 samples/sec. This is reduced by a factor of N (the signal is decimated by N) by simply keeping only every N^{th} sample output from the narrowband filter of bandwidth Δ. For this, N is taken to be odd, and the bandwidth Δ is adjusted to be $\Delta = 160{,}000/N$. The new sampling period is then N/320,000, so in the sampling theorem we have

$$\text{Sampling Period} = \frac{1}{2W} = \frac{N}{320{,}000} \tag{13}$$

or

$$W = \frac{160{,}000}{N} = \Delta. \tag{14}$$

Thus, after decimation all the signal energy will appear in the baseband $(0, \Delta)$. Furthermore, all signal and noise components before decimation lie in the frequency interval

$$80{,}000 - \Delta/2 \leq f \leq 80{,}000 + \Delta/2. \tag{15}$$

But Δ is chosen so that

$$80{,}000 = N\Delta/2. \tag{16}$$

Therefore, this signal-frequency interval can be expressed as

$$N\Delta/2 - \Delta/2 \leq f \leq N\Delta/2 + \Delta/2 \tag{17}$$

$$\frac{N-1}{2}\Delta \leq f \leq \frac{N+1}{2}\Delta \tag{18}$$

or, since $\Delta = W$ and the decimation factor N is chosen to be odd,

$$iW \leq f \leq (i+1)W \tag{19}$$

where

$$i = \frac{N-1}{2}.$$

Thus, the decimation parameters are chosen so that the signal and noise all lie in <u>one</u> frequency interval, so that after decimation they will appear in the baseband $(0,\Delta)$ without any frequency "foldover" or aliasing.

Normally N is chosen so that i is even (a value of N = 101 was used for the results contained in this report), so the signal of bandwidth Δ centered at 80

kHz is simply downshifted in frequency by an amount $[(N-1)/2]\ \Delta = 80\ \text{kHz} - \Delta/2$ due to the decimation. (The amount of decimation which could be used is limited only by how small a bandwidth Δ will contain the signal frequency component $f_{sc}d'_n$.) Note that the frequency of the signal after this operation is $\Delta/2 - f_{sc}d'_n$, and the phase of the signal is

$$\phi = 2\pi[(\Delta/2)t - f_{sc}d_n] + k_1 \tag{20}$$

The signal and noise amplitudes, and their fluctuations, have, of course, been preserved through all of these pre-processing steps.

A.2 PHASE-LOCKED-LOOP PROCESSING

The signal $v(t)$ from the receiving and pre-processing operations is given by

$$v(t) = A(t)\sqrt{2}\ \sin\{2\pi[(\Delta/2)t - f_{sc}d_n(t)] + k_1\} + n(t) \tag{21}$$

where now we explicitly indicate that the amplitude A(t) is a function of time. This time variability is due to four factors: (1) the increasing distance from the spacecraft to the receiver, (2) the changing orientation of the spacecraft antenna as the spacecraft passes behind the planet, (3) the changing average atmospheric attenuation as the received signal passes deeper and deeper through the planetary atmosphere, and (4) the variable turbulence-induced scattering of the signal as it passes through the planetary atmosphere. It is this last component which is of primary interest here.

In order to quantitatively determine the effects of planetary turbulence, it is necessary to extract (or estimate) the amplitude A(t) and the phase $f_{sc}d_n(t)$

from the signal $\nu(t)$. This is accomplished by computer processing which extracts the phase with a digital phase-locked loop (PLL) and the amplitude with a digital coherent amplitude estimator.

A.2.1 Phase Extraction

Here we will not give a complete description of the workings of the phase-locked loop, since several good references on this subject (Refs. A1-A3) are readily available. Instead, we will simply note that the PLL is a non-linear phase-tracking device which can normally (when it is tracking) be well approximated as a device whose input is of the form

$$x(t) = A\sqrt{2}\,\sin\{2\pi f_{vco}\,t + \theta_1(t)\} + n(t) \tag{22}$$

where f_{vco} is the quiescent frequency of the PLL's VCO, and which extracts the phase $\theta_1(t)$ from the signal. In the process of doing this, the PLL passes the phase θ_1 and the noise $n(t)$ divided by the amplitude A, through a lowpass filter to produce θ_2, a noisy estimate of the phase θ_1. In other words, the output phase estimate $\theta_2(t)$ is that which would be obtained by passing the input phase deviation $\theta_1(t)$ through a lowpass filter, plus an error which can be thought of as coming from passing white noise through the same lowpass filter.

When using the PLL to estimate the signal delay component due to atmospheric non-homogeneities, the VCO quiescent frequency is set at $\Delta/2$ so that

$$\theta_1(t) = -2\pi f_{sc} d_n + k_1. \tag{23}$$

The phase estimate $\theta_2(t)$ is then simply noise plus a term proportional to the desired delay component d_n lowpass filtered.

The transfer function of the equivalent lowpass filter of the linearized second-order PLL is (Ref. A1, Eq. 5-19)

$$L(s) = \frac{1 + \left(\frac{R+1}{4B_L}\right)s}{1 + \left(\frac{R+1}{4B_L}\right)s + \left(\frac{R+1}{4B_L\sqrt{R}}\right)^2 s^2} \tag{24}$$

$$= \frac{1 + (2\zeta/W_n)s}{1 + (2\zeta/W_n)s + s^2/W_n^2}$$

where

B_L = one-sided loop noise bandwidth (Hz),

R = Tausworthe's damping parameter,

W_n = loop natural radian frequency,

ζ = loop damping factor.

Note that these parameters are related by

$$B_L = \frac{4\zeta^2 + 1}{8\zeta} W_n , \tag{25}$$

$$R = 4\zeta^2, \tag{26}$$

$$W_n = \frac{4B_L\sqrt{R}}{R+1} , \tag{27}$$

$$\zeta = \frac{\sqrt{R}}{2} . \tag{28}$$

The magnitude and the squared magnitude of the filter transfer function $L(j2\pi f)$ are shown in Figures A-4a and A-4b, respectively.

A.2.2 Phase Errors

The phase estimate $\theta_2(t)$ produced by the PLL will differ from the desired phase $\theta_1 = 2\pi f_{sc} d_n + k_1$, due to two factors, viz., (1) higher-frequency variations in $\theta_1(t)$ will be filtered out by the lowpass filter L(s) (unless the loop bandwidth B_L is made sufficiently large), and (2) the low-frequency components of the noise n(t)/A, which in this case has an essentially flat spectrum, will pass through the filter L(s). Thus, it is clear that for the best possible phase-estimate accuracy, the loop bandwidth used should be as small as possible, consistent with the requirement that it pass all significant variations in the input phase θ_1.

If we let

$$\begin{aligned} \phi &= \text{Phase error (rad)} \\ &= \theta_1(t) - \theta_2(t) \end{aligned} \tag{29}$$

and

$S_\phi(f)$ = one-sided spectral density of ϕ due to noise, (30)

then for spectrally flat noise, which is typical of the receiver noise present at the input to the PLL, with one-sided power spectral density N_0 watts/Hz, we get

$$S_\phi(f) = \frac{N_0}{A^2} \left| L(j2\pi f) \right|^2 \tag{31}$$

where N_0/A^2 is the spectral density of the noise at the input to the equivalent lowpass filter L(s), and A^2 is the power in the signal into the PLL (see Ref. A2, Sec. 2.8). Thus, the spectral density of the noise-induced phase error will have the shape shown in Fig. A-4b, and a level which depends on the signal-to-noise ratio (SNR) N_0/A^2.

The mean squared value σ_ϕ^2 of the phase error is just

$$\sigma_\phi^2 = \int_0^\infty S_\phi(f)\, df$$

$$= \frac{N_0}{A^2} \int_0^\infty \left| L(j2\pi f) \right|^2 df \tag{32}$$

$$= \frac{N_0 B_L}{A^2}$$

In order for the linearized model of the PLL which we have been assuming to be valid, this mean squared phase error must be less than about $0.1(\text{rad})^2$. Thus,

for all the PLL processing described in this report the loop bandwidth B_L was chosen small enough to satisfy

$$\sigma_\phi^2 = \frac{N_0 B_L}{A^2} \leq 0.1 \tag{33}$$

$$B_L \leq \frac{A^2}{10\ N_0} = \frac{\text{SNR in 1-Hz Bandwidth}}{10} \tag{34}$$

A.2.3 Phase Tracking

As indicated above, one requirement on the choice of loop bandwidth B_L is that it be large enough to pass the significant variations in the input phase $\theta_1(t)$. An important aspect of this is the requirement that the frequency rate of the signal at the input to the PLL not be too large to follow. This is because the second-order PLL tracks a frequency rate with a phase offset of (Ref. A2, Table 2.1)

$$\phi_{ss} = \frac{\pi R (R+1)^2}{8\ B_L^2\ R} \tag{35}$$

where

R = frequency rate (Hz/sec),

B_L = loop bandwidth,

R = Tausworthe's damping parameter.

The value of the damping parameter R used was R = 2, so ϕ_{ss} can be expressed as

$$\phi_{ss} = \frac{\pi R}{2B_L^2} \times \frac{9}{8} \approx \frac{\pi R}{2B_L^2} \tag{36}$$

For the PLL to track, this steady-state phase error must be kept below about $90° = \pi/2$. Therefore, the bandwidth must satisfy

$$\frac{\pi R}{2B_L^2} < \frac{\pi}{2} \tag{37}$$

or

$$B_L > \sqrt{R} \tag{38}$$

which, when combined with the phase-error requirement above, leads to

$$\sqrt{R} < B_L < \frac{A^2}{10\ N_0}. \tag{39}$$

An obvious possibility when tracking signals transmitted from deep space by an accelerating spacecraft is that

$$\frac{A^2}{10\ N_0} < \sqrt{R} \tag{40}$$

due to a low SNR and a high doppler. In this case reliable PLL tracking would not be possible. It was precisely to counteract this situation, by removing most

of the signal's frequency variations, that the pre-processing described in Section A.1 was performed.

A.2.4 Amplitude Extraction

The estimates of the signal's time-varying amplitudes A(t) which are used to detect and characterize the turbulence of the Venusian atmosphere are produced by a coherent amplitude-estimating circuit which works in conjunction with the PLL. Actually, two such circuits are implemented as part of the PLL. One of these acts as an AGC circuit for the PLL, and its parameters are chosen to optimize its performance in that role. The other is nearly identical, but it is used only to produce amplitude estimates for further processing, and its parameters are chosen to obtain good performance in that role.

A block diagram of the coherent amplitude-estimating circuit, as implemented in computer software, is shown in Fig. A-5. The input signal is $\nu(t)$ from the pre-processing operations described in Section A.1:

$$\nu(t) = A(t)\ \sqrt{2}\ \sin\{2\pi[(\Delta/2)\ t - f_{sc} d_n(t)] + k_1\} + n(t) \qquad (41)$$

where

$A(t)$ = time-varying signal rms amplitude,

Δ = signal-plus-noise bandwidth,

f_{sc} = frequency of transmitted signal,

$d_n(t)$ = delay caused by non-homogeneities in the Venusian atmosphere.

This can be simplified notationally to

$$\nu(t) = A(t)\ \sqrt{2}\ \sin[\omega t + \theta_1(t)] + n(t) \tag{42}$$

by letting

$$\begin{aligned} \omega &= \pi\Delta \\ &= 2\pi f_{vco} \end{aligned} \tag{43}$$

where

f_{vco} = quiescent PLL VCO frequency

and, as in Section A.2.1, by letting

$$\theta_1(t) = -2\pi f_{sc} d_n + k_1. \tag{44}$$

To further simplify the notation we will drop the explicit time dependence of $A(t)$ and $\theta_1(t)$, denoting then by simply A and θ_1. This results in the form for $\nu(t)$ shown in Fig. A-5.

As shown in Fig. A-5, the input signal $\nu(t)$ is first divided by the "gain" W_g, which is derived by the rest of the circuit. The circuit is designed to attempt to adjust W_g so that the ratio A/Wg is held at unity, so that the rms signal amplitude into the PLL is constant at unity. In the amplitude-estimating circuit used only for producing estimates of A(t), the amplitude-stabilized signal $\nu(t)/W_g$ is not fed to the PLL or any other circuit. It is used only in the amplitude-estimating circuit itself. In the amplitude-estimating circuit used as an AGC for the PLL, the signal is fed to the PLL as shown in Fig. A-5.

A nearly coherent signal of the form $\sin(\omega t + \theta_2)$ is obtained from the PLL as described in Section A.2.1, and mixed with the signal $v(t)/W_g$ to produce the signal which drives the AGC circuit. The phase θ_2 is the phase estimate of θ_1 produced by the PLL, and $\theta_1 - \theta_2$ is the PLL tracking error. The output of the mixer can be divided into several components. First, the signal is mixed into a low-frequency component $(A/W_g)\cos(\theta_1 - \theta_2)$, and a double-frequency component at radian frequency 2ω, which is subsequently rejected. The noise into the mixer is of the form

$$\frac{n(t)}{W_g} = \frac{n_1(t)}{W_g}\sin(\omega t + \theta_2) + \frac{n_2(t)}{W_g}\cos(\omega t + \theta_2) \tag{45}$$

where $n_1(t)$ and $n_2(t)$ are orthogonal components of the input noise, each of which has the same spectral density N_0 as the input noise $n(t)$. Therefore, the noise component in the mixer output is

$$\begin{aligned} &\frac{n_1(t)}{W_g}\sqrt{2}\sin^2(\omega t + \theta_2) + \frac{n_2(t)}{W_g}\sqrt{2}\sin(\omega t + \theta_2)\cos(\omega t + \theta_2) \\ &= \frac{n_1(t)}{\sqrt{2}\,W_g} + \text{Double-Frequency Components.} \end{aligned} \tag{46}$$

The output of the mixer has unity subtracted from it, and is then passed through an integrator which effectively rejects the double-frequency components, and, along with the gain A_g, determines the responsiveness of the loop. Finally,

the signal is exponentiated to determine the loop gain W_g, and the estimated rms signal amplitude is taken to be W_g.

The performance of the AGC loop described here was first analyzed in Ref. A4. This analysis was then generalized by Tausworthe in Chapter 7 of Ref. A1. The loop analyzed by Tausworthe is shown in Fig. A-6, which is taken from Figure 7-1 of Ref. A1. It is shown in Refs. A1 and A4 that the loop can be very well approximated as a linear loop if the input and output are identified as the input signal power and the estimated signal power in decibels. To this end, following Ref. A1 let

$$a(t) = 20 \log A(t) \qquad (47)$$

$$= \text{input signal power in dB}$$

and

$$a^*(t) = 20 \log W_g \qquad (48)$$

$$= \text{estimated signal power in dB.}$$

Then the AGC circuit can be represented as approximately linear with a loop transfer function C(s) between a(t) and c(t) given by (see Ref. A1, eq. 7-6)

$$C(s) = \frac{K_{AGC}\, Y(s)}{[1 + K_{AGC}\, Y(s)]\, K_A} \qquad (49)$$

where

$$K_{AGC} = \frac{K_A e_G K_C}{20 \log e}.$$

The quantities in these equations can be related to the parameters used in the actual processing as shown in Fig. A-5 as follows.

$$Y(s) = \frac{1}{s},$$

$$K_A = 20,$$

$$e_G = 1,$$

$$K_C = A_g = \frac{1}{\tau_{AGC}} \frac{1}{\ln 10} = \frac{\log e}{\tau_{AGC}},$$

τ_{AGC} = input parameter to the processing software.

These parameter values give

$$K_{AGC} = \frac{1}{\tau_{AGC}} \tag{50}$$

and

$$C(s) = \frac{1/s\tau_{AGC}}{[1 + 1/s\tau_{AGC}]\ 20} = \frac{0.05}{1 + s\tau_{AGC}} \tag{51}$$

which result in the input signal power (in dB) a(t) being related to the estimated signal power $a^*(t)$ by the block diagram shown in Fig. A-7. Note that the input to the equivalent RC filter (represented by $K_A C(s)$) consists of three terms:

(1) the true signal amplitude a(t) in dB,

(2) a bias of 20 log cos $\phi(t)$ due to phase tracking errors in the PLL,

(3) a noise component $[20(\log e)\ n_1(t)]/W_g$.

Note also that the noise component depends on the value of the gain W_g. However, in most cases of interest the SNR will be high enough for the error in W_g to be

at most moderate, so that $W_g \approx A$, and the noise component can be adequately approximated by

$$\frac{20(\log e)\, n_1(t)}{A}. \tag{52}$$

The power spectral density of n_1 is the same as that of the input noise n(f), viz., N_0. Therefore, the spectral density of the noise into the equivalent circuit shown in Fig. A-7 is approximately

$$\frac{(20 \log e)^2 N_0}{A^2} = 75.4 \left[\frac{N_0}{A^2}\right] \tag{53}$$

where the term in brackets is the input reciprocal SNR in a one-Hz bandwidth. This flat spectrum will be shaped by the squared magnitude of the equivalent RC filter shown in Fig. A-7. The result will be an output error spectrum having the shape shown in Fig. A-8.

A.2.5 Amplitude Errors

There are three basic sources of error in the amplitude estimate $a^*(t)$; one for each of the input terms shown in Fig. A-7. These are:

(1) variations in the true amplitude a(t) are filtered by the RC filter with time constant τ_{AGC} of Fig. A-7, and if these variations are not slow compared to τ_{AGC}, the estimate $a^*(t)$ will not follow the rapid fluctuation components (which suggests using a small value for τ_{AGC}),

(2) the noise term proportional to $n_1(t)$, filtered by the noise bandwidth of the filter, is added to the estimate $a^*(t)$ (which suggests using a large value for τ_{AGC}),

(3) the phase-error term $-20 \log \cos \phi(t)$, which is always positive, is filtered and subtracted from $a^*(t)$, biasing it toward estimated values which are low.

Here we will treat only the second two of these error sources, and will assume that the bandwidth of the equivalent RC filter is large enough (τ_{AGC} is small enough) to pass the true amplitude fluctuations of interest.

A.2.5.1 Bias Errors

Since the low-frequency response of the filter in Fig. A-7 is unity, the expected value of the estimate a*(t) is simply

$$\overline{a^*(t)} = \overline{a(t)} + \frac{20 \log e}{\sqrt{2}\, W_g} \overline{n_1(t)} + 20\, \overline{\log \cos \phi(t)} \tag{54}$$

Now we can use the fact that, for reasonably small phase tracking errors $\phi(t) = \theta_1 - \theta_2$, the approximation $\ln \cos \phi \approx -\phi^2/2$ is valid, to write

$$\overline{\log \cos \phi(t)} \approx - (\log e)\, \sigma^2/2 \tag{55}$$

where σ^2 is the PLL mean-squared phase error. At high SNR's it is well approximated by (see Section A.2.2) $\sigma^2 = N_0 B_L / A^2$, where B_L is the PLL noise bandwidth. Also, the average value of the noise $n_1(t)$ is zero, so we have

$$\overline{a^*(t)} = \overline{a(t)} - (10 \log e)\,\sigma^2$$

$$\approx \overline{a(t)} - 4.34\, N_0 B_L / A^2 \qquad (56)$$

The term A^2/N_0B_L is the SNR within the PLL bandwidth, and for our application it will exceed 10 dB. Therefore, the bias caused by the PLL phase-tracking error will be less than 0.434 dB.

A.2.5.2 Amplitude-Estimate Variance

The variance of the estimate a*(t) can be gotten as the sum of the variances caused separately by the noise and by the phase error. As can be seen from Fig. A-7, the variance due to the noise is just the (constant) power spectral density of the noise times the noise bandwidth of the filter. The latter is given by

$$B_C = \frac{1}{2\pi}\int_0^\infty |K_A C(j\omega)|^2 d\omega = \frac{1}{2\pi}\int_0^\infty \frac{d\omega}{1 + \omega^2\tau_{AGC}^2} = \frac{1}{4\tau_{AGC}} \qquad (57)$$

and, as noted above, the former is given by $75.4\ N_0/A^2$. Therefore, the noise component of the variance of a*(t) is

$$\frac{75.4\ N_0B_C}{A^2} = \frac{18.9\ N_0}{A^2\tau_{AGC}} = 75.4\left[\frac{N_0B_L}{A^2}\right]\frac{B_C}{B_L} \qquad (58)$$

where in the last expression the term in brackets is the reciprocal SNR in the PLL loop bandwidth B_L, and is less than 0.1.

The second contribution to the variance of the estimate a*(t) is that due to the phase error $\phi(t)$. If the phase-error input of Fig. A-7 is again approximated by

$$-20 \log \cos \phi(t) \approx 10 (\log e) \phi^2(t), \tag{59}$$

then to compute the component's contribution to the variance, the power spectrum of $\phi^2(t)$ must be estimated, multiplied by the magnitude squared of the filter transfer function, and integrated over frequency. This can be done approximately by assuming that the spectrum of $\phi(t)$ is flat with a value of σ^2/B_L from 0 to the PLL loop bandwidth B_L. Then the spectrum of $\phi^2(t)$ is triangular with a peak value of $2\sigma^4/B_L$ at zero frequency, decreasing to zero at a frequency of $\pm 2B_L$ (see Ref. A5). A good approximation to the variance at the output of the filter in Fig. A-7 can then be gotten by integrating this spectral density from 0 to the filter bandwidth B_C. This is equivalent to replacing the RC filter by a flat filter of the same noise bandwidth. The result for $B_C \leq B_L$ is

$$\int_0^{B_C} \frac{2\sigma^4}{B_L} \left(1 - \frac{f}{2B_L}\right) df = \frac{2\sigma^4 B_C}{B_L} \left(1 - \frac{B_C}{4B_L}\right). \tag{60}$$

Therefore, the variance in a*(t) due to the phase error $\phi(t)$ is about

$$2(10 \log e)^2 \sigma^4 \left(\frac{B_C}{B_L}\right) \left[1 - \frac{B_C}{4B_L}\right] = 37.7 \left[\frac{N_0 B_L}{A^2}\right]^2 \left(\frac{B_C}{B_L}\right) \left[1 - \frac{B_C}{4B_L}\right]. \tag{61}$$

From the last expression and the one obtained above for the variance contribution due to noise, we obtain the desired result:

$$\text{var}[a^*(t)] = 75.4 \left[\frac{N_0 B_L}{A^2}\right]\left(\frac{B_C}{B_L}\right)\left\{1 + \frac{1}{2}\left[\frac{N_0 B_L}{A^2}\right]\left[1 - \frac{B_C}{4B_L}\right]\right\} \tag{62}$$

Since normally the SNR $A^2/N_0 B_L$ in the PLL loop bandwidth is at least 10, and the bandwidth ratio

$$\frac{B_C}{B_L} = \frac{1}{4B_L \tau_{AGC}} \tag{63}$$

is smaller than unity, this variance is well approximated by

$$\text{var}[a^*(t)] \approx 75.4 \left[\frac{N_0 B_L}{A^2}\right]\frac{B_C}{B_L} \tag{64}$$

which is just the component due to noise, and which will be less than one $(\text{dB})^2$ for $\tau_{AGC} \geq 2/B_L$. In other words, the contribution of the phase error to the variance is normally negligible, so the approximations we used in calculating it are not critical.

A.2.6 Amplitude Tracking

Since subsequent processing of the amplitude estimates a*(t) will be aimed at determining the power spectrum of the fluctuations in a*(t), the most critical information required about the amplitude tracking (estimation) errors in a*(t) is their spectrum. As shown above in Section A.2.4 and Fig. A-8, at frequencies well below $1/2\pi\tau_{AGC}$ the spectral level of the noise-induced error in a*(t) will be $75.4\ N_0 A^2\ (\text{dB})^2/\text{Hz}$. At higher frequencies this will be modified by the squared

magnitude of the equivalent RC filter of Fig. A-7, and will fall off by factor of 100 for every decade increase in frequency above $1/2\pi\tau_{AGC}$.

Another important consideration is the selection of the time constant τ_{AGC}. Clearly, this should be small enough to pass the actual fluctuations of interest in the true signal amplitude a(t). However, if it is too small the noise induced error in a*(t) will cause the amplitude tracking error a*(t) will cause the amplitude tracking error a*(t) - a(t) to be too large for the linear model of Sections A.2.4 and A.2.5 to be valid.

The approximation which leads to the linear model is replacement of the signal component

$$\frac{A}{W_g} \cos (\theta_1 - \theta_2) - 1 \tag{65}$$

at the input of the integrator of Fig. A-5, by

$$\ell n \left[\frac{A}{W_g} \cos (\theta_1 - \theta_2)\right]. \tag{66}$$

This is a valid approximation so long as

$$\ell n\left[\frac{A}{W_g} \cos (\theta_1 - \theta_2)\right] << 2 \tag{67}$$

or

$$20 \log A + 20 \log \cos (\theta_1 - \theta_2) - 20 \log W_g << 17.4 \tag{68}$$

which is the same as

$$a(t) - a^*(t) + 20 \log \cos (\theta_1 - \theta_2) << 17.4 \text{ dB} \tag{69}$$

We have already seen in Section A.2.5.2 that the standard deviation of the left side of this relation is well approximated by

$$\left\{ \text{var}[a^*(t)] \right\}^{1/2} = \left\{ \frac{18.9\ N_0}{A^2 \tau_{AGC}} \right\}^{1/2} . \tag{70}$$

Therefore, for reliable tracking we must have

$$\left\{ \frac{18.9\ N_0}{A^2 \tau_{AGC}} \right\}^{1/2} << 17.4 . \tag{71}$$

Taking "<<" to mean less than 10%, this can be written as

$$\tau_{AGC} > \frac{18.9\ N_0}{(1.74A)^2} = 6.24\ N_0/A^2 . \tag{72}$$

This condition was satisfied for all data contained in this report.

A.3 SPECTRUM ANALYSIS OF THE AMPLITUDE ESTIMATES

Once the amplitude (in dB) as a function of time has been estimated as described in Section A.2, it is possible to separate this estimate into three components: (1) the fluctuations due to Venusian atmospheric turbulence, (2) the (slowly varying) "trend" component due to average atmospheric attenuation, antenna beam-pattern effects, and changing earth-spacecraft distance, and (3) the variations due to noise at the receiver input. The separation is made in the spectral

domain, and is done in two steps. First, the amplitude estimates a*(t) are "detrended" by fitting a quadratic time function to them, and subtracting it from them. Then, the difference is spectrum analyzed using an FFT algorithm, and theoretical results are used to identify the turbulence components and the noise components.

A.3.1 Amplitude Sampling

As described in Sections A.1 and A.2, the processing which yields the normalized amplitude estimates a*(t) is performed digitally. The time sampling rate of this digital processing is determined by the bandwidth of the processed signal (see Section A.1.4). However, the amplitude estimates produced are low-pass filtered by the response of the (digital) amplitude estimating circuit, as shown in Fig. A-7, to the spectral shape shown in Fig. A-8. Though these estimates are not strictly band limited, at frequencies above $1/2\tau_{AGC}$ their spectrum is attenuated by more than a factor of $1/\pi^2 \approx 0.1$. Therefore, spectral components above a frequency of $1/2\tau_{AGC}$ might be neglected, so that samples of the amplitude could be taken at a rate as low as $1/\tau_{AGC}$, which corresponds to a sampling period as long as τ_{AGC}. Spectral components above a frequency of $1/2\tau_{AGC}$ [i.e., above $2\pi\tau_{AGC}$ f = π in Fig. A-8] would then be "folded" down below this frequency, but only those above a frequency of

$$\frac{1}{2\tau_{AGC}} + \left[\frac{1}{2\tau_{AGC}} - \frac{1}{2\pi\tau_{AGC}}\right] = \left[2 - \frac{1}{\pi}\right] /2\tau_{AGC}$$

would be folded below a frequency of $1/2\pi\tau_{AGC}$, and these would be attenuated by more than a factor of $1/(2\pi-1)^2 \approx 0.036 \approx -14$dB. Thus, if the amplitude estimates

$a^*(t)$ are sampled at a rate no lower than $1/\tau_{AGC}$, the spectrum of these estimates will exist up to a frequency of $1/2\tau_{AGC}$, and all frequency components below $1/2\pi\tau_{AGC}$ will be essentially undistorted.

In the processing described in other parts of this report, the amplitude estimates were sampled at a rate no lower than $1/\tau_{AGC}$.

A.3.2 Normalization and Detrending

The theoretical turbulence results contained in this report are expressed in terms of the normalized amplitudes $\chi(t)$, which are defined as

$$\chi(t) = \ln \frac{A(t)}{\bar{A}(t)} \tag{73}$$

where

$A(t)$ = received signal rms amplitude,

$\bar{A}(t)$ = ensemble average value of $A(t)$.

This can be expressed as

$$\begin{aligned} \chi(t) &= \ln A(t) - \ln \bar{A}(t) \\ &= \frac{\ln 10}{20} \left[20 \log A(t) - 20 \log \bar{A}(t)\right] \\ &= 0.115 \left[a(t) - \hat{a}(t)\right] \end{aligned} \tag{74}$$

where

$a(t)$ = received signal amplitude in dB,

$\hat{a}(t) = \bar{A}(t)$ expressed in dB.

The $\hat{a}(t)$ term is slowly varying, and in the processing is lumped in with the other "trend" components. Thus, our estimate of the fluctuations in $\chi(t)$ is

$$\chi^*(t) = 0.115\ [a^*(t) - \text{Quadratic Fit}] \tag{75}$$

where

$a^*(t)$ = estimated received signal power in dB,

and the "Quadratic Fit" is obtained by making a minimum least squares fit to $a^*(t)$ over the time interval to be analyzed. This essentially removes all slowly-varying components from $\chi^*(t)$.

A.3.3 Spectrum Analysis

The samples of $\chi^*(t)$ which result from the detrending process, are processed through a fast Fourier transform (FFT) routine to estimate the spectrum of $\chi(t)$. This is a conventional FFT routine augmented by two special features: a Hamming window and zero fill. The characteristics of these features are described in detail in Ref. A6. The purpose of the Hamming window is to reduce the spurious "sidelobe" response of strong spectral components (with a corresponding loss in frequency resolution), and the purpose of using zero fill is simply to evaluate the Fourier transform of $\chi^*(t)$ at closer-spaced frequencies than would otherwise be obtained.

A.3.3.1 Hamming Window

If we let h denote the sampling period used to sample $\chi^*(t)$, and we compute the power spectrum (magnitude squared of the Fourier transform) for N equispaced samples of $\chi(t)$, then the time interval processed is $T = Nh$, and an FFT will yield

1+N/2 samples of the spectrum spaced in frequency by 1/T Hz from 0 thru 1/2h Hz. A single (sine wave) input spectral component at frequency f_o will produce an FFT spectrum output proportional to $\text{sinc}^2[(f - f_o)T]$ where

$$\text{sinc}\ (x) = \frac{\sin \pi x}{\pi x} \ . \tag{76}$$

As a function of frequency f, this function has a main lobe of width 2/T centered at f_o, surrounded by "sidelobes" of width 1/T, the first of which is 12 dB below the main lobe, with subsequent sidelobes falling off at 6 dB per octave. From this it can be seen that if the data to be spectrum analyzed contain wide fluctuations (greater than 12 dB) in spectral level, then the "sidelobes" from the strong components can mask the weaker components. To prevent this, a Hamming window is applied to the data. This is accomplished by multiplying the input to the FFT by the window function

$$w(t) = 1 - k \cos\ (2\pi t/T) \qquad 0 \le t \le T = Nh \tag{77}$$

where

k = 23/27 for Hamming window.

When this is done, a single spectral component at frequency f_o will have a spectrum with a main lobe of width 4/T (thus, poorer frequency resolution) centered at f_o, surrounded by sidelobes of width 1/T, all of which are at least 40 dB below the main lobe. Thus, use of the Hamming window prevents sidelobes from strong spectral components from masking weaker components that are no more than four orders of magnitude weaker. The cost for this is a somewhat reduced

frequency resolution. For the data analyzed in this report, frequency resolution was not a significant problem, but a large dynamic range was, so a Hamming window was used for all spectral estimates.

A.3.3.2 Zero Fill

The Fourier transform of $\chi^*(t)$ exists at all frequencies, but is evaluated by FFT routines only at frequencies spaced by 1/T Hz. Thus, interpolation is required to get a smooth curve of the spectrum versus frequency. An efficient way to accomplish this is to use zero fill. In doing this, the original N data points (weighted by the Hamming window) are followed by N_z zeros, and the FFT is applied to the resulting $(N + N_z)$-point sequence. It can be shown that the only effect this has on the spectrum is that it is evaluated every $1/(N + N_z)h$ Hz, i.e., the spacing between evaluation points is reduced by a factor of $1 + N_z/N$, producing a smoother representation of the curve. For the spectra of this report the values

$$N = 1500,$$

$$N_z = 2596,$$

$$N + N_z = 4096,$$

were used, which yield frequency points spaced by only 0.366/T Hz instead of 1/T Hz. It should be emphasized that this procedure does not improve the frequency resolution, which is determined by the Hamming window, but only interpolates to provide a smoother curve.

A.3.3.3 Spectrum Normalization

For direct comparison with the theoretical results it is necessary to maintain the correct spectral level at the output of the spectrum-analysis processing steps. This means that the effect of the Hamming window must be accounted for, as well as that care must be used in determining the appropriate normalization at the other steps.

The Hamming window is accounted for by computing the mean-squared value of the data $\chi^*(t)$ both before and after the Hamming window is applied. Then the spectral levels produced by the FFT routine are increased by the ratio of these mean-squared values. This assures that the area under the spectral curve equals the energy in the data, as is required by Parseval's theorem.

A.3.3.4 Frequency Averaging

The final step in producing the experimental spectra for this report is averaging over frequency. This step is required due to the fact that we are estimating the power spectrum of a random process (the turbulence-induced amplitude fluctuations) from one sample function of that random process, and estimates obtained this way are very noisy. For example, the standard deviations of such estimates are approximately equal to the mean spectral level. This is illustrated further in Section A.3.4. By averaging several adjacent frequency points together, the variances of the estimates are reduced, at the expense of reduced frequency resolution.

Frequency resolution is most important at the lower frequencies, since frequency is most naturally shown on a logarithmic scale for results of the type

derived here. The lowest frequency which can be shown on such a scale is equal to about half the frequency resolution. Thus, the tradeoff to be made is between accuracy of the measured spectrum and definition of the low-frequency portion of the spectrum.

The averaging done here is a "running-point" average, i.e., the spectrum at every frequency point (spaced by $1/(N + N_z)h$ Hz) is replaced by

$$\hat{G}_{AV}(f) = \frac{1}{m} \sum_{\ell=-(m-1)/2}^{(m-1)/2} \hat{G}(f + t\Delta f) \tag{78}$$

where

m = number of points (assumed odd) in running-point average,

Δf = frequency spacing from FFT,

$= 1/N + N_z)h$,

$\hat{G}(f)$ = spectrum from FFT at frequency f.

For the case m = 1, no averaging is done, and the frequency resolution is just that of the Hamming window. This is given by

$$B_w = \frac{\int_{-\infty}^{\infty} \left|F\{w(t)\}\right|^2 df}{\left|F\{w(t)\}\right|^2_{f=0}} \tag{79}$$

where F denotes the Fourier-transform operation, and

$w(t)$ = Hamming-window weighting function,

$= 1 - k \cos (2\pi t/T)$,

T = time duration of data spectrum analyzed,

$= Nh$.

The Fourier transform of $w(t)$ is

$$F\{w(t)\} = \frac{1}{\pi} e^{-j\pi Tf} \sin (\pi Tf) \left[\frac{1}{f} + \frac{kf}{(1/T^2) - f^2}\right] \tag{80}$$

so that

$$\left|F\{w(t)\}\right| = \frac{\sin (\pi Tf)}{\pi} \left[\frac{1}{f} + \frac{kf}{(1/T^2) - f^2}\right] \tag{81}$$

and

$$\lim_{f \to 0} \left| F\{w(t)\}\right| = \frac{\sin (\pi Tf)}{\pi f} \to T. \tag{82}$$

This is the square root of the denominator of the expression for B_w. The numerator is most conveniently evaluated by using Parseval's theorem, viz.,

$$\int_{-\infty}^{\infty} \left|F\{w(t)\}\right|^2 df = \int_{-\infty}^{\infty} \left|w(t)\right|^2 dt$$

$$= \int_0^T [1 - k \cos (2\pi t/T)]^2 dt$$

$$= T(1 + k^2/2). \tag{83}$$

Therefore, we have for the frequency resolution (i.e., for the bandwidth) of the Hamming window,

$$B_w = \frac{T(1 + k^2/2)}{T^2} = (1 + k^2/2)/T$$

$$= \begin{cases} [1 + (23/27)^2/2]/T = 1.363/T & \text{for the Hamming window} \\ 1/T & \text{for no window (k=0).} \end{cases} \quad (84)$$

As previously indicated, adjacent frequency points from the FFT are separated by

$$\Delta f = \frac{1}{(N + N_z)h} = \frac{1}{(1 + N_z/N)T}$$

$$= \frac{1}{(1 + 2596/1500)T} = \frac{0.366}{T} . \quad (85)$$

Therefore, when m points are averaged together the frequency resolution becomes

$$B = B_w + (m - 1)\ \Delta f$$

$$= [1.363 + 0.366\ (m - 1)]/T. \quad (86)$$

The lowest frequency point of interest (i.e., above zero frequency) after this averaging is

$$f_{min} = \frac{m+1}{2}\,\Delta f = 0.366\ (m+1)/2T$$

$$= \frac{B}{2} - \frac{0.316}{T}$$

$$\approx \frac{B}{2}\ . \tag{87}$$

A.3.4 Confidence Limits

It is shown in Ref. A6 that the spectrum estimates we obtain are approximately chi-square distributed with a number n of degrees of freedom given by (Ref. A6, eq. 6.110)

$$n = 2BT \tag{88}$$

where

B = frequency resolution,

T = time duration of data spectrum analyzed.

For our parameter values this gives

$$n = 2.726 + 0.732\ (m - 1).$$

It then follows that a 90% confidence interval is given by

$$\left(\frac{n}{\chi^2_{n;0.05}}\right)\hat{G}_{AV}(f) \le G(f) \le \left(\frac{n}{\chi^2_{n;0.95}}\right)\hat{G}_{AV}(f) \tag{89}$$

where

$\hat{G}_{AV}(f)$ = spectrum estimated from running-point average,

$G(f)$ = true spectrum,

$\chi^2_{n;\alpha}$ = percentage points of the chi-square distribution.

Values of $\chi^2_{n;\alpha}$ for integer n are tabulated in Table A.3 of Ref. A6. These were used to tabulate the 90% confidence intervals shown here in Table A-1.

From that table it can be seen that without averaging, the 90% confidence interval is

$$0.38\ \hat{G}_{AV}(f) \leq G(f) \leq 8.5\ \hat{G}_{AV}(f)$$

which is a very wide interval. When a 51-point average is used this interval is reduced to

$$0.72\ \hat{G}_{AV}(f) \leq G(f) \leq 1.5\ \hat{G}_{AV}(f)$$

which corresponds to a much more useful estimation accuracy.

A.4 SUMMARY OF PROCESSING STEPS

In this Section we will summarize the processing steps required to produce the experimental spectra shown in this report.

A.4.1 Filtering and Decimation

The data processed for this report had previously been received, recorded, and digitized for the original Mariner V occultation experiment (Ref. A7). Thus, the first step to be taken here is to filter and decimate the data (Section A.1.4). This requires selection of a spline curve to follow the gross frequency-versus-time

profile of the received signal, and a choice of bandwidth Δ and decimation factor N. The spline curve had been previously developed, as described in Ref. A8. The bandwidth Δ must be chosen large enough to pass the signal frequency variations after being shifted by the spline curve, and the decimation factor N must correspond to Δ. For the processing carried out here, N = 101 was found to be a convenient value.

A.4.2 PLL Tracking

The main parameters to be chosen for the phase-locked-loop tracking (Section A.2) are the loop bandwidth B_L, the damping R, the AGC time constant τ_{AGC}, and the output sampling period h. The bandwidth must satisfy

$$\sqrt{R} < B_L < \frac{A^2}{10\ N_0} \tag{90}$$

where

R = signal's frequency rate (Hz/sec),

A = signal rms amplitude,

N_0 = noise one-sided spectral density (watts/Hz).

The choice of damping R is not critical, and here was taken to be 2 (see Fig. A-4).

The time constant τ_{AGC} is one of the more critical processing constants (Sections A.2.5 and A.2.6), because it determines the maximum frequency at which amplitude fluctuations may be observed. For good performance it must satisfy

$$\tau_{AGC} \geq 6.24\ N_0/A^2. \tag{91}$$

Also, it must satisfy

$$\frac{1}{2\pi f_{max}} < \tau_{AGC} \tag{92}$$

where

f_{max} = maximum frequency of turbulence.

One other consideration in the choice of τ_{AGC} is that it indirectly determines the lowest frequency component that can be measured. This is because the lowest frequency component measured is (Section A.3.3.4)

$$f_{min} = \frac{0.366\ (m + 1)}{2T} \tag{93}$$

where

m = number of points in running-point average,

T = Nh,

N = number of data points in input to FFT,

= 1500,

h = sampling period,

$\leq \tau_{AGC}$.

Thus, for fixed values of the other parameters, the minimum frequency f_{min} is limited by the choice of τ_{AGC}.

A.4.3 Spectrum Analysis

The spectrum analysis step consists of fitting a quadratic function of time to the data for use in detrending it, computing the FFT of the Hamming-windowed

data, and smoothing the result by the running-point average. The only parameter to be chosen here is the number m of points over which to compute the average. In practice several values of m are used, usually ranging from one to 51.

A.4.4 Interpretation of Results

The last step in the processing consists of using the theoretical results of this report to separate the turbulence-induced fluctuations from the noise-induced fluctuations. The noise is recognized (see Section A.2.5.2) by having the spectral shape shown in Fig. A-8 and a level given by $75.4\ N_0/A^2$ for $a^*(t)$, and by N_0/A^2 for $\chi^*(t)$, where $a^*(t)$ is the estimated amplitude in dB, and $\chi^*(t)$ is the natural logarithm of the estimated amplitude. The part of the experimental spectrum which deviates from this noise part is then interpreted in terms of turbulence-induced phenomena.

REFERENCES

A1. Tausworth, R.C., "Theory and Practical Design of Phase-Locked Receivers," Vol. I, Jet Propulsion Laboratory, Pasadena, Calif., Technical Report No. 32-819, Feb. 15, 1966.

A2. Viterbi, A.J., Principles of Coherent Communication, McGraw-Hill, New York, 1966.

A3. Gardner, F.M., Phaselock Techniques, John Wiley, New York, 1966.

A4. Victor, W.K., and M.H. Brockman, "The Application of Linear Servo Theory to the Design of AGC Loops", Proc. IRE, Vol. 48, No. 2, pp 234-238, Feb. 1960.

A5. Davenport, W.B., and W.L. Root, An Introduction to the Theory of Random Signals and Noise, McGraw Hill, New York, 1958, p. 255, Eqns. (12-24a) through (12-26b).

A6. Bendat, J.S., and A.G. Piersol, Random Data: Analysis and Measurement Procedures., Wiley-Interscience, New York., 1971.

A7. Kliore, A., G.S. Levy, D.L. Cain, G. Fjeldbo, and S.I. Rasool, "Atmosphere and Ionosphere of Venus from Mariner V S-Band Radio Occultation Measurement," Science, Vol. 158, pp 1683-1688, Dec. 29, 1967.

A8. Kendall, W.B., "Digital Processing of the Mariner-V Occultation Data," Jet Propulsion Lab., Pasadena, Calif., Space Programs Summary 37-50, Vol. 2, pp 80-86, March 1968.

m No. of Freq. Points Averaged	n = 2BT Degrees of Freedom	Nearest Integer in Table A.3 of Ref. A6	$\frac{n}{\chi^2_{n;0.05}}$	$\frac{n}{\chi^2_{n;0.95}}$
1	2.73	3	0.38	8.5
11	10.05	10	0.55	2.5
21	17.38	17	0.62	2.0
31	24.70	25	0.66	1.7
41	32.03	30	0.68	1.6
51	39.35	40	0.72	1.5

Table A-1. 90% Confidence Intervals for Averaged Spectrum Estimates

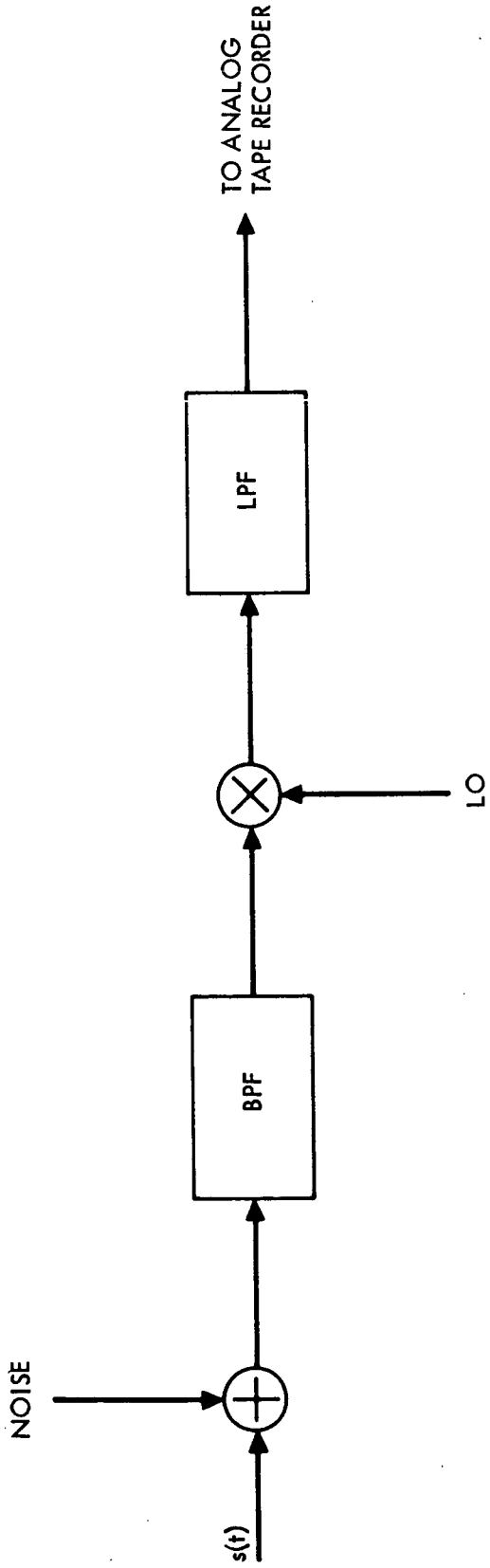

Fig. A-1. Simplified Receiver Block Diagram

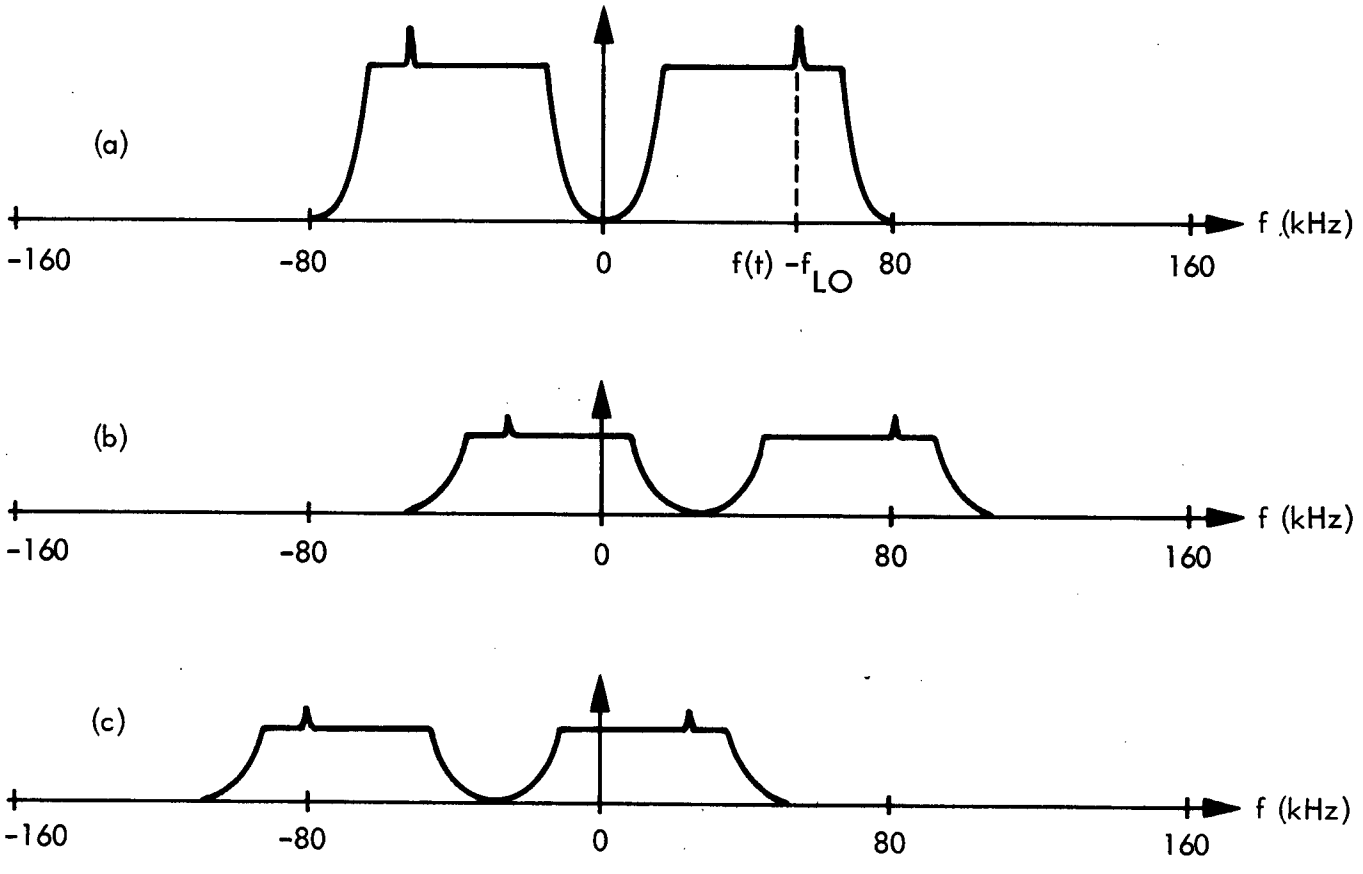

Fig. A-2. Spectra of r(t). (a) Original (b) Upshifted (c) Downshifted

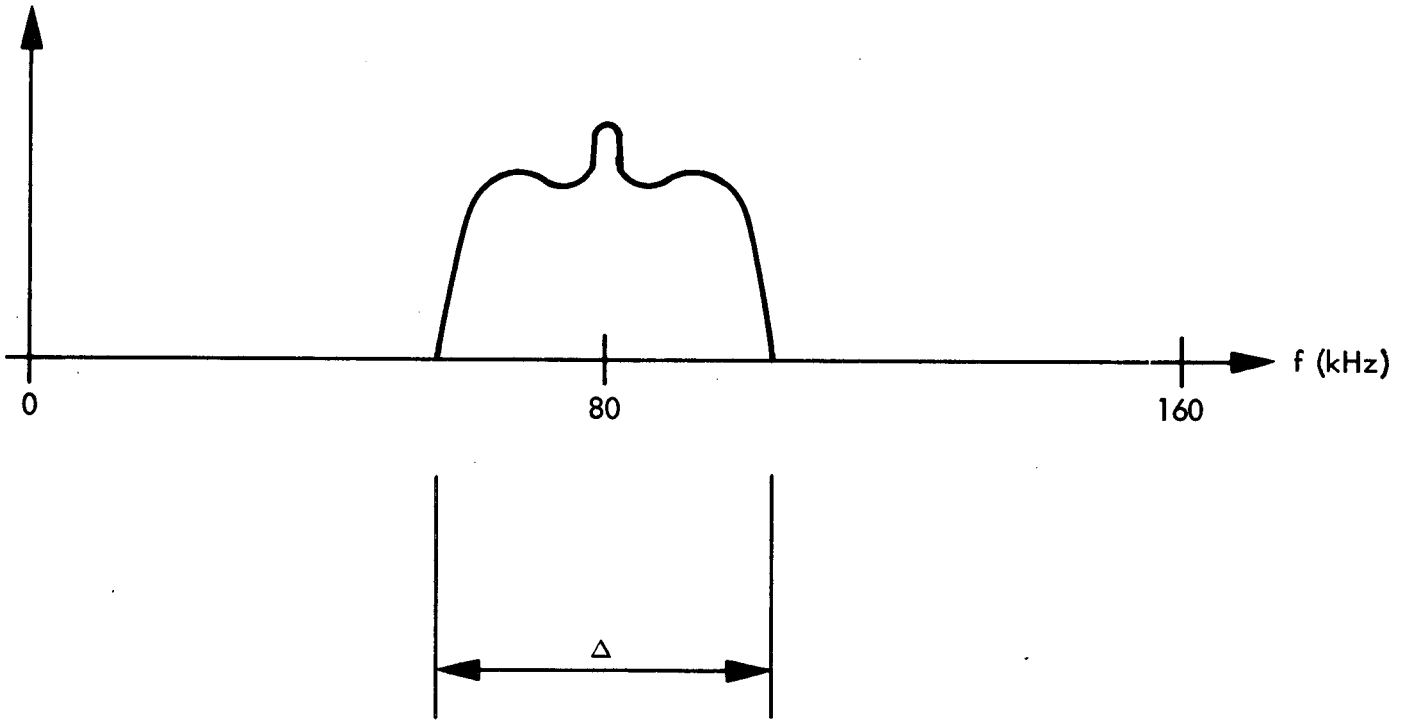

Fig. A-3. Positive-Frequency Spectrum of r(t) after Frequency Shifting and Band Limiting

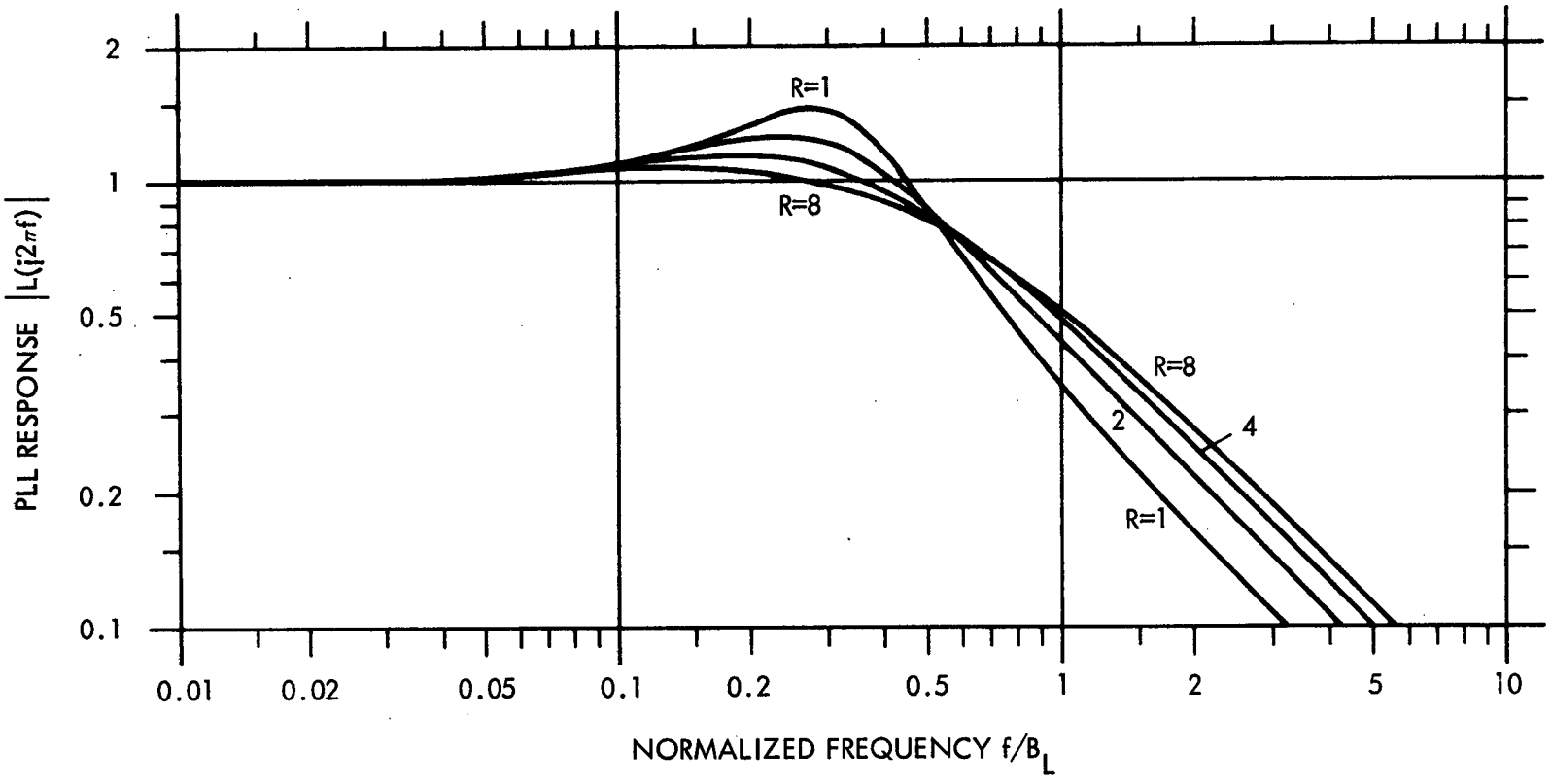

Fig. A-4a. Response of PLL to Phase Modulation at Frequency f

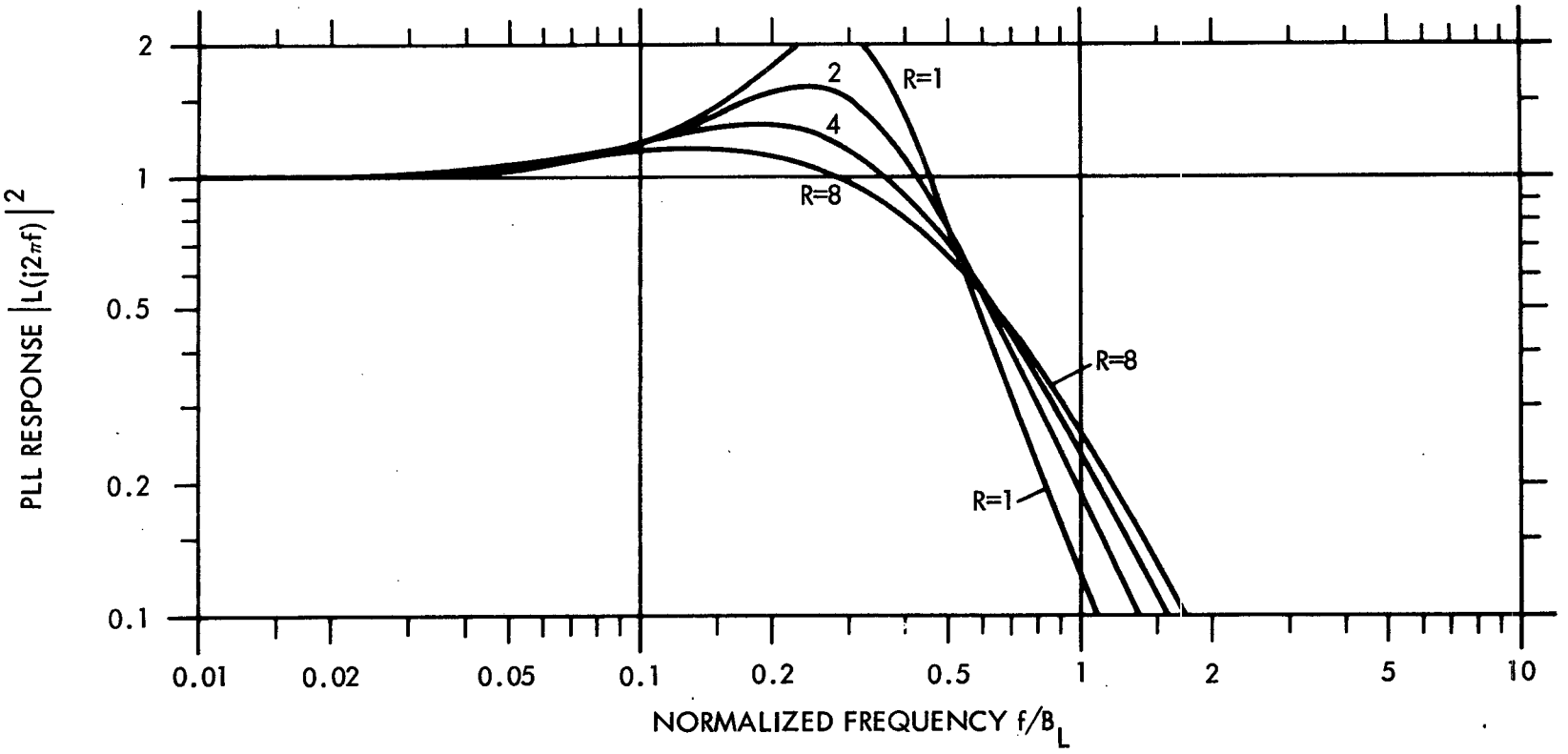

Fig. A-4b. Spectral Response of PLL to Phase Modulation at Frequency f

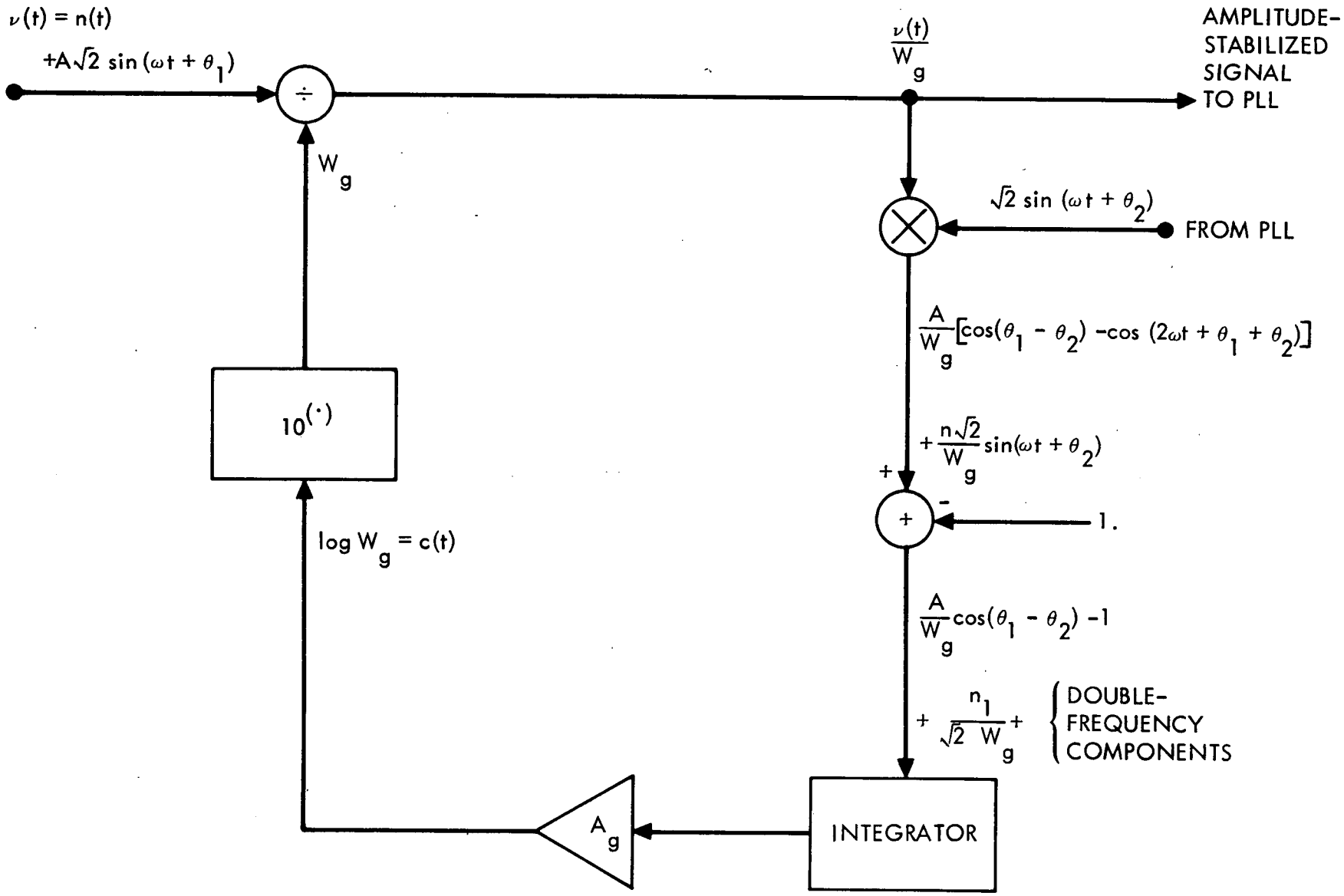

Fig. A-5. Block Diagram of the Coherent Amplitude Estimating and AGC Computer Program

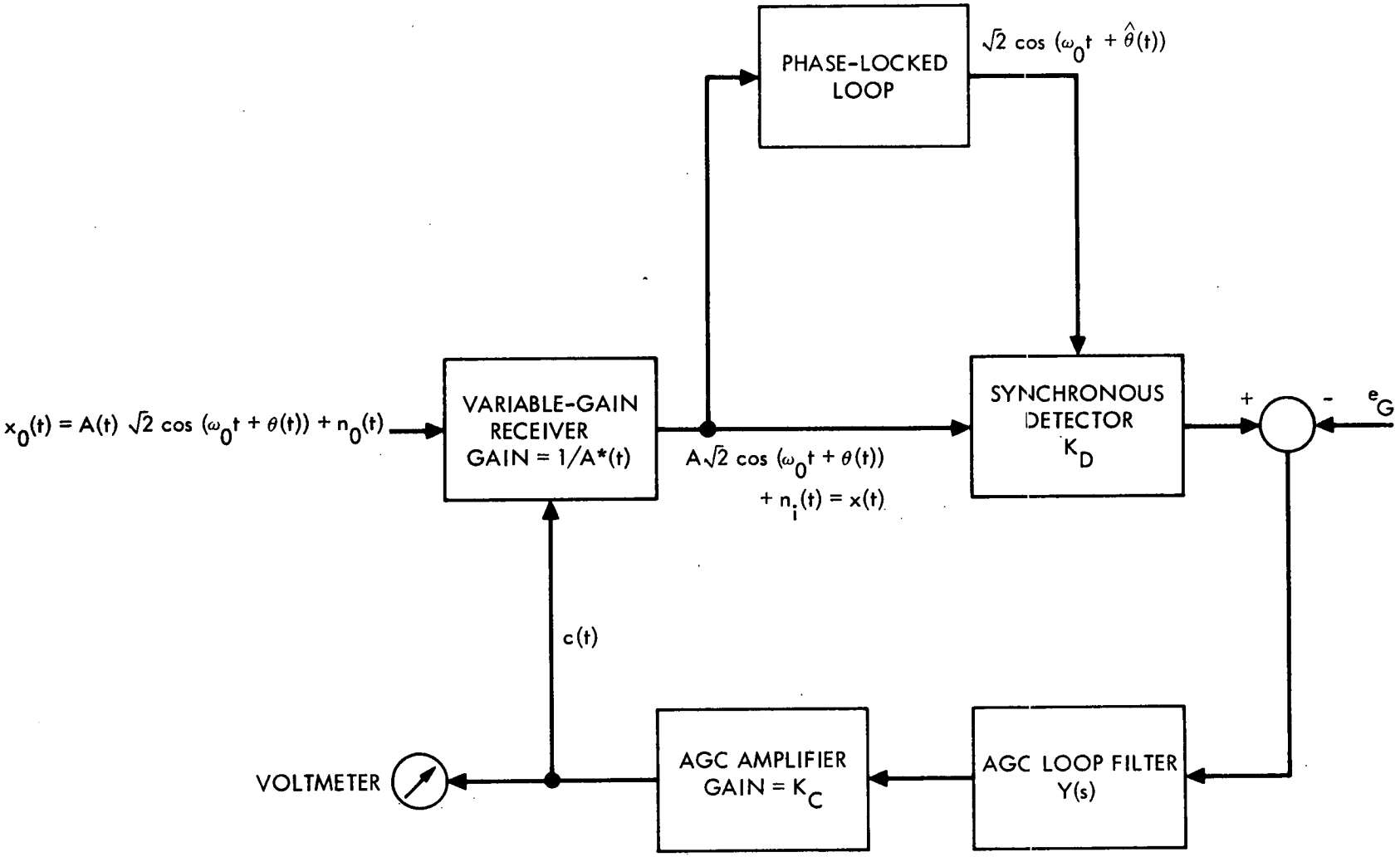

Fig. A-6. Block Diagram of the AGC Loop Analyzed by Tausworthe. Taken from Fig. 7-1 of Ref. A1

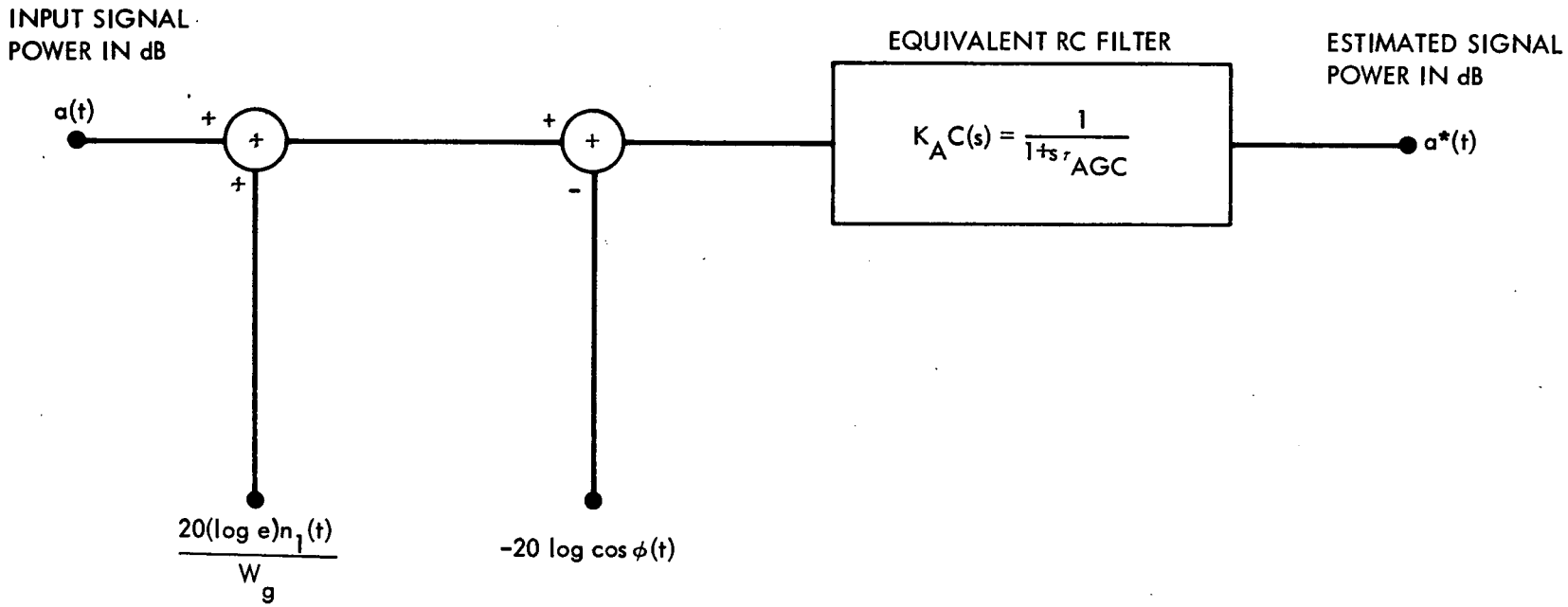

Fig. A-7. Equivalent Block Diagram for the Linearized AGC Loop

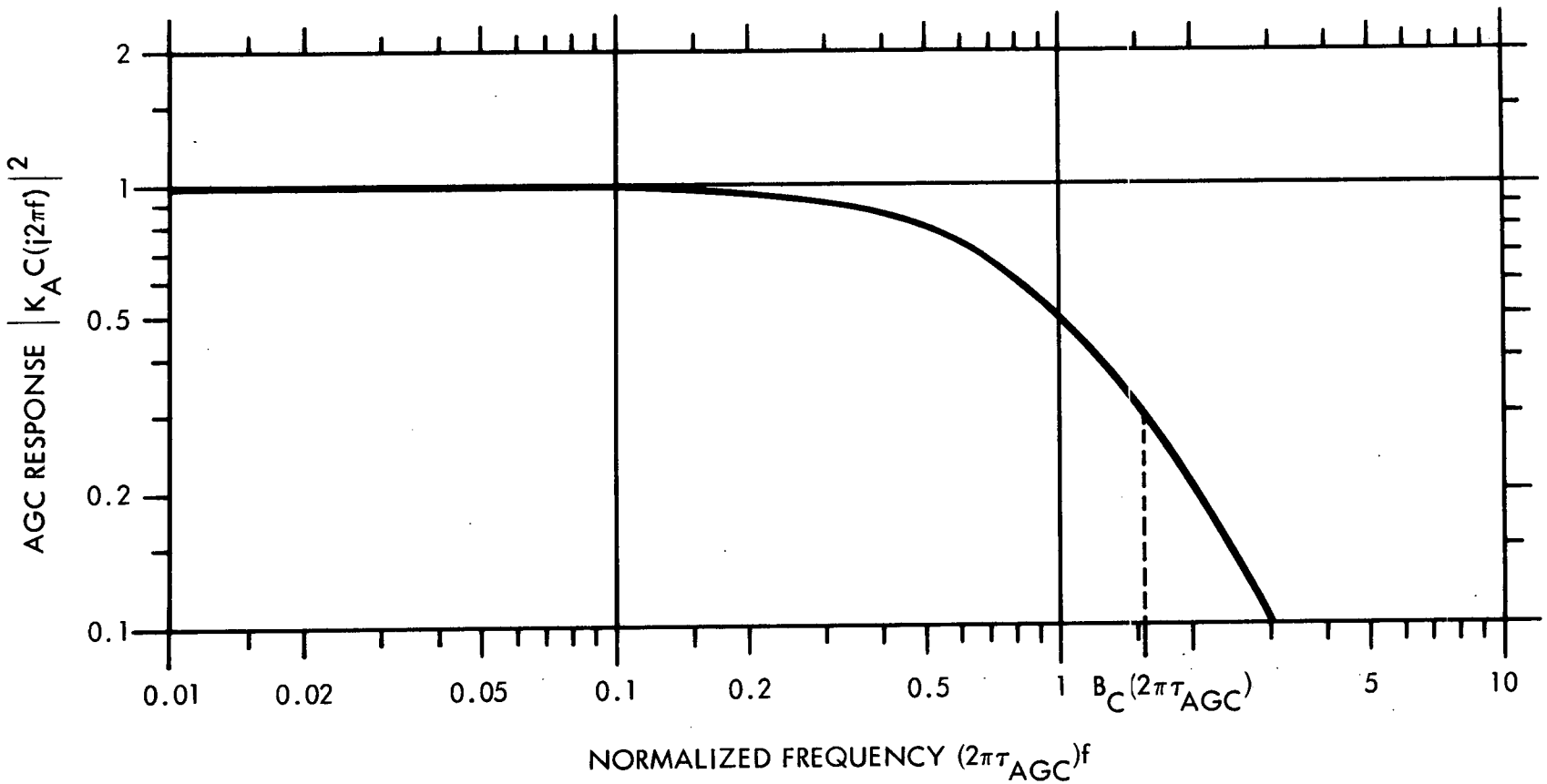

Fig. A-8. Spectral Response of AGC to Amplitude Modulation at Frequency f

APPENDIX B

CONTENTS

APPENDIX B

EFFECTS OF ATMOSPHERIC TURBULENCE ON THE RADIO SIGNAL OF A FLY-BY SPACE PROBE

B.1 Formulation of the General Problem

Let us consider both plane and spherical wave propagation with the respective configurations depicted in Figs. B-1 and B-2. The direction of wave propagation is assumed to be along the x axis and the turbulence medium characterized by the refractive index

$$n(\vec{r}, t) = 1 + n_1(\vec{r}, t) \tag{1}$$

where $n_1(\vec{r}, t)$ is the fluctuation and assumed small, r is position and t time.

According to Rytov's method (Refs. B1 and B2) the field U at the observation point $(L, \vec{\rho})$ at time t is given approximately by

$$U(L, \vec{\rho}, t) = U_o(L, \vec{\rho}) \exp [\psi_1(L, \vec{\rho}, t)] \tag{2}$$

$$\psi_1(L, \vec{\rho}, t) = \int_o^L dx' \iint_{-\infty}^{\infty} d\vec{\rho}' h(L, x', \vec{\rho}' - \gamma\vec{\rho}) \, n_1(x, \vec{\rho}', t) \tag{3}$$

where

$$h(L, x', \vec{\rho}') = \frac{k^2}{2\pi} \frac{1}{\gamma(L - x')} \exp \left[i \frac{k}{2} \frac{\vec{\rho}' \cdot \vec{\rho}'}{\gamma(L - x')} \right]$$

$\gamma = 1$ for a plane wave

$\gamma = \frac{x'}{L}$ for a spherical wave

$\vec{\rho} = y\,\hat{y} + z\,\hat{z}$, $\hat{y}$ and $\hat{z}$ are unit vectors in the y and z directions, $\vec{\rho}' = y'\,\hat{y} + z'\,\hat{z}$, k is the free space wavenumber and U_o is the field in free space (without turbulence). Also,

$$\psi_1(L, \vec{\rho}, t) = \chi(L, \vec{\rho}, t) + i\, S_1(L, \vec{\rho}, t) \tag{4}$$

where χ is the log-amplitude fluctuation and S_1 is the phase fluctuation.

Under Taylor's frozen-in hypothesis

$$n_1(\vec{r}, t) = n_1(\vec{r} - \vec{v}t, 0) \tag{5}$$

where $\vec{v}$ is the average wind velocity perpendicular to the direction of wave propagation. Inherent in (5) is the assumption that the effect of wind velocity fluctuations is small compared to the average wind velocity $\vec{v}$. Applying Taylor's frozen-in hypothesis to (3), we have

$$\psi_1(L, \vec{\rho}, t) = \int_0^L dx' \int_{-\infty}^{\infty}\int d\vec{\rho}''\; h[L, x', \vec{\rho}'' - (\gamma\vec{\rho} - \vec{v}t)]\; n_1(x, \vec{\rho}'', 0) \tag{6}$$

where the coordinate $\vec{\rho}'' = \vec{\rho}' - \vec{v}t$ is attached to the moving turbulence. n_1 in (6) is a function of position only and the usual time-independent spectral representation for n_1 may be used.

We will assume that the turbulence is described by a random process studied by Silverman (Ref. B3) and employed in previous turbulence studies (Refs. B4 and B5). The correlation function for the refractive index fluctuation $B_n(\vec{r}_1, \vec{r}_2)$ is given as a product of the average coordinate and a function of the difference coordinate, i.e.

$$B_n(\vec{r}_1, \vec{r}_2) = B_n^v(\vec{r}_c)\; B_n^o(\vec{r}_d) \tag{7}$$

where $\vec{r}_c = \frac{1}{2}(\vec{r}_1 + \vec{r}_2)$ and $\vec{r}_d = \vec{r}_1 - \vec{r}_2$. The corresponding spectrum $\Phi_n(\vec{K}_1, \vec{K}_2)$ is then a product of a function of the average wavenumber and a function of the difference wavenumber, i.e.

$$\Phi_n(\vec{K}_1, \vec{K}_2) = \Phi_n^v(\vec{K}_d)\ \Phi_n^o(\vec{K}_c) \tag{8}$$

where $\vec{K}_c = \frac{1}{2}(\vec{K}_1 + \vec{K}_2)$ is the average wavenumber and $\vec{K}_d = \vec{K}_1 - \vec{K}_2$ is the difference wavenumber. B_n^v and B_n^o are related to Φ_n^v and Φ_n^o through the following Fourier transforms

$$B_n^v(\vec{r}_c) = \int_{-\infty}^{\infty}\int\int \exp(i\,\vec{K}_d \cdot \vec{r}_c)\ \Phi_n^v(\vec{K}_d)\ d\vec{K}_d \tag{9}$$

$$B_n^o(\vec{r}_d) = \int_{-\infty}^{\infty}\int\int \exp(i\,\vec{K}_c \cdot \vec{r}_d)\ \Phi_n^o(\vec{K}_c)\ d\vec{K}_c \tag{10}$$

Since the wave is propagating in the x direction we need use the spectral representation in the y-z plane only. We then have

$$B_n^v(x_c, \vec{\rho}_c) = \int_{-\infty}^{\infty}\int \exp(i\,\vec{\kappa}_d \cdot \vec{\rho}_c)\ F_n^v(x_c, \vec{\kappa}_d)\ d\vec{\kappa}_d \tag{11}$$

$$B_n^o(x_d, \vec{\rho}_d) = \int_{-\infty}^{\infty}\int \exp(i\,\vec{\kappa}_c \cdot \vec{\rho}_d)\ F_n^o(x_d, \vec{\kappa}_c)\ d\vec{\kappa}_c \tag{12}$$

and the two dimensional spectra F_n^v and F_n^o are related to the three dimensional spectra Φ_n^v and Φ_n^o by

$$F_n^v(x_c, \vec{\kappa}_d) = \int_{-\infty}^{\infty} \exp(i K_{d1} x_c)\ \Phi_n^v(K_{d1}, \vec{\kappa}_d)\ dK_{d1} \tag{13}$$

$$F_n^o(x_d, \vec{\kappa}_c) = \int_{-\infty}^{\infty} \exp(i K_{c1} x_d)\ \Phi_n^o(K_{c1}, \vec{\kappa}_c)\ dK_{c1} \tag{14}$$

where $\vec{K}_c = K_{c1}\hat{x} + K_{c2}\hat{y} + K_{c3}\hat{z} = K_{c1}\hat{x} + \vec{\kappa}_c$, $\vec{K}_d = K_{d1}\hat{x} + K_{d2}\hat{y} + K_{d3}\hat{z}$ $= K_{d1}\hat{x} + \vec{\kappa}_d$, $\vec{\rho}_c = (\vec{\rho}_1 + \vec{\rho}_2)/2$, $\vec{\rho}_d = \vec{\rho}_1 - \vec{\rho}_2$, $x_c = (x_1 + x_2)/2$ and $x_d = x_1 - x_2$. We will assume that the turbulence is isotropic so that the correlation function $B_n^o(\vec{r}_d)$ is a function of the magnitude of $\vec{r}_d$ only and (Ref. B4)

$$\frac{1}{2\pi} \int_{-\infty}^{\infty} F_n^o(x_d, \vec{\kappa}_c)\ dx_d = \Phi_n^o(0, \vec{\kappa}_c) = \Phi_n^o(\kappa_c) \tag{15}$$

The correlation functions for the log-amplitude and phase fluctuations, B_χ and B_s, are

$$B_\chi(L, \vec{\rho}_c, \vec{\rho}_d, t_c, \tau) = \langle \chi(L, \vec{\rho}_1, t_1)\ \chi(L, \vec{\rho}_2, t_2) \rangle \tag{16}$$

$$B_s(L, \vec{\rho}_c, \vec{\rho}_d, t_c, \tau) = \langle S_1(L, \vec{\rho}_1, t_1)\ S_1(L, \vec{\rho}_2, t_2) \rangle \tag{17}$$

where $t_c = (t_1 + t_2)/2$ and $\tau = t_1 - t_2$. Following a procedure similar to that in Ref. B4, we can obtain (16) and (17) from (4) and (6) for the turbulent medium described above. Let us first look at the case of log-amplitude fluctuations. We will assume that the observation distance is large compared to x_d and obtain the following results:

$$B_\chi(L, \vec{\rho}_c, \vec{\rho}_d, t_c, \tau) = 2\pi k^2 \int_0^L dx_c \frac{1}{(2\pi)^2} \iint_{-\infty}^{\infty} d\vec{\rho}_c'' \, B_n^v(x_c, \vec{\rho}_c'')$$

$$\cdot G_\chi(x_c, \gamma\vec{\rho}_c - \vec{v}t_c - \vec{\rho}_c'', \gamma\vec{\rho}_d - \vec{v}\tau) \tag{18}$$

where

$$G_\chi(x_c, \vec{\rho}_c, \vec{\rho}_d) = \int_{-\infty}^{\infty}\int d\vec{\kappa}_d \exp(i\,\vec{\kappa}_d \cdot \vec{\rho}_c)$$

$$\cdot \int_{-\infty}^{\infty}\int d\vec{\kappa}_c \exp(i\,\vec{\kappa}_c \cdot \vec{\rho}_d)\, S_\chi(x_c, \vec{\kappa}_c, \vec{\kappa}_d)\, \Phi_n^o(\kappa_c) \tag{19}$$

$$S_\chi(x_c, \vec{\kappa}_c, \vec{\kappa}_d) = \frac{1}{4}\left\{\exp(i\,A\,\vec{\kappa}_c \cdot \vec{\kappa}_d) + \exp(-i\,A\,\vec{\kappa}_c \cdot \vec{\kappa}_d)\right.$$

$$\left. - \exp\left[i\,A\left(\kappa_c^2 + \frac{\kappa_d^2}{4}\right)\right] - \exp\left[-i\,A\left(\kappa_c^2 + \frac{\kappa_d^2}{4}\right)\right]\right\} \tag{20}$$

and

$$A = \frac{\gamma(L - x_c)}{k}\,.$$

We note that $B_n^v(x_c, \vec{\rho}_c'')$ is measured in the coordinate system $\vec{\rho}_c''$ which is moving with velocity $\vec{v}$, i.e., $\vec{\rho}_c'' = \vec{\rho}_c' - \vec{v}t_c$ where $\vec{\rho}_c'$ is the actual position of the turbulence at t_c. We can transform (18) into an integral with respect to the actual coordinate $\vec{\rho}_c'$ and obtain:

$$B_\chi(L, \vec{\rho}_c, \vec{\rho}_d, t_c, \tau) = 2\pi k^2 \int_0^L dx_c \frac{1}{(2\pi)^2} \int_{-\infty}^{\infty}\int d\vec{\rho}_c' \, B_n^v(x_c, \vec{\rho}_c' - \vec{v}t_c)$$

$$\cdot \, G_\chi(x_c, \gamma\vec{\rho}_c - \vec{\rho}_c', \gamma\vec{\rho}_d - \vec{v}\tau) \tag{21}$$

It should be pointed out that (21) can also be written as an integral in terms of the two wavenumbers $\vec{\kappa}_c$ and $\vec{\kappa}_d$ as was done in Ref. B4.

Similarly, for phase, we have

$$B_S(L, \vec{\rho}_c, \vec{\rho}_d, t_c, \tau) = 2\pi k^2 \int_0^L dx_c \frac{1}{(2\pi)^2} \int_{-\infty}^{\infty}\int d\vec{\rho}_c' \, B_n^v(x_c, \vec{\rho}_c' - \vec{v}t_c)$$

$$\cdot \, G_S(x_c, \gamma\vec{\rho}_c - \vec{\rho}_c', \gamma\vec{\rho}_d - \vec{v}\tau) \tag{22}$$

where G_S is the same as (19) except for S_χ which is replaced by S_S and

$$S_S(x_c, \vec{\kappa}_d, \vec{\kappa}_c) = \frac{1}{4}\left\{\exp(iA\vec{\kappa}_c \cdot \vec{\kappa}_d) + \exp(-iA\vec{\kappa}_c \cdot \vec{\kappa}_d) + \exp\left[iA\left(\kappa_c^2 + \frac{\kappa_d^2}{4}\right)\right]\right.$$

$$\left. + \exp\left[-iA\left(\kappa_c^2 + \frac{\kappa_d^2}{4}\right)\right]\right\} \tag{23}$$

The variances of the log-amplitude and phase fluctuations σ_χ^2 and σ_S^2 respectively along with the frequency spectra of the log amplitude and phase fluctuations W_χ and W_S respectively may now be derived in terms of the corresponding correlation functions (18) and (22). Since we are interested in the signal at one location and at one time, $\vec{\rho}_d = 0$ and $\tau = 0$.

$$\sigma_\chi^2(L,\vec{\rho}_c,t_c) = B_\chi(L,\ \rho_c,\ 0,\ t_c,\ 0) \tag{24}$$

$$\sigma_S^2(L,\ \vec{\rho}_c,t_c) = B_S(L,\ \rho_c,\ 0,\ t_c,\ 0) \tag{25}$$

and

$$W_\chi(L,\vec{\rho}_c,0,t_c,f) = W_\chi(L,\ \vec{\rho}_c,\ t_c,\ f) = 2\int_{-\infty}^{\infty} B_\chi(L,\ \vec{\rho}_c,\ 0,\ t_c,\ \tau)e^{-i\omega\tau}d\tau \tag{26}$$

$$W_S(L,\vec{\rho}_c,\ 0,t_c,f) = W_S(L,\ \vec{\rho}_c,\ t_c,\ f) = 2\int_{-\infty}^{\infty} B_S(L,\ \vec{\rho}_c,\ 0,\ t_c,\ \tau)e^{-i\omega\tau}d\tau \tag{27}$$

where $\omega = 2\pi f$ and f is the fluctuation frequency. We will evaluate and discuss (24)-(27) in the following sections.

B.2 Theoretical Variances of Log-amplitude and Phase Fluctuations

As in a previous study (Ref. B5) we will assume that the Venusian atmospheric turbulence is localized and smoothly varying so that its correlation function can be written

$$B_n(\vec{r}_1,\ \vec{r}_2) = 0.033\ c_n^2(\vec{r}_c)\ B_n^o(|\vec{r}_d|) \tag{28}$$

where the structure constant c_n characterizes the intensity of turbulence and is slowly varying. Comparing (28) with (7) we observe that $B_n(\vec{r}_c) = 0.033\, c_n^2(\vec{r}_c)$. We will also employ the von Kármán representation of the Kolmogorov spectrum to describe the localized homogeneous and isotropic turbulence, i.e.

$$\Phi_n^o(\kappa_c) = \left(\kappa_c^2 + \frac{1}{L_o^2}\right)^{-11/6} \tag{29}$$

which is of course related to $B_n^o(|\vec{r}_d|)$ through (10), (14) and (15).

Using this turbulence description, G_χ in (18) can be integrated so that (24) and (25) become (Ref. B5)

$$\sigma_\chi^2(L,\vec{\rho}_c,t_c) = 0.033\,\frac{k^2}{2\pi}\int_0^L dx_c \int_{-\infty}^{\infty}\int d\vec{\rho}_c''\, c_n^2(x_c, \vec{\rho}_c'' - \vec{v}t_c)$$

$$\cdot\left\{\left(\frac{2\pi^2}{A^2}\right)\left(\frac{\rho_c^2}{A^2} + \frac{1}{L_o^2}\right)^{-11/6}\right.$$

$$\left. - \mathrm{Re}\left[\left(\frac{2\pi^2}{-iA}\right)\exp\left(-i\,\frac{\rho_c^2}{A}\right)L_o^{5/3}\,\psi\left(1, \frac{1}{6}; -i\,\frac{A}{L_o^2}\right)\right]\right\} \tag{30}$$

and

$$\sigma_S^2(L,\vec{\rho}_c,t_c) = 0.033\,\frac{k^2}{2\pi}\int_0^L dx_c \int_{-\infty}^{\infty}\int d\vec{\rho}_c''\, B_n^v(x_c, \vec{\rho}_c'' - \vec{v}t_c)$$

$$\cdot\left\{\left(\frac{2\pi^2}{A^2}\right)\left(\frac{\rho_c^2}{A^2} + \frac{1}{L_o^2}\right)^{-11/6}\right.$$

$$+ \operatorname{Re}\left[\left(\frac{2\pi^2}{-iA}\right)\exp\left(-i\frac{\rho_c^2}{A}\right) L_o^{5/3}\,\psi\left(1, \frac{1}{6}; -i\frac{A}{L_o^2}\right)\right]\Bigg\} \qquad (31)$$

where Re [ ] means real part of [ ] and $\psi(a,c;z)$ is the confluent hypergeometric function (Ref. B6).

As discussed in the main text (Section 4.2) we will choose the following model for c_n^2

$$c_n^2(\vec{r}_c) = c_n^2(x_c,y_c,z_c) = c_{no}^2 \exp -\left[\left(\frac{x_c - L}{a}\right)^2 - \left(\frac{y_c}{b}\right)^2 - \left(\frac{z_c}{a}\right)^2\right] \qquad (32)$$

where $c_{no}^2 = c_n^2(0,0,0)$ is the peak structure constant and the coordinate system and occultation geometry are shown in Fig. B-3.

It is obvious that the moving spacecraft results in a sweeping motion of the line-of-sight through the turbulent atmosphere and that this motion has the same effect on the radio signal as the wind. Also, since the velocity of this sweeping motion is considerably larger than the wind velocity in the Venusian atmosphere, $\vec{v}$ essentially represents the velocity of the sweeping motion and is oriented in the y_c-direction. It can therefore be seen that this study does take into account the effect of the spacecraft velocity.

Applying (30) and (31) to the configuration in Fig. B-3 we have at the observation point located on earth

$$\left.\begin{matrix}\sigma_\chi^2 \\ \sigma_S^2\end{matrix}\right\} = 0.033\,\frac{k^2}{2\pi}\int_0^{L'} dx_c \int_{-\infty}^{\infty}\int dy_c\, dz_c\, c_n^2(x_c, y_c - vt_c, z_c) \left\{\begin{matrix}G_x(x_c,y_c,z_c) \\ G_S(x_c,y_c,z_c)\end{matrix}\right\} \qquad (33)$$

where

$$G_X = G_{X1} - G_{X2}$$

$$G_S = G_{X1} + G_{X2}$$

$$G_{X1} = \left(\frac{2\pi^2}{A^2}\right)\left(\frac{y_c^2 + z_c^2}{A^2} + \frac{1}{L_o^2}\right)^{-11/6} \tag{34}$$

$$G_{X2} = \mathrm{Re}\left[\left(\frac{2\pi^2}{-iA}\right) e^{-i\left(\frac{y_c^2 + z_c^2}{A}\right)} L_o^{5/3}\, \psi\left(1, \frac{1}{6}\,;\, -i\,\frac{A}{L_o^2}\right)\right] \tag{35}$$

$$A = \frac{x_c(L' - x_c)}{kL'}$$

and v the velocity of the sweeping motion of the line-of-sight is assumed to be in the y_c direction. We note that A can be alternately written

$$\frac{x_c L''}{k(L + L'')}$$

and since $L'' >> L$, A can be approximated by x_c/k. Furthermore

$$\int_{-\infty}^{\infty} dy_c \exp\left[-\left(\frac{y_c - vt_c}{b}\right)^2 - i\,\frac{y_c^2}{A}\right]$$

$$= \frac{\sqrt{\pi}}{\sqrt{\frac{1}{b^2} + \frac{i}{A}}} \exp\left[\left(\frac{2vt_c}{b^2}\right)^2 \frac{1}{4\left(\frac{1}{b^2} + \frac{i}{A}\right)} - \frac{v^2 t_c^2}{b^2}\right] \tag{36}$$

and when L >> a

$$\int_{-\infty}^{\infty} f(x_c) \exp\left[-\left(\frac{x_c - L}{a}\right)^2\right] dx_c \cong \sqrt{\pi}\, a\, f(L) \tag{37}$$

It can then be shown that (33) becomes

$$\sigma_\chi^2 = 0.033 \frac{k^2}{2\pi} \sqrt{\pi}\, a\, c_{no}^2 (I_1 + I_2) \tag{38}$$

$$\sigma_S^2 = 0.033 \frac{k^2}{2\pi} \sqrt{\pi}\, a\, c_{no}^2 (I_1 - I_2) \tag{39}$$

where

$$I_1 = \frac{2\pi^2}{A^2} \int_{-\infty}^{\infty}\int dy_c\, dz_c \left(\frac{y_c^2 + z_c^2}{A^2} + \frac{1}{L_o^2}\right)^{-11/6} \exp\left[-\left(\frac{y_c - vt_c}{b}\right)^2 - \left(\frac{z_c}{a}\right)^2\right] \tag{40}$$

$$I_2 = -\mathrm{Re}\left\{\left(\frac{2\pi}{-iA}\right) L_o^{5/3}\, \psi\left(1, \frac{1}{6}; -i\frac{A}{L_o^2}\right) \frac{\pi}{\sqrt{\frac{1}{a^2} + \frac{i}{A}}\sqrt{\frac{1}{b^2} + \frac{i}{A}}} \exp\left[\left(\frac{2vt_c}{b^2}\right)\frac{1}{4\left(\frac{1}{b^2} + \frac{i}{A}\right)} - \frac{v^2 t_c^2}{b^2}\right]\right\} \tag{41}$$

As shown in Ref. B5, (38)-(41) can be evaluated for various ranges of L. In this report we will be interested only in the first three regions which are shown in Fig. B-4.

Region I: $A = \frac{L}{k} << L_o^2 << L_o b << L_o a << b^2 << a^2$

We will assume that $A/L_o << vt_c$, so that

$$I_1 = \frac{2\pi^2}{A} \int_{-\infty}^{\infty} dy_c \int_{-\infty}^{\infty} dz_c \left(\frac{y_c^2 + z_c^2}{A^2} + \frac{1}{L_o^2} \right)^{-11/6} \exp \left[- \left(\frac{vt_c}{b} \right)^2 \right] \tag{42}$$

$$= \frac{12}{5} \pi^3 L_o^{5/3} \exp \left[- \left(\frac{vt_c}{b} \right)^2 \right] \tag{43}$$

Also, using the small argument approximation for ψ (Ref. B6)

$$\psi \left(1, \frac{1}{6} ; x \right) \simeq \frac{6}{5} + \Gamma \left(- \frac{5}{6} \right) x^{5/6} \tag{44}$$

where Γ is the Gamma function, we have

$$I_2 = - 2\pi^2 L_o^{5/3} \pi \left[\frac{6}{5} + \Gamma \left(- \frac{5}{6} \right) \cos \left(\frac{5\pi}{12} \right) \frac{A^{5/6}}{L_o^{5/3}} \right] \exp \left[- \left(\frac{vt_c}{b} \right)^2 \right] \tag{45}$$

so that

$$\sigma_\chi^2 = 0.997 \, k^{7/6} L^{5/6} a \, c_{no}^2 \exp \left[- \left(\frac{vt_c}{b} \right)^2 \right] \tag{46}$$

$$\sigma_S^2 = \left(1.385\ k^2\ L_o^{5/3}\ a\ c_{no}^2 - \sigma_x^2\right)\ \exp\left[-\left(\frac{vt_c}{b}\right)^2\right] \tag{47}$$

where σ_χ^2 in (47) is just (46)

Region II: $\quad L_o^2 << A << L_o b << L_o a << b^2 << a^2$

In this region I_1 is the same as (46) while for I_2 we use the large argument approximation for ψ (Ref. B6)

$$\psi\left(1, \frac{1}{6}\ ;\ x\right) \simeq \frac{1}{x} \tag{48}$$

so that I_2 becomes $I_2 = 0$ and

$$\sigma_\chi^2 = \sigma_S^2 = 0.033\ \frac{k^2}{2\pi}\ \sqrt{\pi}\ a\ c_{no}^2\ \frac{12}{5}\ \pi^3\ L_o^{5/3}\ \exp\left[-\left(\frac{vt_c}{b}\right)^2\right]$$

$$= 0.69274\ k^2\ L_o^{5/3}\ a\ c_{no}^2\ \exp\left[-\left(\frac{vt}{b}\right)^2\right] \tag{49}$$

Region III: $\quad L_o^2 << L_o b << a << L_o a << b^2 << a^2$

$$I_1 = \frac{2\pi^2}{A^2}\ \sqrt{\pi}\ b \int_{-\infty}^{\infty} dy_c \left(\frac{y_c^2}{A^2} + \frac{1}{L_o^2}\right)^{-11/6} \exp\left[-\left(\frac{y_c}{a}\right)^2 - \left(\frac{vt_c}{b}\right)^2\right] \tag{50}$$

and can be rewritten

$$I_1 = A\, L_o^{5/3} \sqrt{\pi}\, \psi\left(\frac{1}{2}, -\frac{1}{3}; \frac{A^2}{L_o^2 a^2}\right) \exp\left[-\left(\frac{vt_c}{b}\right)^2\right] \tag{51}$$

and since $A/L_o a << 1$, we can use the small argument approximation

$$\psi\left(\frac{1}{2}, -\frac{1}{3}; \frac{A^2}{a^2 L_o^2}\right) \cong \frac{\Gamma\left(\frac{4}{3}\right)}{\Gamma\left(\frac{11}{6}\right)} \tag{52}$$

I_2 is the same as that in region II. Therefore

$$\sigma_\chi^2 = \sigma_S^2 = 0.033\, c_{no}^2 \sqrt{\pi}\; a\, \pi^2 k^3 \frac{b L_o^{5/3}}{L} \frac{\Gamma\left(\frac{4}{3}\right)}{\Gamma\left(\frac{11}{6}\right)} \exp\left[-\left(\frac{vt_c}{b}\right)^2\right] \tag{53}$$

$$= 0.548\, k^3\, ab\, \frac{L_o^{8/3}}{L}\, c_{no}^2 \exp\left[-\left(\frac{vt_c}{b}\right)^2\right] \tag{54}$$

It should be emphasized that we have used the approximation $A/L_o << vt_c$ in the above results and that this condition should be checked especially in region III. We note that the results contain the factor

$$\exp\left[-\left(\frac{vt_c}{b}\right)^2\right]$$

which becomes significant only when $vt_c > b$. This factor represents the effect of the finite extent of the turbulence in the y_c direction when the line-of-sight traverses a distance longer than b.

The dependence of σ_χ^2 on L is summarized in Fig. B-4. If $vt_c << b$, then the behavior of σ_χ^2 can be explained in a similar manner as in Ref. B5. In region I we see only the effects of turbulence inhomogeneity and finite extent in the x_c direction, while in regions II and III the effects in the transverse direction as well. In region II the largest blob size is L_o so that the scattering angle is no smaller than $(kL_o)^{-1}$. Also since $L >> kL_o^2$ corresponds to the Fraunhofer region of L_o, the contribution from each blob decreases as L^{-2}. Therefore, even though the number of blobs contributing to the fluctuation increases as the square of the distance L, the variance of the log-amplitude fluctuation remains essentially constant.

At $L = kL_o b$, the Fresnel-zone size is the same as the size of the turbulent medium in the y_c direction of the L = 0 plane. In region III, $L > kL_o b$; the number of blobs increases as L and since the contribution from each blob decreases as L^{-2}, the variance decreases as L^{-1}.

It should be point out that even though the expressions for σ_χ^2 and σ_S^2 in regions II and III are asymptotic, they are also valid close to the boundary separating regions II and III. We can obtain some estimate on the error in using these results close to the boundary by evaluating and comparing σ_χ^2 at the boundary $L = kL_o b$ using (49) and (54). We find that the ratio of (49) to (54) at $L = kL_o b$ is 1.26.

B.3 Theoretical Frequency Spectra of Log-amplitude and Phase Fluctuations

Let us rewrite (26) in the following form

$$W_\chi(L, \vec{\rho}_c, t_c, f) = 8\pi^2 k^2 \int_0^L dx_c \frac{1}{(2\pi)^2} \int\int_{-\infty}^{\infty} d\vec{\rho}_c' \, B_n^v(x_c, \vec{\rho}_c' - \vec{v}t_c) \, g_\chi(x_c, \vec{\rho}_c, \vec{\rho}_c') \tag{55}$$

where

$$g_\chi(x_c,\vec{\rho}_c,\vec{\rho}_c') = \frac{1}{2\pi}\int_{-\infty}^{\infty}\int d\vec{\kappa}_d \exp\left[i\vec{\kappa}_d\cdot(\gamma\vec{\rho}_c-\vec{\rho}_c')\right]\int_{-\infty}^{\infty} d\vec{\kappa}_c \exp(i\vec{\kappa}_c\cdot\vec{v}\tau)S_\chi(x_c,\vec{\kappa}_d,\vec{\kappa}_c),$$

$$\cdot\int_{-\infty}^{\infty}\Phi_n^o(\kappa_c)\, e^{-i\omega\tau}d\tau \tag{56}$$

and S_χ is given by (20). For the τ integration in (56) we use the fact that

$$\frac{1}{2\pi}\int_{-\infty}^{\infty}\exp(-i\vec{\kappa}_c\cdot\vec{v}\tau - i\omega\tau)\,d\tau = \delta(\omega+\vec{\kappa}_c\cdot\vec{v}) \tag{57}$$

where δ is Dirac's delta function so that

$$g_\chi(x_c,\vec{\rho}_c,\vec{\rho}_c') = \int_{-\infty}^{\infty}\int d\vec{\kappa}_d \exp\left[i\vec{\kappa}_d\cdot(\gamma\vec{\rho}_c-\vec{\rho}_c')\right]\int_{-\infty}^{\infty}\int d\vec{\kappa}_c\,\delta(\omega+\vec{\kappa}_c\cdot\vec{v})S_\chi(x_c,\vec{\kappa}_d,\vec{\kappa}_c)\Phi_n^o(\kappa_c) \tag{58}$$

For the $\vec{\kappa}_c$ integration we use a polar coordinate system where κ_c is the radial distance and α is the angle $\vec{\kappa}_c$ makes with $\vec{v}$. We will first consider the integration over α. Since (Ref. B7)

$$\int_a^b d\alpha\,\delta[f(\alpha)] = \sum_{n=1}^{N}\int_a^b \frac{\delta(\alpha-\alpha_n)}{\left|\frac{df(\alpha)}{d\alpha}\right|_{\alpha=\alpha_n}} \tag{59}$$

where α_n are the roots of $f(\alpha) = 0$ within (a, b), we obtain

$$\int_{-\pi}^{\pi} d\alpha \delta(\omega + \kappa_c v \cos\alpha) = \begin{cases} \dfrac{1}{\sqrt{(\kappa_c v)^2 - \omega^2}} \displaystyle\int_{-\pi}^{\pi} d\alpha[\delta(\alpha - \alpha_1) + \delta(\alpha - \alpha_2)] & \text{for } \kappa_c v > \omega \\ 0 & \text{for } \kappa_c v < \omega \end{cases} \tag{60}$$

where

$$\alpha_1 = \cos^{-1}\left(-\frac{\omega}{\kappa_c v}\right) \qquad 0 \le \alpha_1 \le \pi$$

$$\alpha_2 = -\alpha_1$$

We denote the vectors $\vec{\kappa}_c$ corresponding to α_1 and α_2, $\vec{\kappa}_{c1}$ and $\vec{\kappa}_{c2}$ respectively (see Fig. B-5). Then (46) becomes

$$g_\chi(x_c, \vec{\rho}_c, \vec{\rho}_c') = \int_{-\infty}^{\infty}\int d\vec{\kappa}_d \exp[i\vec{\kappa}_d \cdot (\gamma\vec{\rho}_c - \vec{\rho}_c')] \int_{\omega/v}^{\infty} \kappa_c d\kappa_c \frac{1}{\sqrt{(\kappa_c v)^2 - \omega^2}}$$

$$\cdot [S_\chi(x_c, \vec{\kappa}_d, \vec{\kappa}_{c1}) + S_\chi(x_c, \vec{\kappa}_d, \vec{\kappa}_{c2})]\, \Phi_n^o(\kappa_c) \tag{61}$$

Let us now carry out the integration over $\vec{\kappa}_d$. Before we do this we will assume that the wind direction is along the y_c axis. We will also write

$$\left.\begin{aligned} \vec{B} &= \gamma\vec{\rho}_c - \vec{\rho}_c' \\ \vec{C}_1 &= A\vec{\kappa}_{c1} \\ \vec{C}_2 &= A\vec{\kappa}_{c2} \end{aligned}\right\} \tag{62}$$

Note from Fig. B-6 that $C_{1y_c} = C_{2y_c} = -A\,\omega/v$ and $C_{1z_c} = -C_{2z_c}$, where the subscript y_c or z_c designates the respective component. Since

$$\iint_{-\infty}^{\infty} \exp\left(i\vec{\kappa}_d \cdot \vec{B} + iA\kappa_c^2 + i\,\frac{A}{4}\,\kappa_d^2\right)\, d\vec{\kappa}_d = \frac{4\pi}{A} \exp\left(iA\kappa_c^2 + i\,\frac{\pi}{2} - i\,\frac{B^2}{A}\right) \tag{63}$$

(61) becomes

$$g_\chi\left(x_c, \vec{\rho}_c, \vec{\rho}_c'\right) = \int_{\omega/v}^{\infty} \frac{\kappa_c\, d\kappa_c}{\sqrt{(\kappa_c v)^2 - \omega^2}}\, \Phi_n^o(\kappa_c) \left\{ \frac{(2\pi)^2}{4} \left[\delta(B_{y_c} + C_{1y_c})\, \delta(B_{z_c} + C_{1z_c}) \right.\right.$$

$$+ \delta(B_{y_c} - C_{1y_c})\, \delta(B_{z_c} - C_{1z_c}) + \delta(B_{y_c} + C_{1y_c})\, \delta(B_{z_c} - C_{1z_c})$$

$$\left.\left. + \delta(B_{y_c} - C_{1y_c})\, \delta(B_{z_c} + C_{1z_c})\right] - \frac{4\pi}{A}\, \mathrm{Re}\left[\exp\left(iA\kappa_c^2 - i\,\frac{B^2}{A^2} + i\,\frac{\pi}{2}\right)\right]\right\} \tag{64}$$

where Re [ ] means real part of [ ]. For the integration over κ_c, we will use the following change of variable

$$\kappa_c^2 - \frac{\omega^2}{v^2} = \kappa_c'^2 \tag{65}$$

and from Fig. B-6 we note that $C_{1z_c} = -C_{2z_c} = A\kappa'_{c1} = A\kappa'_c$. Thus,

$$g_\chi(x_c,\vec{\rho}_c,\vec{\rho}'_c) = \int_0^\infty \frac{d\kappa'_c}{v}\,\Phi_n^o(\kappa'_c)\left\{\frac{(2\pi)^2}{4}\left[\delta\left(B_{y_c} - A\frac{\omega}{v}\right)\delta(B_{z_c} + A\kappa'_c) + \delta\left(B_{y_c} + A\frac{\omega}{v}\right)\delta(B_{z_c} - A\kappa'_c)\right.\right.$$

$$\left. + \delta\left(B_{y_c} - A\frac{\omega}{v}\right)\delta(B_{z_c} - A\kappa'_c) + \delta\left(B_{y_c} + A\frac{\omega}{v}\right)\delta(B_{z_c} + A\kappa'_c)\right]$$

$$\left. - \frac{4\pi}{A}\,\mathrm{Re}\left[\exp\left(iA\kappa_c^2 - i\frac{B^2}{A} + i\frac{\pi}{2}\right)\right]\right\} \tag{66}$$

and finally

$$g_\chi(x_c, \vec{\rho}_c, \vec{\rho}'_c) = g_{\chi 1}(x_c, \vec{\rho}_c, \vec{\rho}'_c) + g_{\chi 2}(x_c, \vec{\rho}_c, \vec{\rho}'_c) \tag{67}$$

where

$$g_{\chi 1}(x_c, \vec{\rho}_c, \vec{\rho}'_c) = \frac{(2\pi)^2}{4vA}\left\{\delta\left(B_{y_c} - A\frac{\omega}{v}\right) + \delta\left(B_{y_c} + A\frac{\omega}{v}\right)\right\}\Phi_n^o\left(\left|\frac{B_{z_c}}{A}\right|\right) \tag{68}$$

$$g_{\chi 2}(x_c, \vec{\rho}_c, \vec{\rho}'_c) = \frac{4\pi}{vA}\int_0^\infty d\kappa'_c\,\Phi_n^o(\kappa'_c)\,\mathrm{Re}\left[\exp\left(iA\kappa_c'^2\right.\right.$$

$$\left.\left. + iA\frac{\omega^2}{v^2} - i\frac{B^2}{A} + i\frac{\pi}{2}\right)\right] \tag{69}$$

The frequency spectrum of the log-amplitude fluctuations for a turbulent medium characterized by (7), (8) and (15) is given by (55) along with (67).

Following a procedure similar to that described above the frequency spectrum of the phase fluctuations $W_S(L, \vec{\rho}_c, t_c, f)$ can be derived.

$$W_S(L,\vec{\rho}_c,t_c,f) = 8\pi^2 k^2 \int_0^L dx_c \iint_{-\infty}^{\infty} d\vec{\rho}_c' \; B_n^v(x_c,\vec{\rho}_c' - \vec{v}t_c) \; g_S(x_c,\vec{\rho}_c,\vec{\rho}_c') \tag{70}$$

where

$$g_S(x_c, \vec{\rho}_c, \vec{\rho}_c') = g_{\chi 1}(x_c, \vec{\rho}_c, \vec{\rho}_c') - g_{\chi 2}(x_c, \vec{\rho}_c, \vec{\rho}_c') \tag{71}$$

B.4 Theoretical Frequency Spectra for Mariner 5

The results given in Appendix B-3 were in terms of B_n^v and Φ_n^o. In this section we will apply them to the case of Mariner 5. As in Appendix B2 we will assume B_n^v and Φ_n^o to be given by (28) and (29) respectively. We will also assume that the observation point is located on the x_c axis (Fig. B-3) so that $\vec{\rho}_c = o$. Then according to (62) $B_{z_c} = - z_c'$ and

$$\Phi_n^o\left(\left|\frac{B_{z_c}}{A}\right|\right) = \left[\left(\frac{z_c'}{A}\right)^2 + \frac{\omega^2}{v^2} + \frac{1}{L_o^2}\right]^{-11/6} \tag{72}$$

Substituting (72) into (69), $g_{\chi 2}$ becomes

$$g_{\chi 2}(x_c,\vec{\rho}_c') = \frac{4\pi}{Av} \operatorname{Re}\left\{\exp\left(i\, A\, \frac{\omega^2}{v^2}\right.\right.$$

$$\left.\left. - i\,\frac{B}{A} + i\,\frac{\pi}{2}\right) \frac{\sqrt{\pi}}{2}\left(\frac{\omega^2}{v^2} + \frac{1}{L_o^2}\right)^{-4/3} \psi\left[\frac{1}{2}, -\frac{1}{3}; - iA\left(\frac{\omega^2}{v^2} + \frac{1}{L_o^2}\right)\right]\right\} \tag{73}$$

Let us apply (55) to the configuration in Fig. B-3. At the observation point on earth

$$W_\chi(L', t_c, f) = 8\pi^2 k^2 \int_0^{L'} dx_c [M_1(t_c, f) - M_2(t_c, f)] \tag{73}$$

where

$$M_1(t_c, f) = \int\int_{-\infty}^{\infty} d\vec{\rho}_c' \; B_n^v(x_c, \vec{\rho}_c' - \vec{v}t_c) \; g_{\chi 1}(x_c, \vec{\rho}_c') \tag{74}$$

$$M_2(t_c, f) = \int\int_{-\infty}^{\infty} d\vec{\rho}_c' \; B_n^v(x_c, \vec{\rho}_c' - \vec{v}t_c) \; g_{\chi 2}(x_c, \vec{\rho}_c') \tag{75}$$

Then, using (68) and (73) and model for c_n^2 in (32), we obtain

$$M_1(t_c,f) = 0.033 \; c_{no}^2 \exp\left[-\frac{(x_c - L)^2}{a^2}\right] \frac{\sqrt{\pi}}{4v} \left(\frac{\omega^2}{v^2} + \frac{1}{L_o^2}\right)^{-4/3} \psi\left[\frac{1}{2}, -\frac{1}{3}; \frac{A^2}{a^2}\left(\frac{\omega^2}{v^2} + \frac{1}{L_o^2}\right)\right]$$

$$\cdot \left\{ \exp\left[-\frac{\left(A\frac{\omega}{v} + vt_c\right)^2}{b^2}\right] + \exp\left[-\frac{\left(A\frac{\omega}{v} + vt_c\right)^2}{b^2}\right] \right\} \tag{76}$$

$$M_2(t_c,f) = 0.033\, c_{no}^2$$

$$\exp\left[-\frac{(x_c - L)^2}{a^2}\right] \frac{1}{Av\pi}\, \mathrm{Re}\left\{\frac{\pi}{\sqrt{\left(\frac{1}{b^2}+\frac{i}{A}\right)\left(\frac{1}{a^2}+\frac{i}{A}\right)}} \exp\left[\left(\frac{2vt_c}{b^2}\right)^2 \frac{1}{4\left(\frac{1}{b^2}+\frac{i}{A}\right)}\right.\right.$$

$$\left.\left. - \frac{v^2 t_c^2}{b^2}\right] \exp\left[iA\frac{\omega^2}{v^2} + i\frac{\pi}{2}\right] \frac{\sqrt{\pi}}{2}\left(\frac{\omega^2}{v^2}+\frac{1}{L_o^2}\right)^{-4/3} \psi\left[\frac{1}{2},-\frac{1}{3};-iA\left(\frac{\omega^2}{v^2}+\frac{1}{L_o^2}\right)\right]\right\} \tag{77}$$

To carry out the integration over x_c in (73) we note from Fig. B-3 that $A = (L' - x_c)\, x_c/kL'$ can be written alternately as $[x_c\, L''/(L + L'')]/k$. L'' is the distance from the planetary atmosphere to the observation point on earth and is much longer than L; A can therefore be approximated by x_c/k. Also, since $L >> a$, we can extend the lower limit of integration (73) from o to $-\infty$ and noting that

$$\int_{-\infty}^{\infty} dx_c \exp\left[-\frac{(x_c - L)^2}{a^2} - \frac{1}{b^2}\left(\frac{x_c}{k}\frac{\omega}{v} + vt_c\right)^2\right] f(x_c)$$

$$\cong \frac{\sqrt{\pi}\, a}{\sqrt{1 + \left(\frac{a}{b}\frac{\omega}{kv}\right)^2}} \exp\left\{-\frac{1}{b^2}\left(\frac{L}{k}\frac{\omega}{v} + vt_c\right)^2\left[\frac{1}{1 + \left(\frac{a\omega}{bkv}\right)^2}\right]\right\} f(L) \tag{78}$$

and

$$\int_{-\infty}^{\infty} dx_c \exp\left[-\frac{(x_c - L)^2}{a^2} + i\frac{x_c}{k}\frac{\omega^2}{v^2}\right] f(x_c)$$

$$\cong \sqrt{\pi}\, a \exp\left[i\frac{L}{k}\frac{\omega^2}{v^2} - \frac{1}{4}\left(\frac{a}{k}\frac{\omega^2}{v^2}\right)^2\right] f(L) \tag{79}$$

if $f(x_c)$ is slowly varying, (73), (76) and (77) become

$$W_\chi(L', t_c, f) = 0.033\, c_{no}^2\, 8\pi^2 k^2 \frac{\pi a}{2v}\left(\frac{\omega^2}{v^2} + \frac{1}{L_o^2}\right)^{-4/3}(M_1' - M_2') \tag{80}$$

where

$$M_1' = \frac{1}{2}\psi\left[\frac{1}{2}, -\frac{1}{3}; \frac{L^2}{k^2a^2}\left(\frac{\omega^2}{v^2} + \frac{1}{L_o^2}\right)\right] \frac{1}{\sqrt{1 + \left(\frac{a\omega}{bkv}\right)^2}}\left[\exp\left\{-\frac{1}{b^2}\left(\frac{L}{k}\frac{\omega}{v} + vt_c\right)^2\left[\frac{1}{1 + \left(\frac{a\omega}{bkv}\right)^2}\right]\right\}\right.$$

$$\left. + \exp\left\{-\frac{1}{b^2}\left(\frac{L}{k}\frac{\omega}{v} - vt_c\right)^2\left[\frac{1}{1 + \left(\frac{a\omega}{bkv}\right)^2}\right]\right\}\right] \tag{81}$$

$$M_2' = \frac{k}{L}\,\mathrm{Re}\left\{\frac{1}{\sqrt{\left(\frac{1}{b^2} + \frac{ik}{L}\right)\left(\frac{1}{a^2} + \frac{ik}{L}\right)}} \exp\left[\left(\frac{2vt_c}{b}\right)^2 \frac{1}{4\left(\frac{1}{b^2} + \frac{ik}{L}\right)} - \frac{v^2t_c^2}{b^2} + i\frac{L}{k}\frac{\omega^2}{v^2} + i\frac{\pi}{2}\right.\right.$$

$$\left.\left. - \frac{1}{4}\left(\frac{a\omega^2}{kv^2}\right)^2\right] \psi\left[\frac{1}{2}, -\frac{1}{3}; -i\frac{L}{k}\left(\frac{\omega^2}{v^2} + \frac{1}{L_o^2}\right)\right]\right\} \tag{82}$$

Similarly,

$$W_S(L', t_c, f) = 0.033\, c_{no}^2\, 8\pi^2 k^2\, \frac{\pi a}{2v} \left(\frac{\omega^2}{v^2} + \frac{1}{L_o^2} \right)^{-4/3} (M_1' + M_2') \tag{83}$$

We can check if (80) and (83) reduce to the results for a plane wave propagating in a homogeneous turbulent medium by letting $a \to \infty$ and $b \to \infty$ and noting that (Ref. B6)

$$\lim_{z \to o} \psi(a, c; z) = \frac{\Gamma(1 - c)}{\Gamma(1 + a - c)} \quad \text{if Re } [c] < o \tag{84}$$

where Γ is the gamma function. We obtain at $x_c = L$

$$W_\chi(f) = 8\pi k^2 L(0.033)\, c_{no}^2\, \frac{1}{v} [W_{\chi 1}(f) + W_{\chi 2}(f)] \tag{85}$$

$$W_S(f) = 8\pi k^2 L(0.033)\, c_{no}^2\, \frac{1}{v} [W_{\chi 1}(f) - W_{\chi 2}(f)] \tag{86}$$

where

$$W_{\chi 1}(f) = \frac{\sqrt{\pi}}{2} \frac{\Gamma\left(\frac{4}{3}\right)}{\Gamma\left(\frac{11}{6}\right)} \left(\frac{\omega^2}{v^2} + \frac{1}{L_o^2} \right)^{-4/3} \tag{87}$$

$$W_{\chi 2}(f) = -\frac{\sqrt{\pi}}{2} \operatorname{Re} \left\{ \exp\left(i \frac{L}{k} \frac{\omega^2}{v^2} \right) \left(\frac{\omega^2}{v^2} + \frac{1}{L_o^2} \right)^{-4/3} \psi \left[\frac{1}{2}, -\frac{1}{3}; -i \frac{L}{k} \left(\frac{\omega^2}{v^2} + \frac{1}{L_o^2} \right) \right] \right\} \tag{88}$$

which agree with those derived by Tatarski (Ref. B1).

Let us evaluate (80) - (83) for regions II and III as defined in Appendix B2. We recall that in regions II and III we have the condition that $L_o^2 << L/k << L_o a$. We can therefore use the small argument approximation for ψ in M_1' and the large argument approximation for ψ in M_2', i.e. (Ref. B6)

$$\psi\left\{\frac{1}{2}, -\frac{1}{3}; \left(\frac{L}{kaL_o}\right)^2\left[1+\frac{\omega^2}{\left(\frac{v}{L_o}\right)^2}\right]\right\} \cong \frac{\Gamma\left(\frac{4}{3}\right)}{\Gamma\left(\frac{11}{6}\right)} \qquad \text{in } M_1' \quad (89)$$

$$\psi\left\{\frac{1}{2}, -\frac{1}{3}; -i\frac{L}{kL_o^2}\left[1+\frac{\omega^2}{\left(\frac{v}{L_o}\right)^2}\right]\right\} \cong \left[-i\frac{L}{k}\left(\frac{\omega^2}{v^2}+\frac{1}{L_o^2}\right)\right]^{-1/2} \qquad \text{in } M_2' \quad (90)$$

We also note that since $b >> L_o$, $L/k << b^2$ in regions II and III and we finally obtain

$$W_\chi(f) = K\left[1+\frac{\omega^2}{\left(\frac{v}{L_o}\right)^2}\right]^{-4/3}(W_1 - W_2) \quad (91)$$

$$W_S(f) = K\left[1+\frac{\omega^2}{\left(\frac{v}{L_o}\right)^2}\right]^{-4/3}(W_1 + W_2) \quad (92)$$

where

$$K = 0.033\, c_{no}^2\, 4\pi^3\, \frac{L_o^{8/3}}{v}\, k^2 a \quad (93)$$

$$W_1 = \frac{\Gamma\left(\frac{4}{3}\right)}{\Gamma\left(\frac{11}{6}\right)}\frac{1}{2}\ \frac{1}{\sqrt{1+\left(\frac{a\omega}{bkv}\right)^2}}\left[\exp\left\{-\frac{1}{b^2}\left(\frac{L}{k}\frac{\omega}{v}+vt_c\right)^2\left[\frac{1}{1+\left(\frac{a\omega}{bkv}\right)^2}\right]\right\}\right.$$

$$\left.+\exp\left\{-\frac{1}{b^2}\left(\frac{L}{k}\frac{\omega}{v}-vt_c\right)^2\left[\frac{1}{1+\left(\frac{a\omega}{bkv}\right)^2}\right]\right\}\right] \tag{94}$$

$$W_2 = \exp\left[-\frac{v^2t_c^2}{b^2}-\frac{1}{4}\left(\frac{a\omega^2}{kv^2}\right)^2\right]\sqrt{\frac{k}{L}}\left(\frac{\omega^2}{v^2}+\frac{1}{L_o^2}\right)^{-1/2}\cos\left(\frac{\pi}{4}+\frac{L}{k}\frac{\omega^2}{v^2}\right) \tag{95}$$

The validity of Taylor's frozen-in hypothesis for wave propagation in localized smoothly varying turbulence deserves some discussion. We will follow similar arguments used by Tatarski (Ref. B1) in his discussion of wave propagation in homogeneous turbulence.

In the case of localized smoothly varying turbulence, the fluctuations are mainly attributable to inhomogeneities in the medium whose scale size ℓ is of the order L_o moving with velocity v. (Of course in the case of Mariner 5 v is the sweeping motion of the line-of-sight.) The inhomogeneities exhibit intrinsic random velocity in addition to the constant wind velocity v and this random velocity is of the order $(\varepsilon\ell)^{1/3}$ or $(\varepsilon L_o)^{1/3}$ where ε is the rate of dissipation of the turbulent energy. The lifetime τ_v of these velocities (time during which these velocities remain constant) depends only on ε and ℓ and is of the order $\varepsilon^{1/3}\ell^{2/3}$. On the other hand, the time required for an inhomogeneity moving with velocity v to cover a distance $\ell = L_o$ is of the order $T \sim L_o/v$. The frozen-in hypothesis will therefore be valid when $\tau_v \gg T$ or

$$v \gg (\varepsilon L_o)^{1/3} \tag{96}$$

According to Refs. B8 and B9, for the atmosphere of Venus ε is of the order of 10^{-1} cm^2 sec^{-3}. As shown in the main text L_o is of the order of 100 m. For these values, v must be greater than 0.0215 m/sec. This condition is certainly met in the case of Mariner 5.

References

B1. Tatarski, A. I., The Effects of the Turbulent Atmosphere on Wave Propagation, Nauka, Moscow, 1967. Translated and available from the U. S. Dept. of Commerce, Springfield, Va.

B2. Ishimaru, A., "Fluctuations of a Focused Beam Wave for Atmospheric Turbulence Probing," Proc. of IEEE, Vol. 57, No. 4, pp. 407-414, April 1969.

B3. Silverman, R., "Locally Stationary Random Processes," IRE Trans. Inform. Theory, Vol. IT 2-3, pp. 182-187, September 1957.

B4. Ishimaru, A., "A New Approach to the Problem of Wave Fluctuations in Localized Smoothly Varying Turbulence," IEEE Trans. Antennas and Propagation, Vol. AP-21, No. 1, pp. 47-53, January 1973.

B5. Woo, R. and Ishimaru, A., "Remote Sensing of the Turbulence Characteristics of a Planetary Atmosphere by Radio Occultation of a Space Probe," Radio Science, Vol. 8, No. 2, pp. 103-108, February 1973.

B6. Abramowitz, M., and Stegun, I. A. (Eds.), Handbook of Mathematical Functions: With Formulas, Graphs, and Mathematical Tables, pp. 503-535, U.S. Government Printing Office, Washington D.C., 1964.

B7. van der Pol, Balth. and Bremmer, H., Operational Calculus Based on the Two-Sided Laplace Integral, University Press, Cambridge, 1955, pp. 78-79.

B8. Gurvich, A.S., "An Estimate of the Parameters of Small-Scale Turbulence in the Atmosphere of Venus Obtained from Fluctuations of Radio Signals from Venus-4 and Mariner-5," Dokl. Akad. Nauk. SSSR, Vol. 5, No. 11, pp. 1172-1178, 1969.

B9. Golitsyn, G.S., "Estimates of Some Characteristics of the General Circulation in the Atmospheres of the Terrestrial Planets," Bull. (Izv.) Acad. Sci. USSR, Atmospheric and Oceanic Physics, Vol. 4, No. 11, 1968.

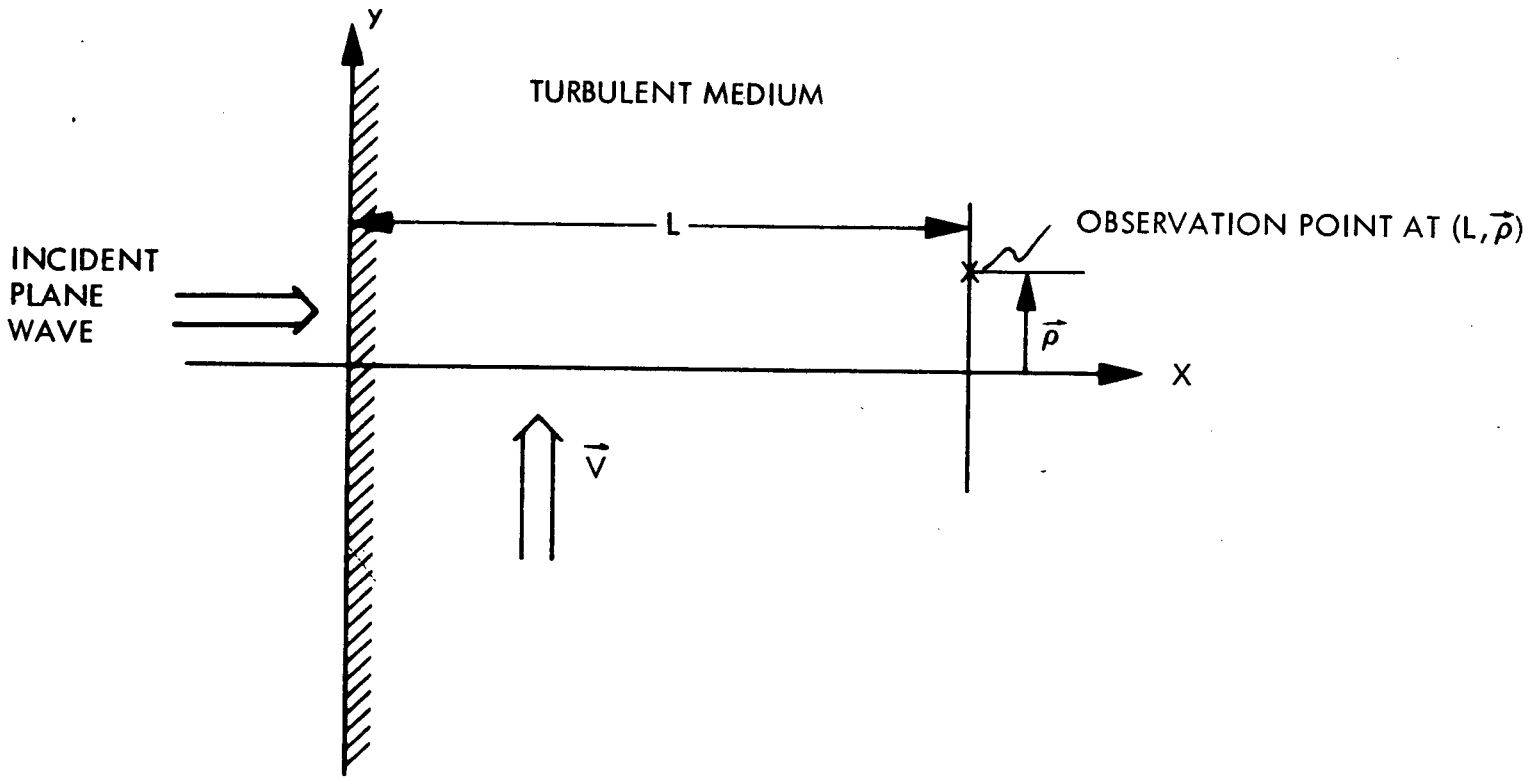

Fig. B-1. Plane Wave Configuration

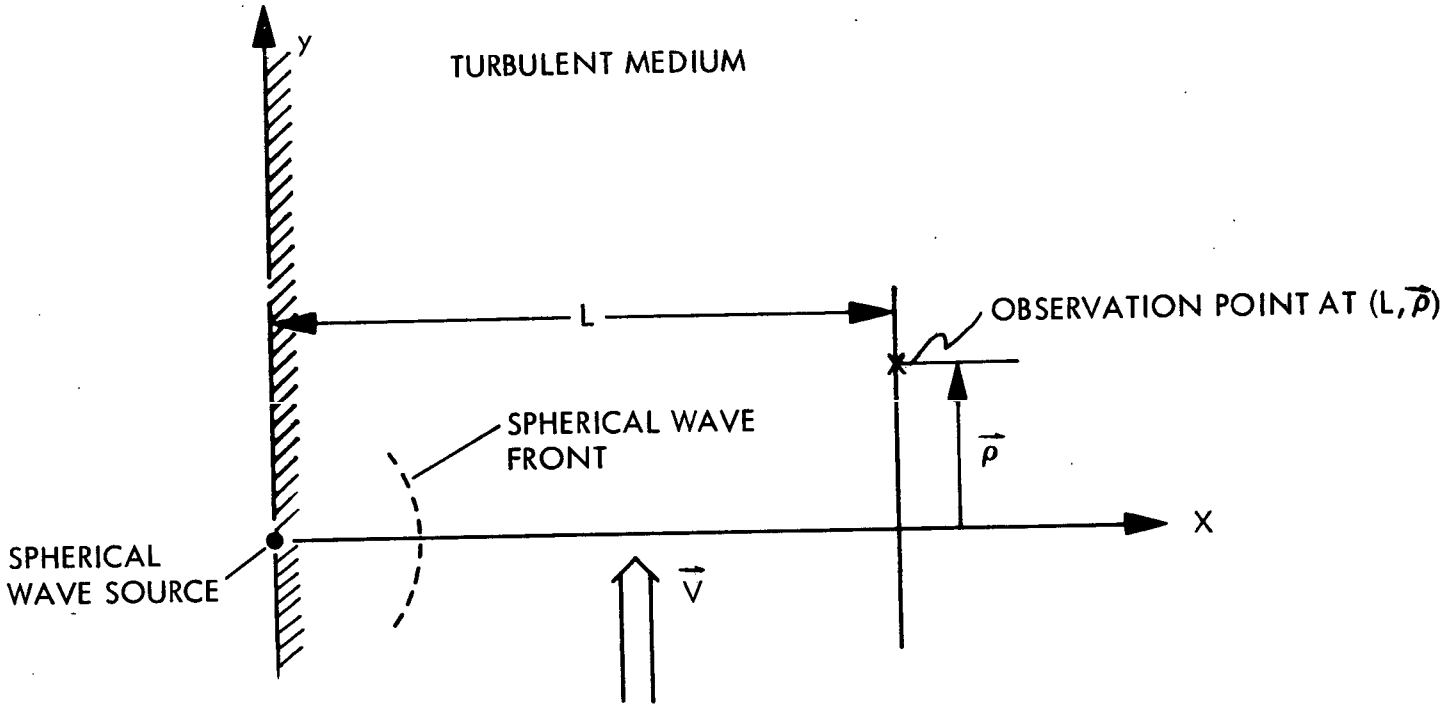

Fig. B-2. Spherical Wave Configuration

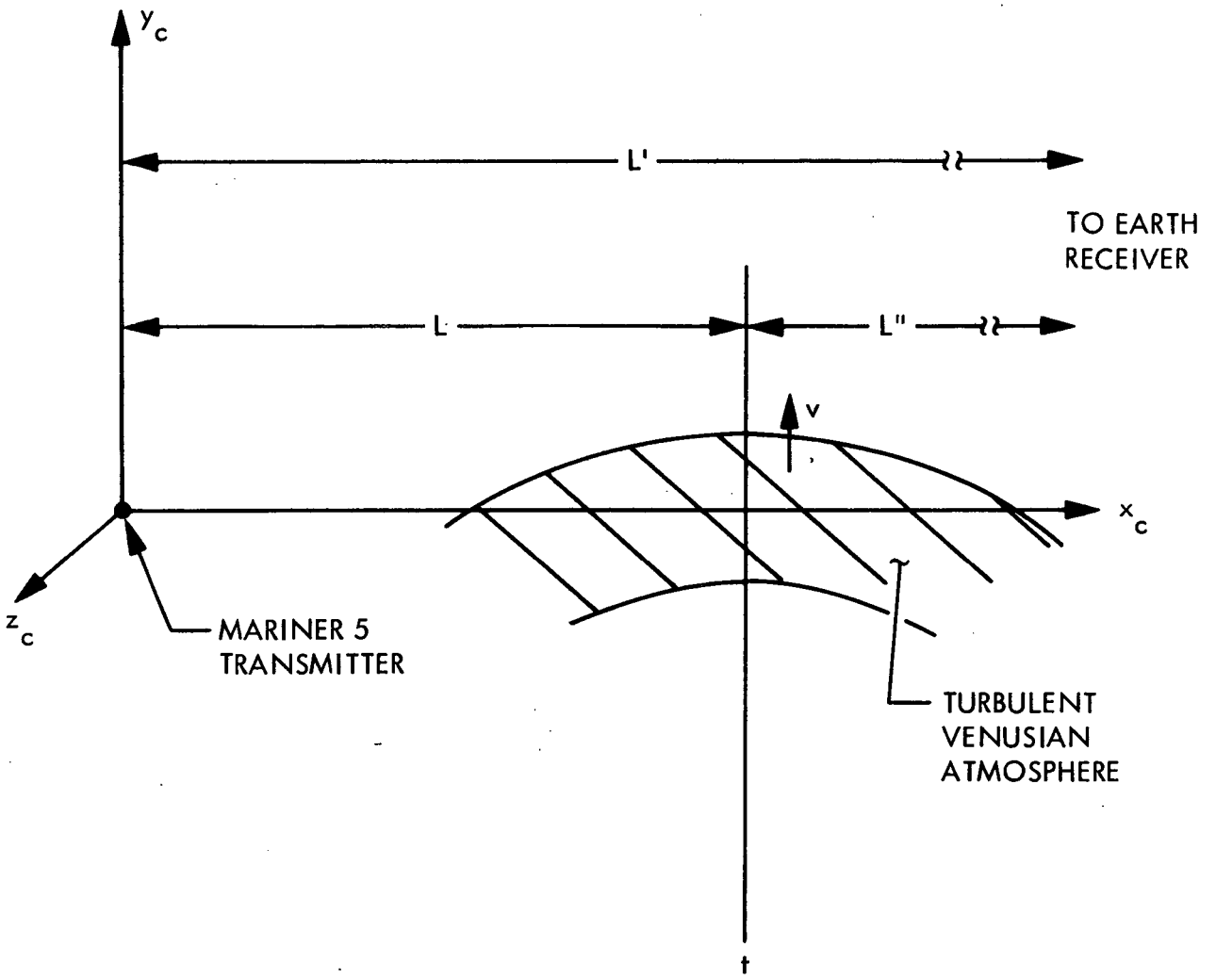

Fig. B-3. Mariner 5 Occultation Configuration

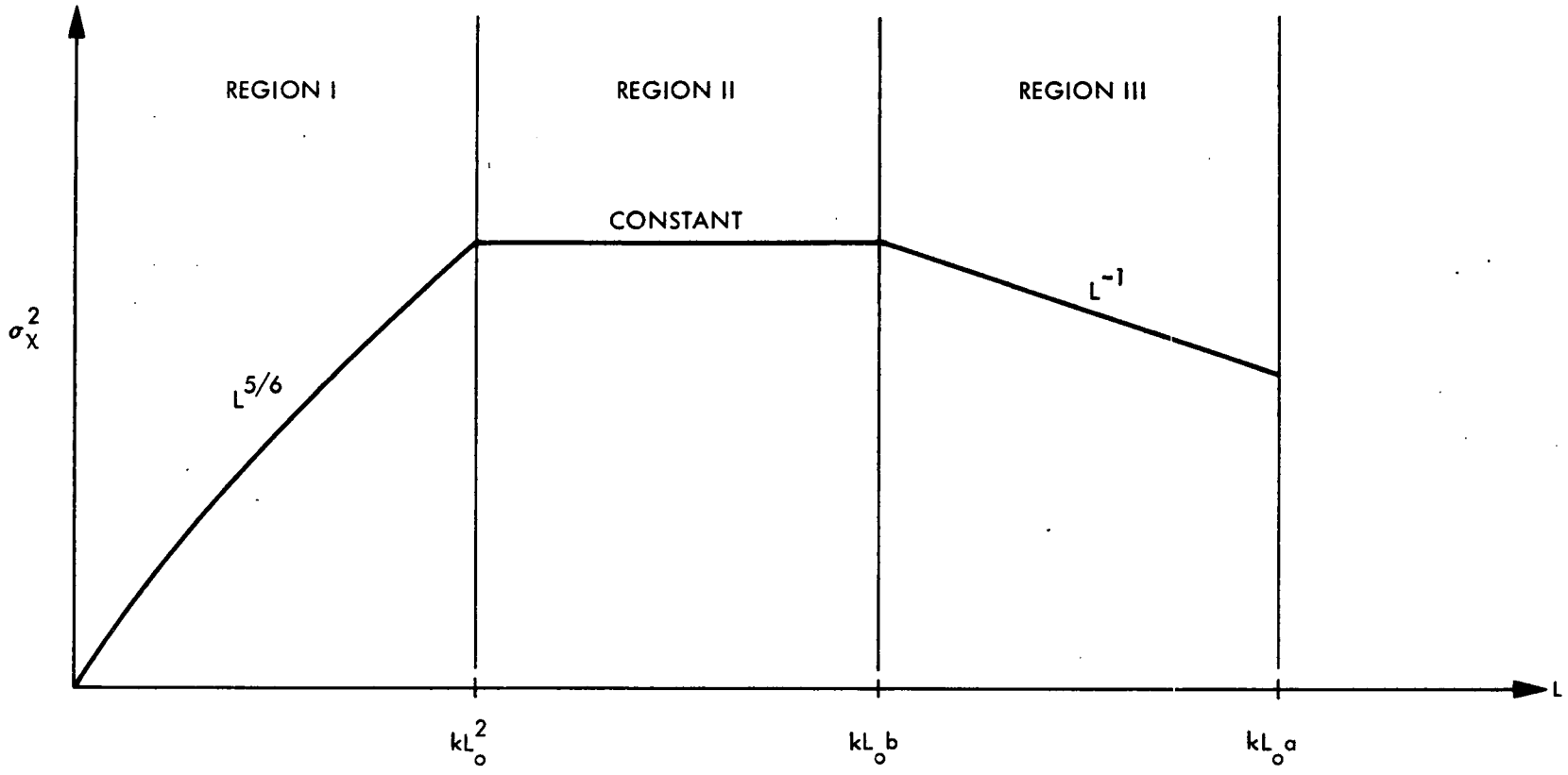

Fig. B-4. Summary of the Behavior of σ_x^2

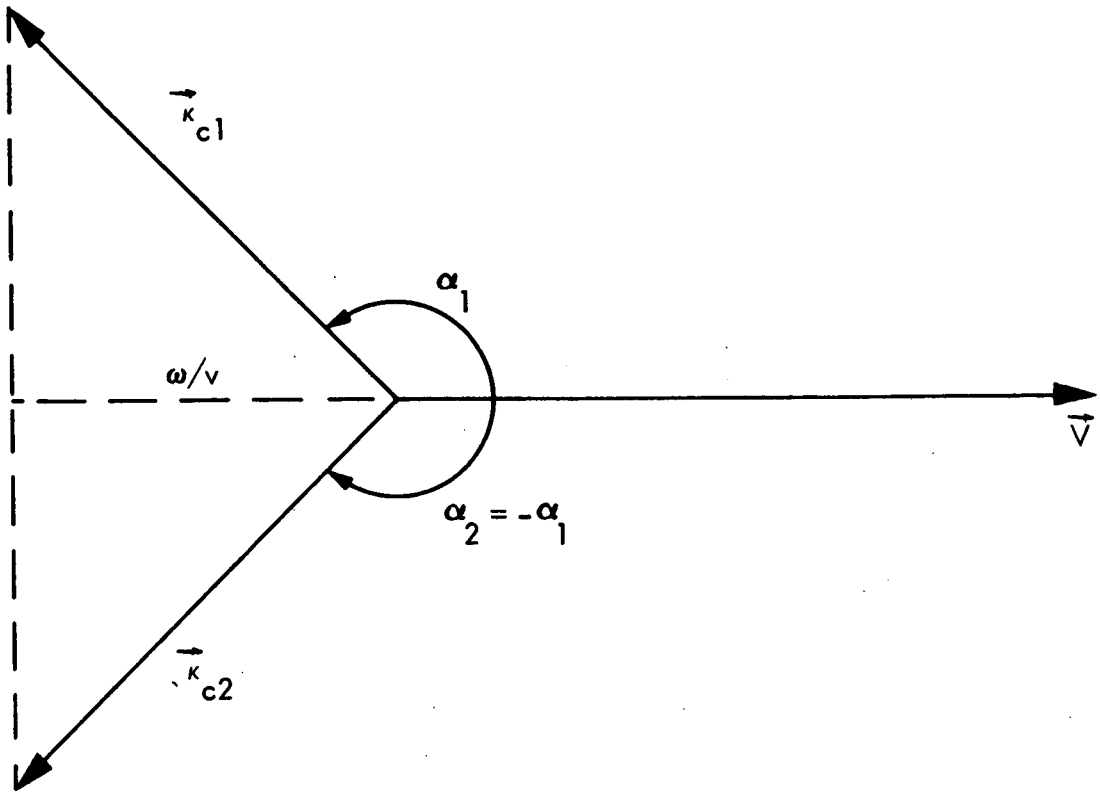

Fig. B-5. Vector Diagram for $\vec{\kappa}_{c1}$ and $\vec{\kappa}_{c2}$

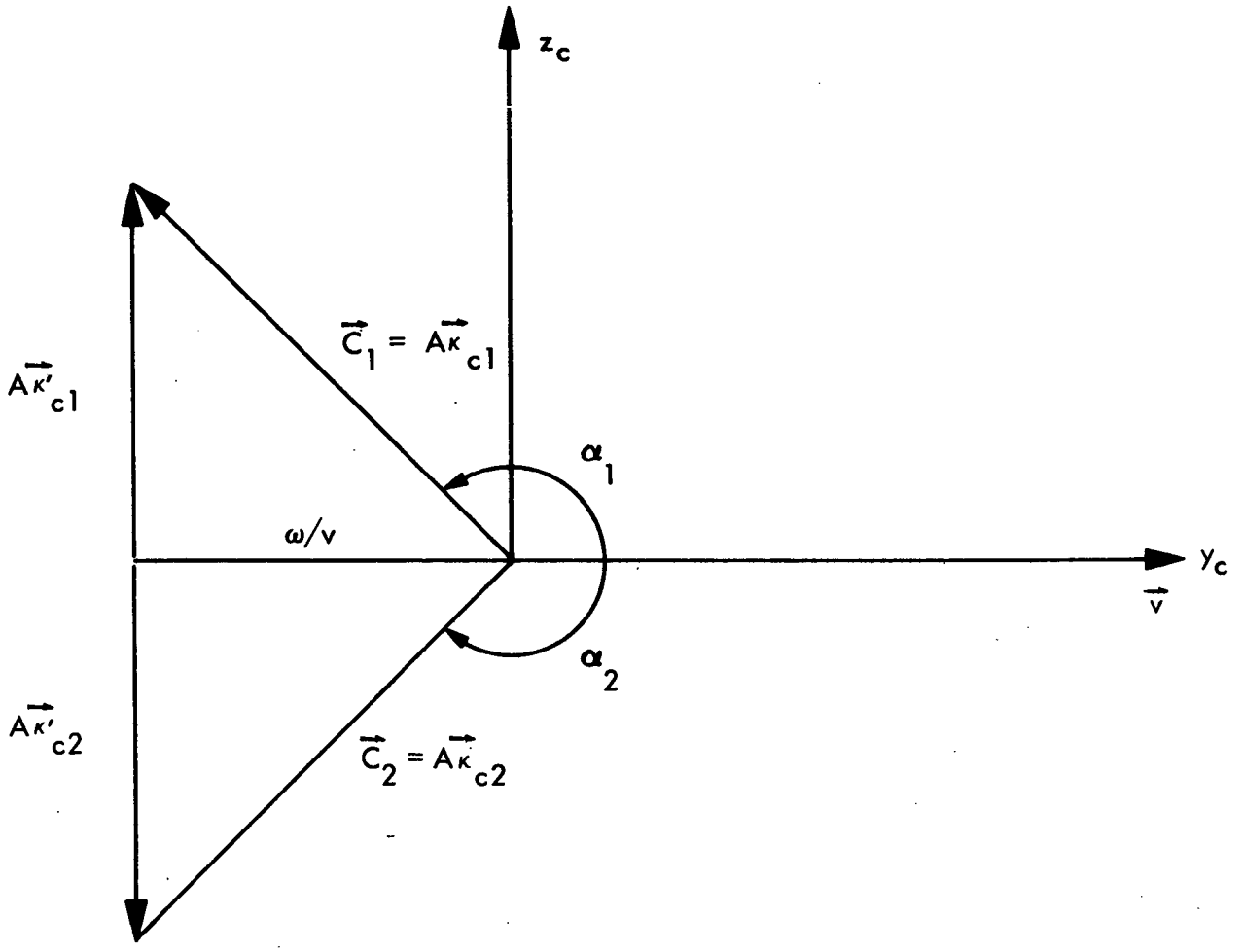

Fig. B-6. Vector Diagram for $\vec{C}_1$ and $\vec{C}_2$

NASA — JPL — Coml., L.A., Calif.